

UNIVERSITY OF CALIFORNIA, SAN DIEGO

**A search for new physics using the  $M_{T2}$  variable in all-hadronic final states produced in proton-proton collisions with a center of mass energy of 13 TeV**

A dissertation submitted in partial satisfaction of the  
requirements for the degree  
Doctor of Philosophy

in

Physics

by

Mark Derdzinski

Committee in charge:

Professor Frank Würthwein, Chair  
Professor Avraham Yagil  
Professor Benjamin Grinstein  
Professor Farhat Beg  
Professor Ian Galton

2018

Copyright  
Mark Derdzinski, 2018  
All rights reserved.

The dissertation of Mark Derdzinski is approved, and  
it is acceptable in quality and form for publication on  
microfilm and electronically:

---

---

---

---

---

---

Chair

University of California, San Diego

2018

## DEDICATION

To my family, who has always supported me in all my pursuits.

## EPIGRAPH

*For knowledge comes slowly, and when it comes, it is often at great personal expense.*

— Paul Auster, *Ghosts*

## TABLE OF CONTENTS

Signature Page . . . . .	iii
Dedication . . . . .	iv
Epigraph . . . . .	v
Table of Contents . . . . .	vi
List of Figures . . . . .	viii
List of Tables . . . . .	xii
Acknowledgements . . . . .	xiv
Vita . . . . .	xvii
Abstract of the Dissertation . . . . .	xviii
Chapter 1    Introduction . . . . .	1
Chapter 2    Theory and Motivation . . . . .	3
2.1    The Standard Model of Particle Physics . . . . .	4
2.2    Issues with the Standard Model . . . . .	6
2.3    Beyond the Standard Model: Supersymmetry . . . . .	8
Chapter 3    The Large Hadron Collider and the CMS Detector . . . . .	10
3.1    The Large Hadron Collider . . . . .	11
3.1.1    Proton Bunches and Pileup . . . . .	15
3.2    The Compact Muon Solenoid . . . . .	15
3.2.1    Silicon Tracker . . . . .	17
3.2.2    Electromagnetic Calorimeter . . . . .	18
3.2.3    Hadronic Calorimeter . . . . .	21
3.2.4    Muon Detectors . . . . .	24
3.2.5    Trigger Systems . . . . .	28
3.3    CMS Physics Objects . . . . .	29
3.3.1    Particle Flow . . . . .	29
3.3.2    Isolation . . . . .	30
3.3.3    Electrons, Muons, and Photons . . . . .	32
3.3.4    Muons . . . . .	33
3.3.5    Jets . . . . .	33
3.3.6    Missing Energy . . . . .	35
3.3.7    Monte Carlo Simulation . . . . .	36

Chapter 4	The $M_{T2}$ Variable Search . . . . .	38
4.1	Analysis Strategy . . . . .	38
4.2	The $M_{T2}$ Variable . . . . .	39
4.3	Event Selection Criteria . . . . .	41
4.4	Search Regions . . . . .	41
4.5	Control Regions . . . . .	47
4.5.1	Single Lepton Control Region . . . . .	49
4.5.2	Dilepton Control Region . . . . .	50
4.5.3	Multijet Control Region . . . . .	51
Chapter 5	Background Estimates . . . . .	53
5.1	Types of Backgrounds . . . . .	53
5.2	Multijet Estimate . . . . .	54
5.2.1	Multijet Signal Region Prediction . . . . .	55
5.2.2	Monojet Signal Region Prediction . . . . .	60
5.3	Lost Lepton Estimate . . . . .	62
5.3.1	Background Prediction . . . . .	62
5.3.2	Systematic Uncertainties . . . . .	63
5.3.3	Signal Contamination . . . . .	68
5.4	Invisible Z Estimate . . . . .	69
5.4.1	Background Prediction . . . . .	69
5.4.2	Systematic Uncertainties . . . . .	75
Chapter 6	Results . . . . .	81
6.1	Yields and Background Fits . . . . .	81
6.2	Signal Interpretations . . . . .	86
6.2.1	Signal Yield Systematic Uncertainties . . . . .	86
6.2.2	Exclusion Limits . . . . .	92
Chapter 7	Extending the All-Hadronic Search . . . . .	100
7.1	Natural Supersymmetry and EWKinos . . . . .	101
7.2	The Soft Lepton Search . . . . .	102
7.2.1	Event Selection . . . . .	102
7.2.2	Backgrounds . . . . .	103
7.2.3	Single Lepton Estimate . . . . .	104
7.2.4	Dilepton Estimate . . . . .	106
7.2.5	Fake Lepton Estimate . . . . .	107
7.2.6	Results and Interpretations . . . . .	108
7.3	Future Extensions for an All-Hadronic Search . . . . .	109
Bibliography	. . . . .	115

## LIST OF FIGURES

Figure 2.1:	An illustration of the elementary particles in the Standard Model and their properties. The three left columns represent the different generations of fermions, with quarks in purple and leptons in green. The gauge bosons are represented in the fourth column in red, and the only scalar boson, the Higgs, in the fifth column in yellow. [24]	7
Figure 3.1:	An aerial view of CERN and the LHC complex. The colored lines indicate the location of the underground tunnels of the LHC and other booster rings used to accelerate protons. [24]	11
Figure 3.2:	A schematic of the different accelerator rings used by the LHC. Protons are accelerated in a series of booster rings – the Proton Synchrotron Booster (PSB, not labeled), Proton Synchrotron (PS), and Super Proton Synchrotron (SPS) – before they are injected into the LHC and ramped up to their collision energy. Particles can be directed to collide at any of the interaction points along the ring where different detectors are situated. [24]	13
Figure 3.3:	The total integrated luminosity delivered by the LHC at a center-of-mass energy of 13 TeV compared to that recorded by CMS through 2016.	14
Figure 3.4:	Geometry of pixel tracker inner layers in CMS.	18
Figure 3.5:	Feynman diagrams depicting some processes causing showers in the ECAL. The left diagram illustrates electron-positron pair production from a photon, and the right diagram depicts bremsstrahlung, where an electron radiates energy away through a photon.	19
Figure 3.6:	Energy resolution $\sigma/E$ of the ECAL as a function of electron energy measured using a test beam. The energy was measured in a $3 \times 3$ crystal array with electrons incident on the center crystal, with electrons falling in a $4 \times 4\text{mm}^2$ region (lower points) and $20 \times 20\text{mm}^2$ region (upper points).	20
Figure 3.7:	A cross section of the ECAL geometry, with the dashed lines marking the pseudorapidity values $\eta$ covered by the various subsystems.	22
Figure 3.8:	The jet transverse energy resolution as a function of the jet transverse energy, in different regions of pseudorapidity. For an explanation of jets, see section 3.3.5	23
Figure 3.9:	Muon momentum resolution as a function of muon momentum using only the inner tracking system, only the muon system, or both combined in the barrel region (left) or endcap region (right).	25
Figure 3.10:	Layout of the CMS muon system for initial run configurations. The DT system is used only in the barrel region and CSCs in the endcap region, while RPCs are deployed in both the barrel and endcap.	26
Figure 3.11:	A graphic depiction of different particles leaving various signatures in the different CMS detector subsystems. Particles may be detected via tracks hits, energy deposits, or a combination of both.	31

Figure 4.1: Topological regions in $N_{\text{jets}}$ and $N_{\text{b-jets}}$ for the [575,1000] $H_T$ region. Within each region, the relative fraction of background events from different SM processes is shown based on simulation. . . . .	43
Figure 4.2: Signal region bins in $H_T$ and $E_T^{\text{miss}}$ (left) and $M_{\text{T2}}$ binning within each $H_T$ region (right). If simulation predicts less than one background event in the greatest $M_{\text{T2}}$ bin within a region, it is merged with the previous bin. . . . .	47
Figure 5.1: Simulated distribution of the $r_\phi$ ratio as a function of $M_{\text{T2}}$ for the low (top left), medium (top right), high (medium left), extreme (medium right), and very low (bottom) $H_T$ regions. Solid points represent the total simulated background, and hollow points show the QCD multijet contribution only. The red line and grey error band illustrates the best fit to a power law function performed in the dashed line fit window . .	56
Figure 5.2: The values of $f_j$ as measured in data in different $H_T$ regions, compared to simulation. The uncertainties include both the statistical error and the systematic sources as listed in table 5.1 . . . . .	58
Figure 5.3: The values of $r_b$ as measured in data in different $N_{\text{jets}}$ regions, compared to simulation. The uncertainties include both the statistical error and the systematic sources as listed in table 5.1 . . . . .	59
Figure 5.4: The transverse momentum of the sub-leading jet for dijet events in the monojet QCD background control region. The total yield of the simulation is normalized to the overall yield in data. . . . .	61
Figure 5.5: An illustration of “unbalanced” dijet events. As the momentum of the sub-leading jet decreases, $E_T^{\text{miss}}$ is more anti-aligned with the primary jet and approaches the topology of a monojet event. . . . .	61
Figure 5.6: The $M_{\text{T2}}$ shape in data and simulation using the single lepton CR selection, for events with zero b-tagged jets (left) or at least one b-tagged jet (right). The simulation is normalized to data in each topological region before summing to create the inclusive region. The hatched bands in each upper plot show the MC statistical uncertainty, while the shaded bands in each lower plot represent the systematic shape uncertainty. . . . .	65
Figure 5.7: The ratio of same-flavor to opposite-flavor events in a $t\bar{t}$ enriched control region, as a function of $N_{\text{jets}}$ (top left), $N_{\text{b-jets}}$ (top right), $H_T$ (bottom left), and $M_{\text{T2}}$ (bottom left). The solid black line corresponds to a constant value of $1.13 \pm 0.15$ , while the dashed black lines correspond to the statistical uncertainty and the dashed red lines the total systematic uncertainty. . . . .	72
Figure 5.8: The $M_{\text{T2}}$ shape distribution in $Z \rightarrow \nu\bar{\nu}$ simulation compared to $\gamma$ , $W \rightarrow \ell\nu$ , and $Z \rightarrow l^+l^-$ enriched samples in data, for each $H_T$ region. The solid grey band indicates the systematic uncertainty associated with the $M_{\text{T2}}$ shape modeling. . . . .	78

Figure 6.1: The data yield in each topological region compared to the pre-fit background prediction. The hatched bands illustrate the total uncertainty in the background estimate. Results in the monojet regions are binned in jet $p_T$ , while those in the multijet regions are labeled according to $N_{\text{jets}}$ and $N_{\text{b-jets}}$ . . . . .	82
Figure 6.2: The data yield in the monojet and very-low $H_T$ regions compared to the pre-fit background prediction. The hatched bands illustrate the total uncertainty in the background estimate. Results in the monojet regions are binned in jet $p_T$ in units of GeV, while those in the multijet regions are labeled according to $M_{T2}$ bin in units of GeV. . . . .	83
Figure 6.3: The data yield in the low $H_T$ and medium $H_T$ regions compared to the pre-fit background prediction. The hatched bands illustrate the total uncertainty in the background estimate. Results are labeled according to $M_{T2}$ bin in units of GeV. . . . .	84
Figure 6.4: The data yield in the high $H_T$ and extreme $H_T$ regions compared to the pre-fit background prediction. The hatched bands illustrate the total uncertainty in the background estimate. Results are labeled according to $M_{T2}$ bin in units of GeV. . . . .	85
Figure 6.5: The data yield in each topological region compared to the post-fit background prediction. The hatched bands illustrate the total uncertainty in the background estimate. Results in the monojet regions are binned in jet $p_T$ , while those in the multijet regions are labeled according to $N_{\text{jets}}$ and $N_{\text{b-jets}}$ . . . . .	87
Figure 6.6: The data yield in the monojet and very-low $H_T$ regions compared to the post-fit background prediction. The hatched bands illustrate the total uncertainty in the background estimate. Results in the monojet regions are binned in jet $p_T$ in units of GeV, while those in the multijet regions are labeled according to $M_{T2}$ bin in units of GeV. . . . .	88
Figure 6.7: The data yield in the low $H_T$ and medium $H_T$ regions compared to the post-fit background prediction. The hatched bands illustrate the total uncertainty in the background estimate. Results are labeled according to $M_{T2}$ bin in units of GeV. . . . .	89
Figure 6.8: The data yield in the high $H_T$ and extreme $H_T$ regions compared to the post-fit background prediction. The hatched bands illustrate the total uncertainty in the background estimate. Results are labeled according to $M_{T2}$ bin in units of GeV. . . . .	90
Figure 6.9: Feynman diagrams depicting the different simplified SUSY models considered in this analysis. Results are interpreted in the context of gluino-mediated bottom, top, and light-flavor squark production (top), direct production of bottom, top, and light-flavor squarks (middle), and alternate decay modes of direct top squark production (bottom). . . . .	94

Figure 6.10: 95% confidence level exclusion limits for gluino-mediated squark production of bottom (top left), top (top right), and light-flavor (bottom) squarks. Dashed red lines indicate the expected sensitivity and associated uncertainty, while black lines indicate the observed exclusion limit and its associated theoretical uncertainty based on the signal cross-section.	96
Figure 6.11: 95% confidence level exclusion limits for direct squark production of bottom (top left), top (top right), and light-flavor (bottom) squarks. Dashed red lines indicate the expected sensitivity and associated uncertainty, while black lines indicate the observed exclusion limit and its associated theoretical uncertainty based on the signal cross-section. . .	97
Figure 6.12: 95% confidence level exclusion limits for top squark production, decaying either via charginos (top left), where the chargino mass is taken as halfway-between the top squark and neutralino; a mixed mode with charginos and neutralinos (top right), where the $\tilde{\chi}^\pm$ mass is 5 GeV above the $\tilde{\chi}_1^0$ mass; or a compressed scenario, where the top squark is kinematically constrained to decay to charm quarks (bottom). Dashed red lines indicate the expected sensitivity and associated uncertainty, while black lines indicate the observed exclusion limit and its associated theoretical uncertainty based on the signal cross-section. . . . .	98
Figure 7.1: The predicted background yields compared to the observed number of events in data for pre-fit (top) and post-fit (bottom) background estimates. The $m_T$ bins are shown on the $x$ -axis, and the grey hatched band represents the total uncertainty on the background yields for the pre-fit background estimates and the fit uncertainty for the post-fit estimates. . . . .	110
Figure 7.2: 95% confidence level exclusion limits for top squark (left) and gluino (right) production. Dashed red lines indicate the expected sensitivity and associated uncertainty, while black lines indicate the observed exclusion limit and its associated theoretical uncertainty based on the signal cross-section. . . . .	111
Figure 7.3: The expected limits of the all-hadronic $M_{T_2}$ analysis compared with a hypothetical soft lepton extension. The “T2qq” model is a typical squark production model as previously shown in figure 6.11, whereas the “T5qqWW” model is a similar squark production model where the squarks decay in a cascade including charginos, which radiate W bosons that may decay to soft leptons. While the performance of the $M_{T_2}$ analysis in the hadronic model (green) is similar to the soft lepton model (blue), a soft lepton search can out-perform the all-hadronic equivalent near the diagonal where the mass splitting between the squarks and lightest supersymmetric particle is very small. . . . .	113

## LIST OF TABLES

Table 4.1:	Summary of physics objects and preselection for events. Here $R$ is the distance parameter of the anti- $k_T$ algorithm, and for veto leptons and tracks, the transverse mass $M_T$ is determined using the veto object and the $E_T^{\text{miss}}$ , while $p_T^{\text{sum}}$ denotes the sum of the transverse momenta of all the PF candidates in a cone around the lepton or track. The size of the cone, in units of $\Delta R \equiv \sqrt{(\Delta\phi)^2 + (\Delta\eta)^2}$ is given in the table. . . . .	42
Table 4.2:	$M_{T2}$ binning in the Very Low, Low, and Medium $H_T$ topological regions. . . . .	45
Table 4.3:	$M_{T2}$ binning in the High and Extreme $H_T$ topological regions. . . . .	46
Table 4.4:	Definition of "super signal regions" used in reinterpretations of the analysis. . . . .	48
Table 5.1:	Relative uncertainty of $f_j$ and $r_b$ associated with the assumed invariance with respect to $M_{T2}$ and $\Delta\phi$ (and $H_T$ for $r_b$ ). . . . .	57
Table 5.2:	The last $M_{T2}$ bin and the $M_{T2}$ extrapolation point for each topological region, beyond which shape data from simulation is used to extrapolate the lost lepton estimate into $M_{T2}$ bins. . . . .	64
Table 5.3:	The control region predicted Drell-Yan (DY) yield, SF yield, OF yield, purity (the rfraction of $Z \rightarrow l^+l^-$ events), and ratio $R_{\text{MC}}^{Z \rightarrow \nu\bar{\nu}/Z \rightarrow l^+l^-}$ for the very low, low, and medium $H_T$ topological regions. Note that the 7+ jet regions with b-tags (marked with an asterisk) share the same CR, and the fraction of events with different numbers of b-tags is folded into the ratio. . . . .	73
Table 5.4:	The control region predicted Drell-Yan (DY) yield, SF yield, OF yield, purity (the rfraction of $Z \rightarrow l^+l^-$ events), and ratio $R_{\text{MC}}^{Z \rightarrow \nu\bar{\nu}/Z \rightarrow l^+l^-}$ for the high and extreme $H_T$ topological regions. Note that the 7+ jet regions with b-tags (marked with an asterisk) share the same CR, and the fraction of events with different numbers of b-tags is folded into the ratio. . . . .	74
Table 5.5:	The $M_{T2}$ extrapolation point for the very low, low, and medium $H_T$ topological regions, beyond which shape data from simulation is used to extrapolate the invisible Z estimate into $M_{T2}$ bins. "NA" indicates regions where the simulation shape is not used at all since dilepton statistics in data are sufficiently large to perform the estimate bin-by-bin. . . . .	76
Table 5.6:	The $M_{T2}$ extrapolation point for the high and extreme $H_T$ topological regions, beyond which shape data from simulation is used to extrapolate the invisible Z estimate into $M_{T2}$ bins. "NA" indicates regions where the simulation shape is not used at all since dilepton statistics in data are sufficiently large to perform the estimate bin-by-bin. . . . .	77

Table 6.1:	Typical values of the systematic uncertainties associated with the simplified SUSY model signal yield for each interpretation in this search. Some systematics are taken as correlated amongst all signal regions; the rest are uncorrelated everywhere. Note that the large range of statistical uncertainty is driven by a small number of signal regions with low acceptance (which are not typically sensitive to those model points). . .	93
Table 6.2:	Summary of 95% CL exclusion limits on the masses of SUSY particles (sparticles) produced by various simplified models. The limit on the produced sparticle is listed for a massless $\tilde{\chi}_1^0$ , along with the greatest excluded mass of $\tilde{\chi}_1^0$ for any mass of produced sparticle. . . . .	99
Table 7.1:	Typical values of the systematic uncertainties associated with the simplified SUSY model signal yield for each interpretation in this search. . .	109

## ACKNOWLEDGEMENTS

First and foremost I want to acknowledge my entire family, namely my parents Anna Derdzinska and Kris Derdzinski, and my sisters, Andrea and Magdalena. It was at home I first discovered my love of science, and without their constant support and encouragement I would not be where I am today.

I would like to thank the entire Surf & Turf group, without whom I could not have completed this research. The support network provided by my colleagues both professionally and personally not only made this work possible, but made my life in particle physics enjoyable.

Both of my graduate advisors, Frank Würthwein and Avi Yagil, were incredibly supportive faculty mentors. Their guidance helped shape me as a physicist, and their patience granted me the opportunity to explore my other passions at the same time.

I am deeply indebted to my post-doc mentor, Giovanni Zevi Della Porta. My daily interactions with Gio were not just integral to this work, but personally rewarding. I have never met a more collegial, supportive, and patient physicist, and could not have wished for a better mentor as a graduate student.

I am very grateful to my undergraduate advisor, Yury Kolomensky, for first indulging my curiosity in particle physics. Yury gave me the opportunity to explore my interests in the field, and his thoughtful mentorship set me on the path to where I am today.

Finally, I would like to acknowledge the thousands of faculty, students, and staff that

make experiments like the LHC and CMS possible. This work could not have happened without all the unnamed scientists that laid the foundation before me, and I am eternally grateful for being given the opportunity to contribute to the legacy of our field.

In particular, I would like to congratulate everyone in the CERN accelerator departments for the excellent performance of the LHC and thank the technical and administrative staffs at CERN and at other CMS institutes for their contributions to the success of the CMS effort. In addition, I gratefully acknowledge the computing centers and personnel of the Worldwide LHC Computing Grid for delivering so effectively the computing infrastructure essential to our analyses. Lastly, I acknowledge the enduring support for the construction and operation of the LHC and the CMS detector provided by the following funding agencies: BMWFW and FWF (Austria); FNRS and FWO (Belgium); CNPq, CAPES, FAPERJ, and FAPESP (Brazil); MES (Bulgaria); CERN; CAS, MoST, and NSFC (China); COLCIENCIAS (Colombia); MSES and CSF (Croatia); RPF (Cyprus); SENESCYT (Ecuador); MoER, ERC IUT, and ERDF (Estonia); Academy of Finland, MEC, and HIP (Finland); CEA and CNRS/IN2P3 (France); BMBF, DFG, and HGF (Germany); GSRT (Greece); OTKA and NIH (Hungary); DAE and DST (India); IPM (Iran); SFI (Ireland); INFN (Italy); MSIP and NRF (Republic of Korea); LAS (Lithuania); MOE and UM (Malaysia); BUAP, CINVESTAV, CONACYT, LNS, SEP, and UASLP-FAI (Mexico); MBIE (New Zealand); PAEC (Pakistan); MSHE and NSC (Poland); FCT (Portugal); JINR (Dubna); MON, RosAtom, RAS, RFBR and RAEP (Russia); MESTD (Serbia); SEIDI, CPAN, PCTI and FEDER (Spain); Swiss Funding Agencies (Switzerland); MST (Taipei); ThEPCenter, IPST, STAR, and NSTDA (Thailand); TUBITAK

and TAEK (Turkey); NASU and SFFR (Ukraine); STFC (United Kingdom); DOE and NSF (USA).

## VITA

- 2011            B. A. in Physics and Mathematics, University of California, Berkeley  
2015            M. S. in Physics, University of California, San Diego  
2018            Ph. D. in Physics, University of California, San Diego

## PUBLICATIONS

**Search for new physics with the  $M_{T2}$  variable in all-jets final states produced in pp collisions at  $\sqrt{s} = 13$  TeV, CMS Collaboration, *J. High Energ. Phys.* **10** (2016) 006, arXiv:1603.04053 [hep-ex]**

**Search for new physics in the one soft lepton final state using 2015 data at  $\sqrt{s} = 13$  TeV, CMS Collaboration, Physics Analysis Summary (2016), CMS-PAS-SUS-16-011, cds.cern.ch/record/2161097**

**Search for new phenomena with the  $M_{T2}$  variable in the all-hadronic final state produced in proton-proton collisions at  $\sqrt{s} = 13$  TeV, CMS Collaboration, *Eur. Phys. J. C* **77** (2017) no. 10, 710, arXiv:1705.04650 [hep-ex]**

## ABSTRACT OF THE DISSERTATION

**A search for new physics using the  $M_{T2}$  variable in all-hadronic final states produced in proton-proton collisions with a center of mass energy of 13 TeV**

by

Mark Derdzinski

Doctor of Philosophy in Physics

University of California, San Diego, 2018

Professor Frank Würthwein, Chair

A search for physics beyond the Standard Model (SM) is performed in events with final states including hadronic activity, missing energy, and significant momentum imbalance as measured with the  $M_{T2}$  variable. The results are based on data collected by the Compact Muon Solenoid detector at the Large Hadron Collider, and correspond to a total integrated luminosity of  $35.9 \text{ fb}^{-1}$  of proton-proton collisions at a center-of-mass energy of 13 TeV. No significant excess above the predicted SM background is observed. The results are interpreted as 95% confidence-level exclusion limits on the masses of hypothesized

particles in a variety of simplified models of  $R$ -parity conserving supersymmetry (SUSY). Additional techniques for extending the search into final states with low-momentum leptons to target natural SUSY models in ewkino decays is discussed, and compared to the exclusion strength of a typical all-hadronic targeting such models.

# Chapter 1

## Introduction

This dissertation documents a search for new physics in proton-proton collisions at the Large Hadron Collider, with data collected by the Compact Muon Solenoid at a center-of-mass energy of 13 TeV. The current state of particle physics and motivations for such a search are summarized in Chapter 2, including the current understanding of the Standard Model of Particle Physics and theorized extensions of the Standard Model which motivate these physics searches.

Chapter 3 describes the experimental apparatus used to collect the data analyzed in this analysis. Section 3.1 describes the physics of the Large Hadron Collider which delivers protons to the collision point, and section 3.2 details the different subsystems of the Compact Muon Solenoid detector which collect particle data from collisions. The data are reconstructed into abstract physics objects as described in section 3.3, which are subsequently analyzed in this search for new physics.

Chapters 4, 5, and 6 describe the analysis design and execution. In chapter 4,

the overall analysis strategy and signal definitions are discussed, and in chapter 5 the background predictions are described in detail. Chapter 6 presents the results of the search, including interpretations constraining parameters of new physics models.

Finally, chapter 7 presents an extension of the all-hadronic search that targets specific signatures motivated by new physics models and limitations of the typical all-hadronic analysis. A pilot analysis of this type was presented in [21].

The all-hadronic analyses detailed in this dissertation are published in [32] and [48].

# Chapter 2

## Theory and Motivation

Particle physics is concerned with the study of the most fundamental constituents of nature and the rules that govern their interactions. Over the course of the twentieth century, physicists developed models using quantum field theory to describe the fundamental forces binding elementary particles together, and experimentalists discovered an abundance of particles predicted by such theories. Today, the Standard Model of particle physics represents the best experimental verified theoretical framework for describing the elementary components of the universe, and experimental particle physicists work in tandem with theorists to identify possible extensions to the Standard Model which may explain some theoretical and experimental issues with the current framework.

## 2.1 The Standard Model of Particle Physics

The Standard Model (SM) is a quantum field theory which describes the fundamental particles which make up the universe and the various interactions between those particles [27, 51, 45]. It is widely regarded as one of the most successful theories ever constructed to describe nature, and has been rigorously verified experimentally. The announcement in 2012 by the ATLAS [4] and CMS [19] detectors of a new particle consistent with the Higgs Boson marked the discovery of the last fundamental particle predicted by the SM over 50 years before its discovery, and many precision measurements of the Standard model parameters have been verified to better than one part in a billion.

The SM classifies all the elementary particles into two categories, depending on their intrinsic angular momentum, *spin*. Particles with a half-integer spin are known as *fermions* while those with integer spin are referred to as *bosons*. Fermions obey the Pauli exclusion principle (where identical fermions cannot occupy the same quantum state), and are often thought of as the constituents of matter. Bosons are not subject to the Pauli exclusion principle, and are often thought of as the “force carriers” which mediate different fundamental forces between different particles. The various fundamental particles of the SM and their properties are detailed in figure 2.1.

Fermions can be divided into two groups, *leptons* and *quarks*. Both leptons and quarks can be further divided into two subgroups based on their electromagnetic charge. Charged leptons carry either positive or negative charge  $e$  (where  $e$  is the fundamental charge constant), whereas the neutral leptons known as *neutrinos* carry no electromag-

netic charge. Different species of quarks can be either positively charged ( $+2/3e$ ) or negatively charged ( $-1/3e$ ). Both leptons and quarks can also be divided into three “flavors” of particles grouped into different families with similar electromagnetic properties but different masses. The leptons in order of increasing mass are *electron*, *muon*, or *tau* flavored (with both charged lepton and neutrino species), and the quarks are grouped into *up/down*, *charmed/strange*, and *top/bottom* pairs (that are positively and negatively charged, respectively).

The bosons of the standard model are associated with the different fundamental forces by which particles (including the bosons themselves) interact. The Standard Model Lagrangian is invariant under local transformations of an  $SU(3) \times SU(2) \times U(1)$  gauge symmetry, and the various gauge symmetries correspond to different forces through which particles interact.  $SU(3)$  is associated with the Quantum Chromodynamics (QCD) color charge (or strong force), and mediated by the *gluon* which binds quarks together (leptons are represented by an  $SU(3)$  singlet and do not interact via the strong force). The  $SU(2) \times U(1)$  groups are associated with weak isospin and hypercharge respectively, and responsible for electroweak interactions between particles, mediated by the  $W^\pm$  and  $Z$  bosons and the *photon*,  $\gamma$ .

While the gauge symmetries of the standard model are preserved, explicit mass terms are forbidden in the Lagrangian and the associated gauge bosons might otherwise remain massless. However, the SM Lagrangian also includes a complex scalar doublet which allows for the Higgs mechanism; the neutral component of the scalar doublet acquires a non-zero vacuum expectation value which manifests as the *Higgs boson*, and the other

degrees of freedom become Goldstone bosons which grant mass to the  $W^\pm$  and  $Z$  bosons. In this manner the electroweak  $SU(2) \times U(1)$  is spontaneously broken into the familiar weak and electromagnetic forces.

## 2.2 Issues with the Standard Model

Despite the great success of the Standard Model in describing many of the fundamental interactions of particles, it is insufficient to explain all physical phenomena. There are several outstanding theoretical questions left unanswered by the Standard Model, and experimental evidence to suggest it is incomplete.

One of the most perplexing theoretical features of the SM is the fact that we have been able to detect all the elementary particles at energies accessible in our experiments. Because the bare masses of particles in the SM Lagrangian receive corrections from quantum loop diagrams, it is not clear why new particles (which must be massive) do not contribute significantly to these corrections. In particular, the quantum loop corrections to the Higgs boson mass include all massive particles, and contributions from undiscovered massive particles could drive the Higgs mass far beyond what is currently accessible, yet this is not observed. This is often referred to as the *hierarchy problem*.

Experimental evidence also suggests there are physical phenomena not explained by the SM. Measurements of the rotational velocity of galaxies compared to the visible matter indicate there is an abundance of *dark matter* in the universe which cannot be accounted for by the particle content of the SM [22]. Furthermore, while the SM predicts

# Standard Model of Elementary Particles

three generations of matter (fermions)					
	I	II	III		
QUARKS	mass $\approx 2.4 \text{ MeV}/c^2$	mass $\approx 1.275 \text{ GeV}/c^2$	mass $\approx 172.44 \text{ GeV}/c^2$	mass $0$	SCALAR BOSONS
	charge 2/3	charge 2/3	charge 2/3	charge 0	
	spin 1/2	spin 1/2	spin 1/2	spin 0	
	u	c	t	g	
	up	charm	top	gluon	
	$\approx 4.8 \text{ MeV}/c^2$	$\approx 95 \text{ MeV}/c^2$	$\approx 4.18 \text{ GeV}/c^2$	$\approx 125.09 \text{ GeV}/c^2$	
	-1/3	-1/3	-1/3	0	
	1/2	1/2	1/2	0	
	d	s	b	H	
LEPTONS	down	strange	bottom	photon	GAUGE BOSONS
	$\approx 0.511 \text{ MeV}/c^2$	$\approx 105.67 \text{ MeV}/c^2$	$\approx 1.7768 \text{ GeV}/c^2$	Z boson	
	-1	-1	-1	0	
	1/2	1/2	1/2	1	
	e	$\mu$	$\tau$	Z	
	electron	muon	tau	W boson	
	$<2.2 \text{ eV}/c^2$	$<1.7 \text{ MeV}/c^2$	$<15.5 \text{ MeV}/c^2$	$\approx 80.39 \text{ GeV}/c^2$	
	0	0	0	$\pm 1$	
	1/2	1/2	1/2	1	
	$\nu_e$	$\nu_\mu$	$\nu_\tau$	W	
	electron neutrino	muon neutrino	tau neutrino		

**Figure 2.1:** An illustration of the elementary particles in the Standard Model and their properties. The three left columns represent the different generations of fermions, with quarks in purple and leptons in green. The gauge bosons are represented in the fourth column in red, and the only scalar boson, the Higgs, in the fifth column in yellow. [24]

neutrinos to be massless, measurements of neutrino flavor oscillations imply that neutrinos mass is very small, but nonzero [9]. Such measured phenomena indicate there may be additional particle content beyond what is posited by the SM, and additional interaction terms between SM particles and a “dark sector” of weakly-interacting particles.

## 2.3 Beyond the Standard Model: Supersymmetry

In order to solve many of the theoretical and experimental issues with the SM, theorists had considered extending SM particle content and interactions to include additional species which might satisfy some of the theoretical constraints of the SM in a consistent manner with observation. However, in 1975 the Haag-Łopuszański-Sohnius theorem [29] demonstrated that the only non-trivial extensions of quantum theories do not only include internal symmetries and the Poincaré symmetry, but also a non-trivial extension of the Poincaré algebra known as *supersymmetry* [43, 40, 28, 41, 26, 53, 52, 50].

A quantum field theory of supersymmetry (SUSY) can be visualized as a dual version of a typical field theory. For each particle, there exists a superpartner with different spin; fermions have boson-like superpartners and bosons have fermion-like superpartners. This is a particularly appealing and elegant solution to many of the issues with the SM; loop diagram corrections to particle mass are partially cancelled out by contributions from superpartner loop diagrams, providing a natural solution to the hierarchy problem [39]. In typical “R-parity conserving” SUSY theories, particle interactions also conserve “SUSYness” in decays, and thus when a superparticle decays into SM particles, the cascade

will always end in the lightest supersymmetric particle (LSP). The LSP must be stable, and because it interacts very weakly with the SM sector provides a suitable dark matter candidate.

While there are many beyond-SM (BSM) theories that seek to explain phenomena beyond the scope of the SM, SUSY provides both elegant solutions to the theoretical concerns of the SM as well as a robust framework to unexplained physical phenomena. The analysis described here is designed to be model independent in a search for new physics, but also sets constraints on SUSY models as it is one of the more promising BSM theories that might be realized by nature.

# Chapter 3

## The Large Hadron Collider and the CMS Detector

In order to probe the most fundamental constituents of nature, accelerators ramp particles up to great energies and then collide them to probe particle interactions. Detectors situated at the collision point can measure the outgoing products from particle collisions, and physicists can study the interactions to measure SM parameters, determine particle properties, quantify interaction rates, or search for new particles and processes.

The Large Hadron Collider is the most powerful particle accelerator ever constructed, and collides protons at a rate of nearly one billion times per second at a record energy of 13 Teraelectronvolts. The Compact Muon Solenoid is one of the all-purpose physics detectors that monitors the products of proton-proton collisions delivered by the LHC. Together with the ATLAS detector (A Toroidal LHC ApparatuS), the CMS detector is responsible for collecting data to measure a wide range of physics phenomena.



**Figure 3.1:** An aerial view of CERN and the LHC complex. The colored lines indicate the location of the underground tunnels of the LHC and other booster rings used to accelerate protons. [24]

### 3.1 The Large Hadron Collider

The Large Hadron Collider (LHC) is the world's largest and most powerful particle accelerator ever constructed [25]. The accelerator was constructed and is operated by the European Organization for Nuclear Research (CERN), and straddles the border between Switzerland and France near Geneva. The accelerator tunnels of the LHC are 27 kilometers in circumferences and 50-175 meters underground, as well as additional, smaller rings used to accelerate protons before they are injected into the LHC. An aerial view of the LHC layout and location of the different experiments is shown in figure 3.1.

The protons delivered by the LHC are accelerated in stages before reaching final collision energy. First, protons are accelerated to 50 MeV by a linear accelerator before being injected into the Proton Synchrotron Booster (PSB). The PSB accelerates protons to 1.4 GeV before they are injected into the Proton Synchrotron (PS) and accelerated to 26 GeV, then injected into the Super Proton Synchrotron (PSP) and accelerated to 450 GeV. Finally the protons are injected into the LHC and directed in two parallel beamlines in opposite directions to a beam energy of 6.5 TeV. A schematic representation of the different boost rings is illustrated in figure 3.2.

The total amount of proton-proton collisions delivered by the LHC is often measured by the *integrated luminosity*. The *instantaneous luminosity* ( $L$ ) is a measure of the number of interactions that can be produced per unit area per second, and the integrated luminosity ( $\mathcal{L}$ ) is the total luminosity integrated over some time interval. Integrated luminosity is thus a unit of inverse area and typically measured in barns (1 barn = 100 fm<sup>2</sup>). The total number of a particular type of event measured by a detector  $N_{\text{events}}$  is the product of the integrated luminosity, the cross section for that particular process ( $\sigma$ ), and the detector-determined efficiency ( $\epsilon$ ) as described in equation 3.1. The total integrated luminosity delivered by the LHC compared that recorded by CMS is illustrated in figure 3.3.

$$N_{\text{events}} = \mathcal{L} \cdot \sigma \cdot \epsilon \quad (3.1)$$

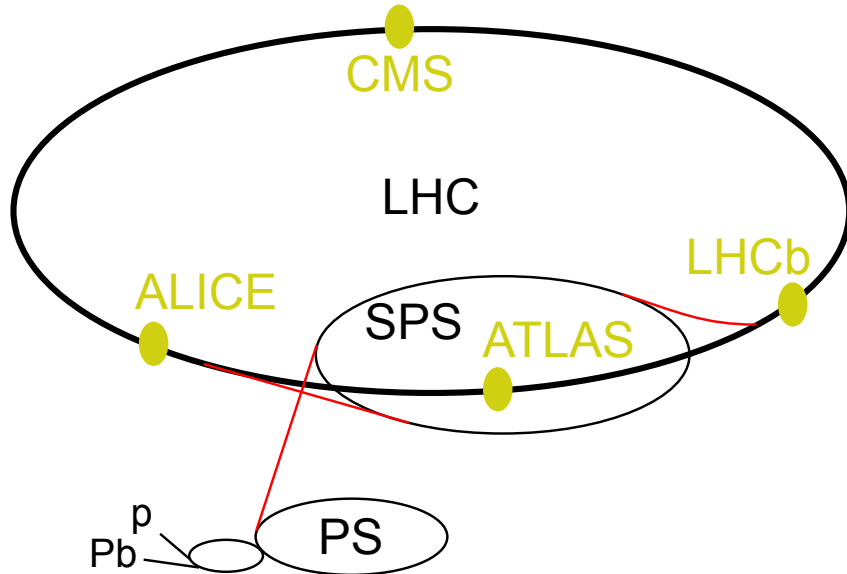


**Figure 3.2:** A schematic of the different accelerator rings used by the LHC. Protons are accelerated in a series of booster rings – the Proton Synchrotron Booster (PSB, not labeled), Proton Synchrotron (PS), and Super Proton Synchrotron (SPS) – before they are injected into the LHC and ramped up to their collision energy. Particles can be directed to collide at any of the interaction points along the ring where different detectors are situated.

[24]

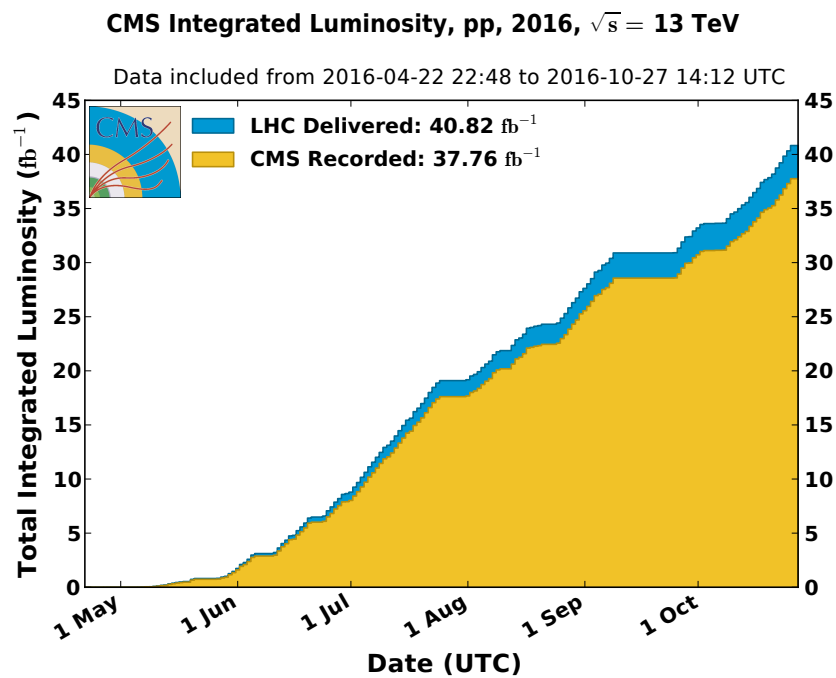


**Figure 3.3:** The total integrated luminosity delivered by the LHC at a center-of-mass energy of 13 TeV compared to that recorded by CMS through 2016.

### 3.1.1 Proton Bunches and Pileup

The protons delivered by the LHC are not in a continuous stream, but separated into “bunches” so that interactions occur at discrete intervals. Each proton bunch is approximately 30 centimeters long and contains over 100 billion protons at the beginning of the machine fill. Proton bunches are injected into the LHC and stored with a bunch spacing of 25ns (or 40 MHz), where they can be accelerated and for hours while collisions occur at the interaction points.

Because protons are delivered in discrete bunches at such a high rate, any bunch crossing results in multiple interactions and outgoing products. This is known as *pileup*, and presents a significant challenge for physics detectors which must be able to associate outgoing products to a specific interaction. *In-time pileup* is caused by multiple interactions per bunch crossing (the majority of interaction in a given bunch crossing are soft proton-proton inelastic scattering), and *out-of-time pileup* is due to interactions from a different bunch crossing (such as the read-out time of a detector subsystem). An effective detector needs to correctly identify which particles are associated with the interaction of interest in any given event, and mitigate the effects of pileup in design and construction.

## 3.2 The Compact Muon Solenoid

The Compact Muon Solenoid (CMS) is a general-purpose physics detector at the LHC, situated at one of the five collision points along the main ring [16, 12]. The detector encapsulates the collision point with layers of various subsystems designed to interact

with the outgoing particles of the proton-proton collisions, and measure the position and energies of the collision products. Because of the extremely high rate of interactions at the collision point (on the order of one billion interactions per second), saving data from every bunch crossing would be unsustainable, and so the detector is also equipped with a system of hardware and software implemented "triggers" which identify events of interest for physics analyses to be saved to disk for further analysis.

The physical construction of the detector is motivated by the different interaction of particles with different types of materials, and consists of several subsystems layered as coaxial cylinders around the interaction point. Each subsystem consists of (sometimes different) components covering the fiducial area coaxial with the beamline (the *barrel*) and also the ends of the cylinder (the *endcap*). The innermost subsystem of CMS is the silicon tracker, which consists of many layered silicon pixels designed to pinpoint the locations of charged particles while minimally interacting with the particle's trajectory. The layer beyond the tracker is the electromagnetic calorimeter (ECAL), a grid of lead-tungstate crystals which scintillate to measure the energies of electromagnetic particles. Beyond the ECAL is the hadronic calorimeter (HCAL), a sampling calorimeter designed to measure the energies of hadronic particles (which deposit minimal energy in the ECAL). The final, outer layer is the CMS muon detector, where the muon detection stations are interweaved with the magnetic return yoke that generates the toroidal 3.8T magnetic field inside the detector volume. The total dimensions of the detector are 21.6m long and 14.6m in diameter, weighing over 12,500 tons.

### 3.2.1 Silicon Tracker

The silicon vertex tracker (SVT) is a series of silicon pixels and strips designed to measure the position of charged particles in the detector, while disturbing their path as little as possible. The position of particles in the interior is of particular importance in event reconstruction; charged particles traveling in a magnetic field will deflect in a curved path with radius proportional to the particles momentum as described in equation 3.2, and so the track reconstruct can be used to not only determine a particle's momentum with high precision, but also the sign of its charge based on the direction of curvature.

$$p = qrB \quad (3.2)$$

As the innermost detector subsystem, the SVT experiences the highest flux of particle radiation. In the barrel region, the tracker layers are oriented in 3 coaxial layers. Closest to the interaction point where particle flux is the greatest, very precise silicon pixels are used, measuring  $100 \times 150\mu\text{m}^2$ , whereas in other layers the flux is low enough to use microstrip detectors, measuring  $10\text{cm} \times 80\mu\text{m}$  and  $25\text{cm} \times 180\mu\text{m}$  in the middle and outer layers respectively. In the endcaps, the pixel strips are arranged in a turbine-like pattern in two separate layers on each end. This configuration allows for the precise measurement of particle position for track reconstruction, while minimizing the amount of material which might deflect particles from their original trajectories. A partial geometry of the pixel layers in the SVT is shown in figure 3.4.

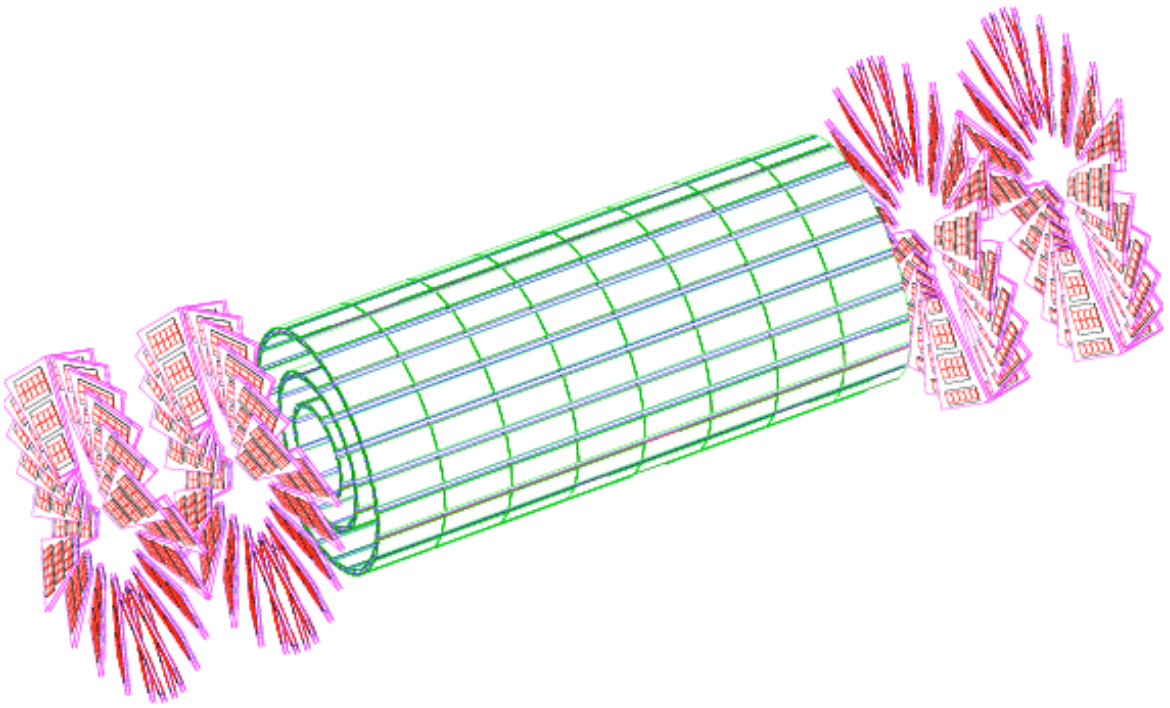


**Figure 3.4:** Geometry of pixel tracker inner layers in CMS.

### 3.2.2 Electromagnetic Calorimeter

The ECAL is used to measure the energies of particles which interact electromagnetically, both absorbing the incident particles and scintillating to provide an energy-readout to photodiodes attached to each crystal. Constructed of lead-tungstate ( $\text{PbWO}_4$ ), electromagnetically interacting particles (such as electrons or photons) will interact with the crystal material, losing energy through a cascade of electromagnetic interactions including electron-positron pair production and bremsstrahlung as shown in figure 3.5. This phenomenon — also referred to as "showering" — causes the crystals to scintillate proportional to the energy deposited in the crystal, which is then measured by various photodiodes to extract an accurate measurement of the particle energy, now fully absorbed by the

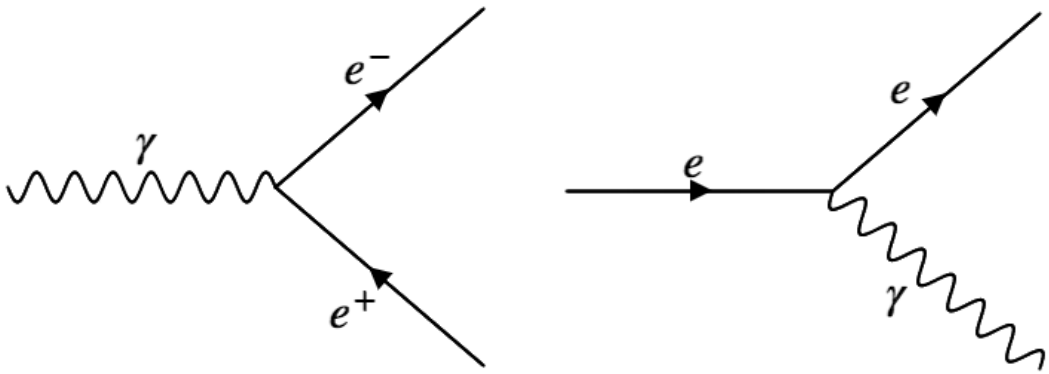


**Figure 3.5:** Feynman diagrams depicting some processes causing showers in the ECAL.

The left diagram illustrates electron-positron pair production from a photon, and the right diagram depicts bremsstrahlung, where an electron radiates energy away through a photon.

calorimeter.

The fundamental principle of the calorimeter measurement relies on the energy loss of particles interacting with matter. In general, the energy of a particle traveling a distance  $X$  through some material is given by equation 3.3, where  $E_0$  is the initial energy of the particle and  $X_0$  is the material-dependent radiation length.

$$E(x) = E_0 e^{\frac{-x}{X_0}} \quad (3.3)$$

The design of the calorimeter is motivated by the choice of a scintillating, radiation-hard material with short  $X_0$  such that incident electromagnetic particles deposit all their energy and are stopped by the ECAL. The resolution of the energy measurement is also dependent on the "stochastic term", which parametrizes the uncertainty due to statistical and measurement fluctuations in the calorimeter, and is given by equation 3.4, where  $S$  is

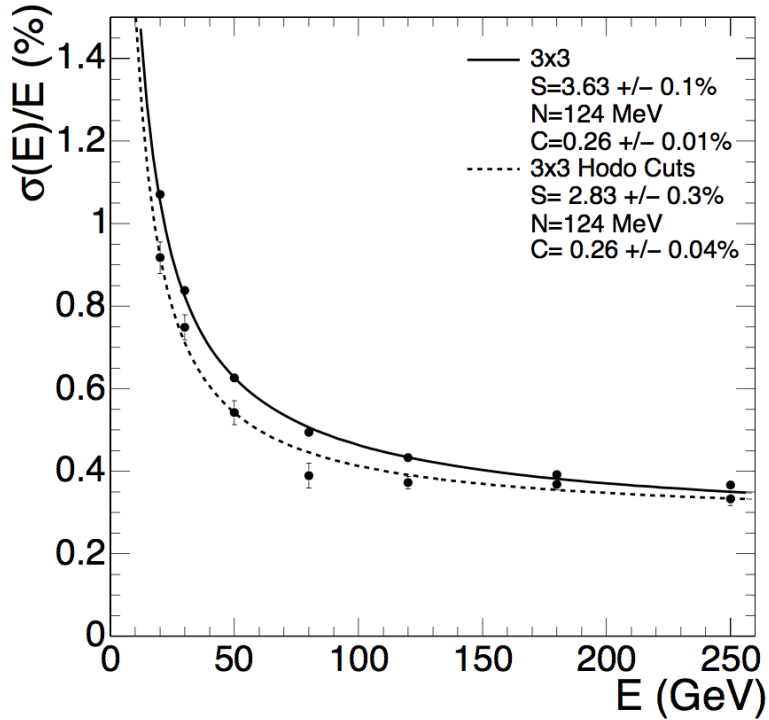


**Figure 3.6:** Energy resolution  $\sigma/E$  of the ECAL as a function of electron energy measured using a test beam. The energy was measured in a  $3 \times 3$  crystal array with electrons incident on the center crystal, with electrons falling in a  $4 \times 4\text{mm}^2$  region (lower points) and  $20 \times 20\text{mm}^2$  region (upper points).

the stochastic term,  $N$  the noise, and  $C$  the constant term.

$$\left(\frac{\sigma}{E}\right)^2 = \left(\frac{S}{\sqrt{E}}\right)^2 + \left(\frac{N}{E}\right)^2 + C^2 \quad (3.4)$$

The energy resolution can be measured by a test beam of known energy, as shown in figure 3.6.

The construction of the calorimeter is also divided into two sections by the cylindrical geometry, the ECAL barrel section (EB) and ECAL endcap sections (EE). The EB consists of 61,200 crystals arranged into 36 "supermodules", each spanning half the barrel

length, and uses silicon avalanche photodiodes (APDs) as photodetectors. The individual crystals are tilted slightly ( $3^\circ$ ) in an  $\eta - \phi$  grid with respect to the nominal interaction point, with a front-facing area of  $22 \times 22\text{mm}^2$  and a length of 230mm. The EE instead uses vacuum phototriodes (VPTs) as photodetectors, and consists of approximately 15,000 crystals clustered in  $5 \times 5$  units, also offset from the interaction point but arranged in an  $x - y$  grid, with a cross section of  $28.6 \times 28.6\text{mm}^2$  and a length of 220mm. The EE is also equipped with a "preshower" device placed in front of the crystal calorimeter, consisting of two strips of silicon strip detectors to enhance  $\pi^0$  rejection. The layout of the ECAL can be seen in figure 3.7. Because of the depth of the ECAL crystals (which are  $\sim 25X_0$ , and the confining properties of the crystals (which have a Moliere radius of 2.2cm, the radius of a cylinder containing 90% of a shower's energy on average), electrons and photons are typically well reconstructed in CMS, except in the transition region where EB and EE meet.

### 3.2.3 Hadronic Calorimeter

The CMS HCAL is a sampling calorimeter. Designed with alternating layers of scintillating and absorbing material, incident hadronic particles (such as charged pions, kaons, protons, etc.) interact with the absorber material and consequently shower into electromagnetic particles, whose energy can be read out by photodiodes connected to the scintillating material. Brass is used as the absorber material for both its interaction length and non-magnetic properties, and plastic scintillator tiles connected to embedded wavelength-shifting fibers carry the light to a readout system.

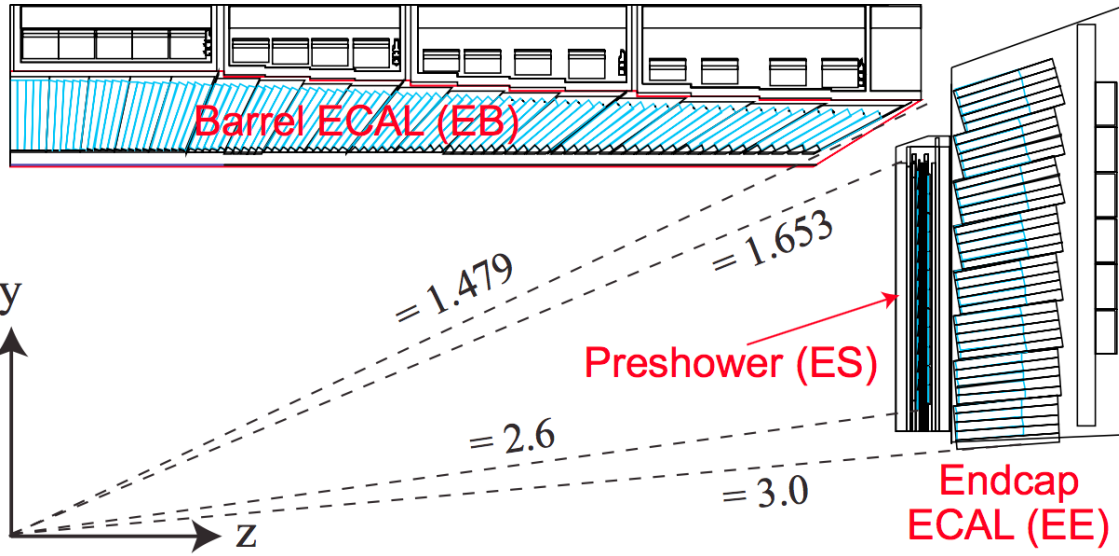


**Figure 3.7:** A cross section of the ECAL geometry, with the dashed lines marking the pseudorapidity values  $\eta$  covered by the various subsystems.

As with the ECAL, the energy loss of hadronic particles in the absorber is characterized by the (hadronic) interaction length and equation 3.3. However, unlike the ECAL, the HCAL contains both hadronic and electromagnetic showers. Electromagnetic particles generated in hadronic showers often fail to escape the absorber layers, and thus some electromagnetic energy is lost in the absorbers. The CMS HCAL is sometimes referred to as a *non-compensating calorimeter* because it is not constructed to actively compensate for the energy lost to these electromagnetic effects and the energy measurements must be corrected offline, known as "jet energy corrections" (JECs). JECs are typically calculated by examining data from collisions producing a boson recoiling against hadronic particles. By accurately measuring the boson energy in the ECAL, the sum of the recoiling hadronic energy in the HCAL is inferred (by momentum conservation) and compared to the de-

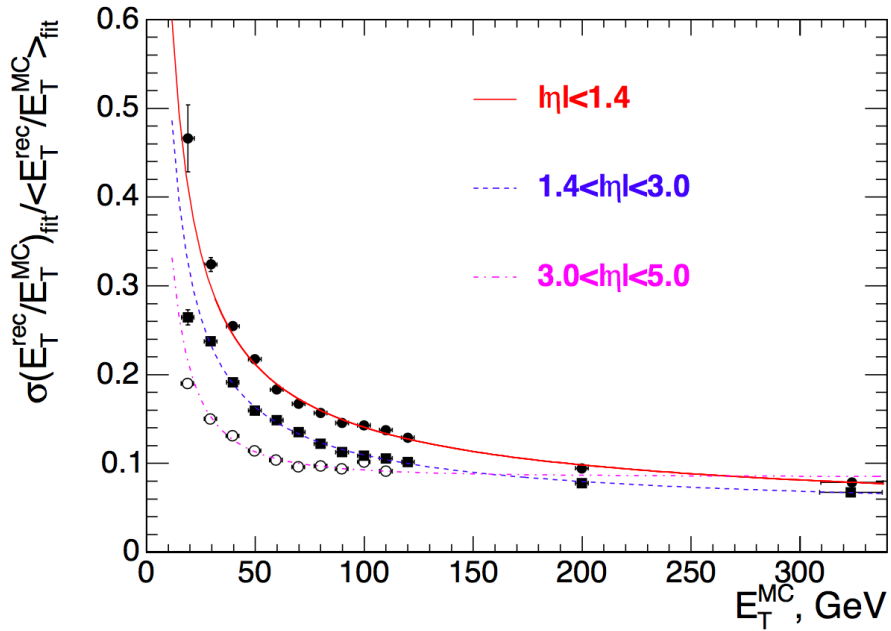


**Figure 3.8:** The jet transverse energy resolution as a function of the jet transverse energy, in different regions of pseudorapidity. For an explanation of jets, see section 3.3.5

tector response. Because the performance of the HCAL can fluctuate with time and run conditions, JECs are regularly recalculated and applied to the raw energy measurements taken by the HCAL to compensate for these effects. Additional information on the corrections contained in JECs is detailed in section 3.3.5. The energy resolution of the HCAL in different regions of pseudorapidity can be seen in figure 3.8.

The geometry of the HCAL can be reduced to four sections. The HCAL barrel (HB) consist of 32 "towers" of alternating absorber/scintillator material spanning the pseudorapidity region  $-1.4 < \eta < 1.4$ . The HCAL outer (HO) detector lies outside the vacuum tank of the magnetic coil and measures energy from any hadronic particles "leaking" through the HB, covering the pseudorapidity region  $-1.26 < \eta < 1.26$ . The HCAL

endcap (HE) consists of 14  $\eta$  towers spanning the pseudorapidity range  $1.3 < |\eta| < 3.0$ . Finally, the HCAL forward (HF) is a different steel/quartz fibre calorimeter spanning the very-forward  $3.0 < |\eta| < 5.0$  region. Instead utilizing Cherenkov radiation generated in the quartz fibers, the HF preferentially samples neutral hadronic energy and is ideally designed for the hadronic-heavy radiation environment in the forward region.

### 3.2.4 Muon Detectors

The muon detector is the only subsystem which is constructed outside of the toroidal magnetic field. Interleaved with the magnetic return yoke, different muon detectors are used to aid in the identification and reconstruction of muon tracks. Because muons typically penetrate every other layer of the detector and have a large bending radius, additional measurements in the muon system — combined with measurements in the SVT — can lead to vastly improved resolution of muon momentum. The non-uniform magnetic field in the muon detector region (beyond the toroidal regime) causes an s-shaped trajectory and tighter bending radius (than in the SVT) for the muons, which improves the resolution for particles with transverse momentum above  $\sim 200\text{GeV}$  as seen in figure 3.9.

Different types of muon detectors are deployed (sometimes in combination) in different sections of the full muon system. In the barrel region ( $-1.2 < \eta < 1.2$ ) where the muon flux, neutral background, and magnetic field are small, drift tube (DT) chambers are used. In the endcaps where the the muon flux, neutral background, and magnetic field are much greater, cathode strip chambers (CSCs) are used to increase coverage up to  $|\eta| < 2.4$ . In addition to these technologies, both the barrel and endcap systems are supplemented

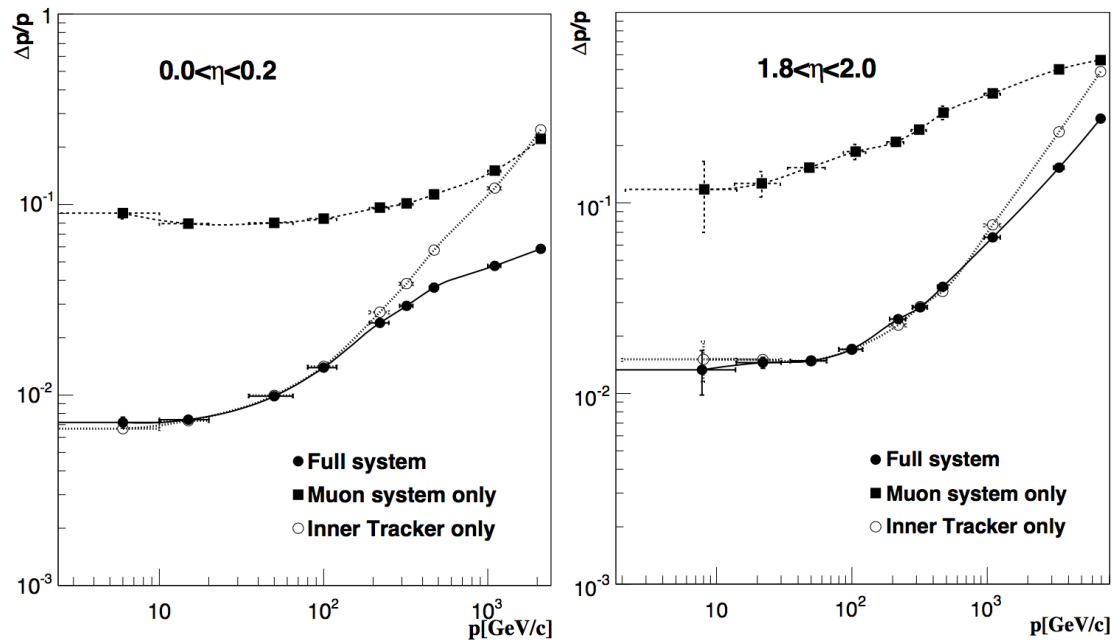


**Figure 3.9:** Muon momentum resolution as a function of muon momentum using only the inner tracking system, only the muon system, or both combined in the barrel region (left) or endcap region (right).

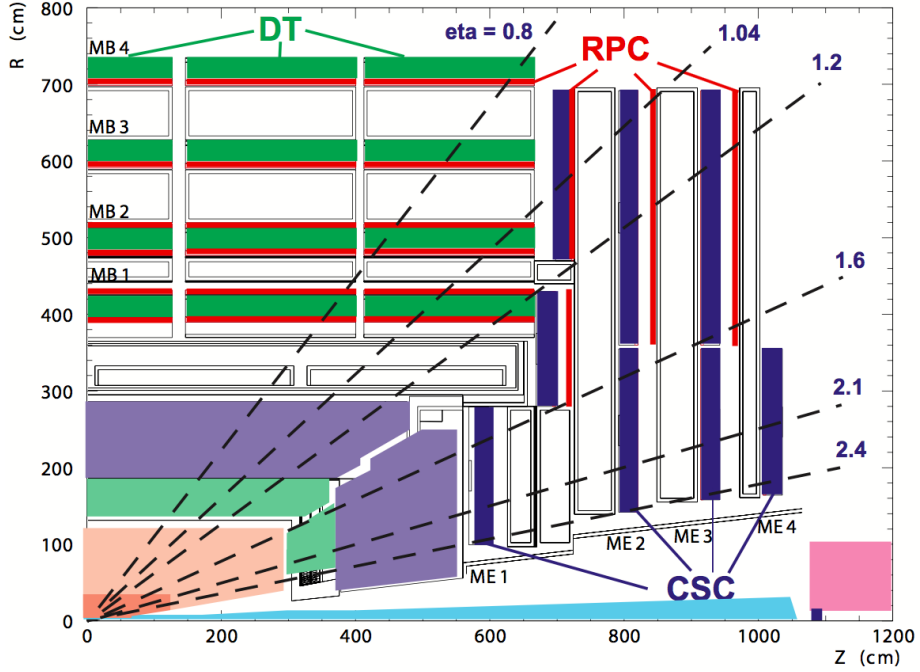


**Figure 3.10:** Layout of the CMS muon system for initial run configurations. The DT system is used only in the barrel region and CSCs in the endcap region, while RPCs are deployed in both the barrel and endcap.

with resistive plate chambers (RPCs) to provide complementary information to the DT and CSC detectors. The layout of the different muon detector components in the barrel and endcap can be seen in figure 3.10.

The DT detectors are chambers filled with gas surrounding a wire, with a voltage difference between the wire and outside of the DT. When charged particles pass through the drift chamber, they ionize the gas, and the ionization products will drift across the voltage difference in the tube, resulting in a detectable voltage change in the DT. By measuring both the position along the DT wire where charge is deposited, as well as reconstructing the "drift time" it takes for the ionized particles to reach the wire, DTs

provide a 2-dimensional measurement of a particle’s position. In CMS, the DT chambers consist of a dozen layers arranged into 3 groups, each with up to 60 DTs. The layers are arranged in such a way that some measure the direction of the muon parallel to the proton beam and others along the perpendicular coordinate, such that the full muon trajectory can be reconstructed by using the DT station information.

The CSCs in each endcap are trapezoidal in shape and overlap in the phi coordinate, increasing the fiducial coverage of the muon system. Each CSC consists of 6 gas gaps, where each gap is comprised of radially aligned cathode strips and a plane of anodes wires nearly perpendicular to the strips. When a muon passes through the CSCs, the ensuing ionization and electron avalanche deposits a charge on the anode wire and an image charge on the cathode strips. A measurement of the muon position can be reconstructed by determining the center-of-gravity of the charge distribution on the cathode strips, and the fast readout of the anode wire is used in low-latency trigger decisions as described in section 3.2.5.

The RPCs are complementary systems in both the barrel and endcap used to improve the time resolution of muon measurements. Each RPC consists of two parallel anode and cathode plates, separated by a gas chamber. The ionization of the gas as muons travel through the chamber is quickly deposited on the plates, and used for a precise time measurement of the muon crossing. Though the spatial resolution of the RPCs is poor, in conjunction with the other muon systems they allow for an unambiguous association of muons with different bunch crossings.

### 3.2.5 Trigger Systems

When operating at design luminosity, the LHC can deliver proton bunches to the collision point at a rate of 40MHz, resulting in an average collision rate on the order of one billion collisions per second. In order to achieve reasonable rates of data collection for offline storage and processing, the detector must suppress the event rate by six orders of magnitude when selecting events of interest to be saved for physics analyses. This is accomplished through a combination of readout electronics and the trigger systems: the Level-1 trigger (L1) processors and online High-Level triggers (HLT) [38].

The L1 trigger system is comprised of specialized hardware processors to rapidly pre-select events of interest based on the calorimeter and muon systems. Based on the beam crossing frequency, the L1 electronics have only a few microseconds to collect readout data from the front end electronics and execute logic to select events of interest, such that the total time allotted for L1 trigger calculations is  $< 1\mu s$ . During this time the bulk of detector data is held in a buffer while L1 trigger decisions are made based on data with reduced granularity and resolution rapidly collected from the calorimeter and muon systems, where triggers typically check for "trigger primitive" objects (such as photons, muons, electrons, etc.). Trigger primitives must meet certain momentum or energy thresholds, and L1 triggers may also check global data about the event such as the sum of transverse energy or the missing transverse energy (inferred from momentum conservation).

After an L1 trigger tags an event, high-resolution data is read out from buffers for additional data processing before reaching the HLT. Each event of  $\sim 1.5MB$  is transferred

to front-end readout buffers which then pipes data to a processor containing the HLT code. HLT code is designed to discard events as soon as possible when making trigger decisions and only a subset of objects or partial reconstruction of events may occur before the final trigger decision is made, though HLT algorithms typically approach the quality of final reconstruction. The HLT reduces the L1 output rate to  $\mathcal{O}(100\text{Hz})$  for event storage and full reconstruction.

### 3.3 CMS Physics Objects

When physics events are fully reconstructed, detector data is used to identify *physics objects* representing real particles and event quantities for use in a physics analysis. The physics objects in an event — such as leptons, jets, or missing energy — and their properties are used to select events of interest for physics analyses targeting different final states. The properties of physics objects and global event data are also be used to make analysis level decisions of the quality of different objects. Here we describe some of the physics objects referred to in the  $M_{\text{T}2}$  analysis and how they are reconstructed, as well as some global event properties and quality variables used as discriminants for physics objects and events.

#### 3.3.1 Particle Flow

Most of the physics objects described in the following sections are reconstructed and identified in CMS using the particle flow (PF) algorithm [47]. The PF algorithm is a holistic, iterative algorithm which uses all the available data in the detector to classify "PF

"candidate" particles in an event. PF works iteratively by identifying tracks and calorimeter deposits into a PF candidate, removing all energy and hits associated with the candidate and repeating the algorithm until all the detector information has been associated to PF objects. First any muon tracks in the inner tracker associated with muon system hits are associated and removed. remaining tracks are extrapolated into the calorimeters, and any energy deposits on the path are associated with the track and removed from further consideration. Once all the tracks have been associated, the remaining energy clusters can be identified with photons and neutral hadrons (depending on their presence in the ECAL or HCAL, respectively). An example of the different tracks and energy deposits associated with various particles can be seen in figure 3.11.

### 3.3.2 Isolation

Isolation is an important distinguishing variable for physics objects measured in the detector. Simply put, isolation measures the total amount of energy in some proximity to a physics object. Because many physics processes results in particle production outside the primary interaction vertex (such as showering, decays, hadronization, pair production, etc.), the isolation of a particle parametrizes the amount of other "activity" surrounding the physics object, and consequently proves a useful discriminant when determining if particles are produced in the primary interaction, or in subsequent physics processes. Particles which are produced in the primary physics process in a collision are sometimes referred to as *prompt*, and isolation is a powerful tool in identifying prompt leptons in particular.

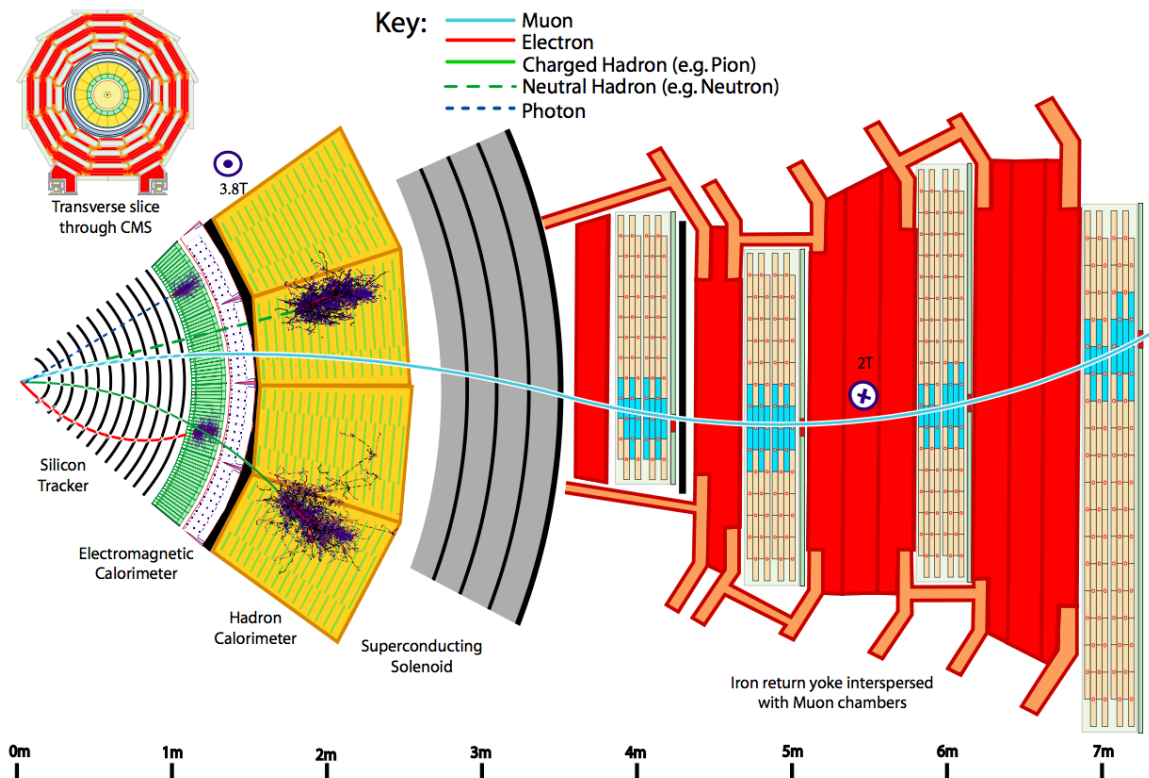


**Figure 3.11:** A graphic depiction of different particles leaving various signatures in the different CMS detector subsystems. Particles may be detected via tracks hits, energy deposits, or a combination of both.

### 3.3.3 Electrons, Muons, and Photons

The primary leptons considered in this analysis are electrons and muons (discussed in section 3.3.4), and photons are also used as a cross-check in some control regions for background estimates. Prompt electrons and photons are identified in CMS primarily through the use of the ECAL, where they are stopped and deposit all their energy [11, 31]. Prompt electrons are customarily distinguished by both the presence of a track originating at the primary vertex and a sufficiently low isolation.

Electrons in CMS are identified primarily through the existence of a charged particle track terminating in an energy cluster in the ECAL. As described in section 3.2.2, the ECAL crystals are  $\sim 25$  radiation lengths deep, and will stop and contain nearly all of the energy of an electron (except perhaps minuscule losses to scattering in the tracker). The charged track leading to the energy deposit distinguishes the charged particle from a neutral particle, and the direction of curvature of the path in the tracker can be used to identify the charge of an electron (or positron).

Photons are distinguished from electrons by the lack of a track in the SVT. As a neutral particle, the only sign of a photon will be the energy deposit in the ECAL where the photon is stopped and deposits all its energy. Photons are typically distinguished from other neutral electromagnetic particles (such as a  $\pi^0$ ) by the shape of the shower in the ecal. Whereas photons typically shower through pair production and bremsstrahlung, other hadronic particles may cascade via different physics processes leading to measurable difference in the shape of the energy cluster.

### 3.3.4 Muons

Prompt muons produced in collisions at the LHC are generally minimum ionizing particles, and will penetrate the bulk of the detector. Without any matching calorimeter deposits, they are reconstructed using hits in the muon system matched to inner tracker hits [17]. The muon system flags muon candidates, which are then matched to inner tracker hits for the best fit of the muon track. Given the track hits, the transverse momentum and energy of the muon can be calculated by a fit to the track parameters. As with electrons, muons are customarily distinguished by both the presence of a track originating at the primary vertex and a sufficiently low isolation.

### 3.3.5 Jets

Many particles produced at the LHC are created through the strong interaction, which may produce particles carrying color charge in the final state (i.e. quarks or gluons). Colored particles cannot exist individually due to the phenomenon known as *confinement*, and so via the process of *hadronization* (also referred to as *fragmentation*) they will proliferate in a series of interactions producing additional particle-antiparticle pairs, cascading in a parton shower to form hadronic bound states. When a "bare" quark or gluon is produced in the primary interaction, the ensuing hadronization results in a stream of tightly collimated hadrons aligned with the trajectory of the original bare particle, referred to as a *jet*.

Jets present themselves in CMS as collimated energy deposits in both the ECAL

and HCAL, as well as tracks originating at the primary vertex [46]. Between the two calorimeters, all the electromagnetic and hadronic components of the jet are stopped and measured by the calorimeters, and any leptons (including muons detected in the muon system) which originate in the cone of the jet are assigned to the total jet energy. The jets are reconstructed using the "anti- $k_T$ " algorithm, which clusters jet activity in cones of a fixed radius [14]. The jet is treated as a single physics object with a total energy equal to the sum of its electromagnetic, hadronic, and leptonic components, which by momentum conservation dictates the energy of the prompt quark or gluon that was produced in the primary interaction.

Furthermore, the substructure of jets and their content can be analyzed to determine the flavor of the parent parton, known as "tagging". Jets are typically tagged to distinguish between those originating from heavy-flavor quarks (bottom or charmed) and light-flavor quarks. Top quarks produced in primary interactions are unique because of their short lifetime. A top quark will decay before hadronization occurs, instead producing a  $W$  boson and down-type (down, bottom, or strange) quark which will subsequently hadronize. Searches involving top quarks in the final state typically employ "top-taggers" to search for these signatures of the top quark.

In practice, jets are complicated objects consisting of many constituent particles, and must be clustered and calibrated so that the jet energy closely matches that of the parent parton which produced the jet. Jet energy corrections (JECs) are applied to raw jet energies to compensate for different experimental deviations from the parent parton energy [37, 20]. In particular, JECs include corrections to compensate for pileup energy

as described in section 3.1.1 [13], detector effects (as a function of  $\eta$ ), energy scale as a function of jet  $p_T$ , and residual corrections to account for differences between data and simulation. The JECs are calculated by collecting data events with a Z boson (decaying to electrons or muons) or photon recoiling against a jet. By precisely measuring the bosons energy with the ECAL, scale factors are derived for jets as a function of pseudorapidity  $\eta$  and momentum  $p_T$ .

### 3.3.6 Missing Energy

Missing energy refers to the sum of all energy which has escaped the detector, and is inferred from a momentum-imbalance in the physics objects measured by the detector [18]. Because the momentum of the incident protons is zero perpendicular to the direction of the beam, the momentum of physics objects produced in any collision must sum to zero in the direction transverse to the beamline. The missing transverse energy ( $E_T^{\text{miss}}$ ), is calculated by taking the negative vector sum of all PF candidates as in equation 3.5.  $E_T^{\text{miss}}$  is of particular importance to analyses targeting BSM physics, as BSM signatures characteristically contain invisible particles in the final state which escape detection.

$$\vec{E}_T^{\text{miss}} = - \sum_i \vec{p}_T^i \quad (3.5)$$

The missing energy in an event is inferred from all other measured quantities in an event, and there are many sources of  $E_T^{\text{miss}}$  which are unphysical in nature but rather dependent on experimental effects. Particles from the primary interaction with a sufficiently large pseudorapidity may escape the fiducial region of the detector subsystems, and resolu-

tion effects or intrinsic noise in the detector may lead to fluctuations in measured energies. These experimental effects must be suppressed or distinguished from "real"  $E_T^{\text{miss}}$  due to physics processes creating particles which escape the detector (e.g. neutrinos). Analyses sensitive to final states with  $E_T^{\text{miss}}$  often employ robust data-driven methods to predict or suppress backgrounds which might generate experimental sources of  $E_T^{\text{miss}}$  or physics processes which can contribute real  $E_T^{\text{miss}}$  (such as  $Z \rightarrow \nu\bar{\nu}$ ).

### 3.3.7 Monte Carlo Simulation

Monte Carlo (MC) simulation of events within the CMS detector is frequently generated to understand the expected physics, design analyses, and help predict certain backgrounds. The simulation begins with the underlying physics process of interest, and subsequently models the trajectories of particles in the final state through the detector volume, their interactions in those volumes and with the detector material, the effects of pileup, and the detector response.

The process of generating MC proceeds in multiple steps interfacing different software packages. In this analysis, many MC samples are generated using the POWHEG [42] and MadGraph [10] generator packages to calculate the matrix elements for the underlying physics process. The calculations performed by these generators are then interfaced with Pythia [49] to model parton showering and hadronization effects. The material interaction in the detector volume are modeled with the Geant4 toolkit [8], and the detector's response is digitized to model the final readout from the event.

Because of the many computationally expensive steps involved in creating MC and

the large amount of events required to suppress statistical uncertainties, simulation is occasionally generated with the Fastsim package [7] to decrease computational burden at the expense of some modeling quality. When Fastsim is employed in this analysis for the purpose of generating signal MC, effects due to potential mismodeling introduced by the simulation are accounted for in studies of the systematic uncertainty (as shown in section 6.2.1).

This work would not have been possible without all the members of the CMS collaboration, whose support made it possible to produce the figures and tables in this chapter.

# Chapter 4

## The $M_{T2}$ Variable Search

### 4.1 Analysis Strategy

Searches for new physics targeting all-hadronic final states present unique challenges and opportunities at the LHC, and have previously been conducted by both the ATLAS collaboration [5, 2, 3, 6, 1, 36] and the CMS collaboration [33, 34, 35]. While such searches typically implement stringent vetoes on lepton candidates (and thus suppress the need to correctly identify “real” leptons), the high rate of QCD processes in proton-proton collisions generates large amounts of SM events with all-hadronic final states. Designing a search targeting signatures with all-hadronic final states requires a mechanism to distinguish and suppress the selection of multi-jet QCD events from new physics signatures, as well as robust background estimation methods to predict the yield of standard model events which may generate missing energy (such as  $Z \rightarrow \nu\bar{\nu}$ ).

The  $M_{T2}$  analysis harnesses the discriminating power of the  $M_{T2}$  variable to dis-

tinguish standard model events from possible signatures including new physics. By first requiring a significant amount of missing energy in the event, multi-jet QCD processes are greatly suppressed. Additional requirements on the topology of the event implemented using  $M_{T2}$  further suppress QCD-like processes and favor events with real missing energy anti-aligned with the hadronic energy deposits in the detector. After estimating the minimal QCD contribution remaining by extrapolating from a region orthogonal to the signal selection, the only remaining backgrounds are leptonic events where the lepton failed reconstruction or identification (or "lost-lepton" events), and SM events creating real  $E_T^{\text{miss}}$ , in the form of neutrinos from a decaying Z boson recoiling against jets (or "invisible Z" events).

## 4.2 The $M_{T2}$ Variable

$M_{T2}$  is a particularly useful kinematic mass variable for final states where two particles decay (possibly in a chain) to a final state containing an invisible particle X of mass  $m_X$  [38]. The typical transverse mass  $M_T$ , is defined in equation 4.1 for particles  $i = 1, 2$ , where the mass  $m^{\text{vis}(i)}$ , transverse momentum  $\vec{p}_t^{\text{vis}(i)}$ , and transverse energy  $E_T^{\text{vis}(i)}$  characterize the visible kinematics of the decay chain, and  $\vec{p}_t^{X(i)}$  and  $E_T^{X(i)}$  characterize the unknown kinematics of the invisible particle X.

$$(M_T^{(i)})^2 = (m^{\text{vis}(i)})^2 + m_X^2 + 2 \left( E_T^{\text{vis}(i)} \cdot E_T^{X(i)} - \vec{p}_t^{\text{vis}(i)} \cdot \vec{p}_t^{X(i)} \right) \quad (4.1)$$

In principle, if the correct values of  $m_X$  and  $\vec{p}_t^{X(i)}$  were accessible, then the transverse mass would have a kinematic endpoint and not exceed the mass of the parent particles.

However, the individual momenta of the invisible particles in the two decay chains cannot be measured; the only quantity experimentally accessible is the total missing momentum  $\vec{p}_T^{\text{miss}}$ . With this in mind, the generalized transverse mass variable  $M_{\text{T2}}$  is defined in equation 4.2, where the unknown mass  $m_X$  is a free parameter and a minimization is performed over the sum of invisible momenta  $\vec{p}_t^{X(i)}$  that satisfy the measured  $\vec{p}_T^{\text{miss}}$  constraint.

$$M_{\text{T2}}(m_X) = \min_{\vec{p}_t^{X(1)} + \vec{p}_t^{X(2)} = \vec{p}_T^{\text{miss}}} \left[ \max \left( M_T^{(1)}, M_T^{(2)} \right) \right] \quad (4.2)$$

Because this analysis selects final states with (often several) jets in the final state, the calculation of  $M_{\text{T2}}$  first requires grouping the hadronic jet activity into two large *pseudojets* to act as the visible components in the  $M_{\text{T2}}$  equation. The jet activity in each event is divided into two hemispheres, and the jets in each hemisphere are summed together to create the pseudojets. The hemisphere algorithm proceeds as follows:

- The direction of the two jets with largest invariant mass is chosen as the initial seed for the two axes.
- Jets are associated to one of the two axes according to the minimal Lund distance, such that jet  $k$  is associated to hemisphere  $i$  instead of  $j$  if the condition in equation 4.3 is true.
- After each jet is associated to one of the two axes, the axes are recalculated by summing the momenta of all jets associated to an axis.
- The association algorithm iterates using the new axes, and continues until no jets are associated to a different axis after an iteration.

$$(E_i - p_i \cos \theta_{ik}) \frac{E_i}{(E_i + E_k)^2} \leq (E_j - p_j \cos \theta_{jk}) \frac{E_j}{(E_j + E_k)^2} \quad (4.3)$$

QCD multijet events (when clustered using this pseudojet algorithm) may yield high  $M_{T2}$  events if the pseudojets have high jet masses, thus the visible masses  $m^{\text{vis}(i)}$  are set to zero to suppress such SM events. Since the kinetic components of  $M_{T2}$  will be large for signal events, this suppression does not significantly impact sensitivity to many BSM signatures, thus  $M_{T2}$  is calculated in this analysis using only  $E_T^{\text{miss}}$  and the two pseudojets.

### 4.3 Event Selection Criteria

The general strategy for the event selection is to first apply baseline cuts on motivated by hardware and software-level triggers (discussed in section 3.2.5) and reducing the QCD multi-jet background to negligible levels. Events are further categorized using the scalar sum of the transverse momenta  $p_T$  of all selected jets ( $H_T$ ), the total number of jets in the event ( $N_{\text{jets}}$ ), the total number of b-tagged jets in the event ( $N_{\text{b-jets}}$ ), and  $M_{T2}$ . A summary of the event preselections can be found in table 4.1.

### 4.4 Search Regions

The search regions are defined by categorizing events in bins of  $H_T$ ,  $N_{\text{jets}}$ ,  $N_{\text{b-jets}}$ , and  $M_{T2}$  (in addition to the baseline selection described in section 4.3). First events are categorized into "topological regions" according to  $H_T$ ,  $N_{\text{jets}}$ , and  $N_{\text{b-jets}}$ :

- $H_T$  (GeV): [250, 450] (Very Low), [450, 575] (Low), [575, 1000] (Medium), [1000, 1500]

**Table 4.1:** Summary of physics objects and preselection for events. Here  $R$  is the distance parameter of the anti- $k_T$  algorithm, and for veto leptons and tracks, the transverse mass  $M_T$  is determined using the veto object and the  $\vec{E}_T^{\text{miss}}$ , while  $p_T^{\text{sum}}$  denotes the sum of the transverse momenta of all the PF candidates in a cone around the lepton or track. The size of the cone, in units of  $\Delta R \equiv \sqrt{(\Delta\phi)^2 + (\Delta\eta)^2}$  is given in the table.

Trigger	$E_T^{\text{miss}} > 120 \text{ GeV}$ and $H_T^{\text{miss}} > 120 \text{ GeV}$ or $H_T > 300 \text{ GeV}$ and $E_T^{\text{miss}} > 110 \text{ GeV}$ or $H_T > 900 \text{ GeV}$ or jet $p_T > 450 \text{ GeV}$
Jet selection	$R = 0.4$ , $p_T > 30 \text{ GeV}$ , $ \eta  < 2.4$
b tag selection	$p_T > 20 \text{ GeV}$ , $ \eta  < 2.4$
$E_T^{\text{miss}}$	$E_T^{\text{miss}} > 250 \text{ GeV}$ for $H_T < 1000 \text{ GeV}$ , else $E_T^{\text{miss}} > 30 \text{ GeV}$ $\Delta\phi_{\text{min}} = \Delta\phi(p_T^{\text{miss}}, j_{1,2,3,4}) > 0.3$ $ \vec{E}_T^{\text{miss}} - \vec{H}_T^{\text{miss}} /E_T^{\text{miss}} < 0.5$
$M_{T2}$	$M_{T2} > 200 \text{ GeV}$ for $H_T < 1500 \text{ GeV}$ , else $M_{T2} > 400 \text{ GeV}$
Veto muon	$p_T > 10 \text{ GeV}$ , $ \eta  < 2.4$ , $p_T^{\text{sum}} < 0.2 \times p_T^{\text{lep}}$ or $p_T > 5 \text{ GeV}$ , $ \eta  < 2.4$ , $M_T < 100 \text{ GeV}$ , $p_T^{\text{sum}} < 0.2 \times p_T^{\text{lep}}$
Veto electron	$p_T > 10 \text{ GeV}$ , $ \eta  < 2.4$ , $p_T^{\text{sum}} < 0.1 \times p_T^{\text{lep}}$ or $p_T > 5 \text{ GeV}$ , $ \eta  < 2.4$ , $M_T < 100 \text{ GeV}$ , $p_T^{\text{sum}} < 0.2 \times p_T^{\text{lep}}$
Veto track	$p_T > 10 \text{ GeV}$ , $ \eta  < 2.4$ , $M_T < 100 \text{ GeV}$ , $p_T^{\text{sum}} < 0.1 \times p_T^{\text{track}}$
$p_T^{\text{sum}}$ cone	Veto e or $\mu$ : $\Delta R = \min(0.2, \max(10 \text{ GeV}/p_T^{\text{lep}}, 0.05))$ Veto track: $\Delta R = 0.3$

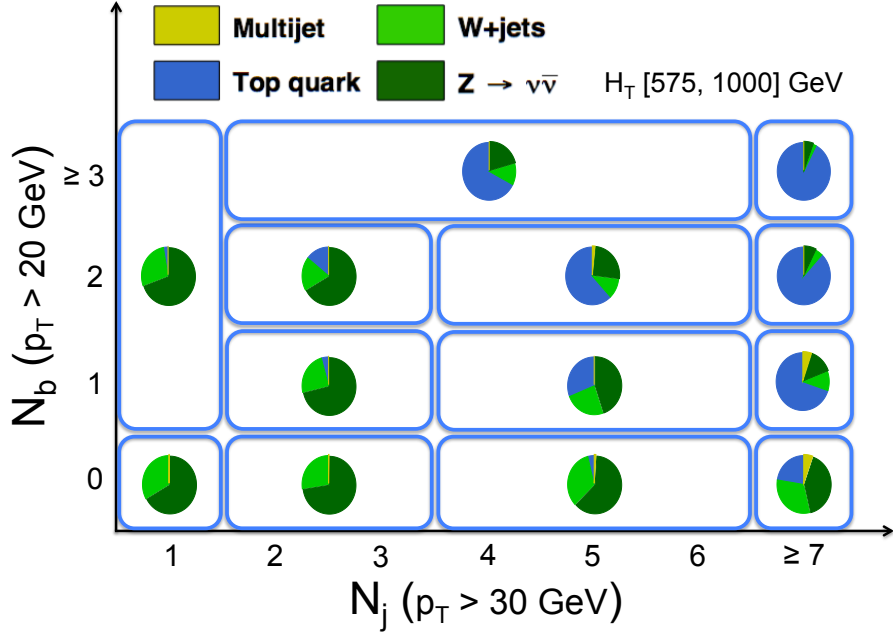


**Figure 4.1:** Topological regions in  $N_{\text{jets}}$  and  $N_{\text{b-jets}}$  for the  $[575, 1000]$   $H_T$  region. Within each region, the relative fraction of background events from different SM processes is shown based on simulation.

(High),  $[1500, \infty]$  (Extreme)

- $N_{\text{jets}} \& N_{\text{b-jets}}$ : 2-3j 0b, 2-3j 1b, 2-3j 2b, 4-6j 0b, 4-6j 1b, 4-6j 2b,  $\geq 7$ j 0b,  $\geq 7$ j 1b,  $\geq 7$ j 2b, 2-6j  $\geq 3$ b, and  $\geq 7$ j  $\geq 3$ b (except in the region with  $250 < H_T < 450$  GeV, where bins  $\geq 7$ j are merged with 4-6j bins due to lack of events).

The different topological regions for one  $H_T$  region and their background composition are depicted in figure 4.1. Each topological region is further divided into bins based on  $M_{T2}$ . The  $M_{T2}$  binning is constructed such that the low edge of the first bin is 400 GeV in regions with  $H_T > 1500$  GeV and 200 GeV everywhere else, and the low edge of the final bin is constructed to contain approximately one background event based on simulation

and not exceeding the maximum  $H_T$  value in that topological region (since an upper limit on  $H_T$  places an upper limit on  $M_{T2}$ ). The detailed  $M_{T2}$  binning is as follows:

- Very Low  $H_T$ : [200,300], [300,400], [400, $\infty$ ]
- Low  $H_T$ : [200,300], [300,400], [400,500], [500, $\infty$ ]
- Medium  $H_T$ : [200,300], [300,400], [400,600], [600,800], [800, $\infty$ ]
- High  $H_T$ : [200,400], [400,600], [600,800], [800, 1000], [1000, 1200], [1200, $\infty$ ]
- Extreme  $H_T$ : [400,600], [600,800], [800,1000], [1000,1400], [1400, $\infty$ ]

The various  $H_T$  bins and associated  $M_{T2}$  binning can be seen in figure 4.2, and the full breakdown of signal regions (including  $M_{T2}$  binning) is listed in tables 4.2 and 4.3. In addition to multi-jet search regions, this analysis also considers monojet events. Because there is only a single jet (and  $M_{T2}$  is ill-defined without multiple jets), binning in these regions is defined using  $N_{b\text{-jets}}$  and  $H_T$  as follows:

- $N_{b\text{-jets}}$ : 0b,  $\geq 1$ b
- $H_T$ : [250,350], [350,450], [450,575], [575,700], [700,1000], [1000,1200], [1200, $\infty$ ]

As with the multi-jet regions, monojet  $H_T$  bins with less than one simulated background event in the final bin are merged with the penultimate bin.

In addition to these signal regions used to interpret results in the context of various BSM physics models, the analysis also provides results in "super signal regions" (SSRs) as defined in table 4.4. These regions provide a simpler set of selection than the nominal

**Table 4.2:**  $M_{T2}$  binning in the Very Low, Low, and Medium  $H_T$  topological regions.

$H_T$ Range [GeV]	Jet Multiplicities	Binning [GeV]
[ 250, 450 ]	2 – 3j, 0b	[ 200, 300, 400, $\infty$ ]
	2 – 3j, 1b	[ 200, 300, 400, $\infty$ ]
	2 – 3j, 2b	[ 200, 300, 400, $\infty$ ]
	$\geq 4j$ , 0b	[ 200, 300, 400, $\infty$ ]
	$\geq 4j$ , 1b	[ 200, 300, 400, $\infty$ ]
	$\geq 4j$ , 2b	[ 200, 300, 400, $\infty$ ]
	$\geq 2j, \geq 3b$	[ 200, 300, 400, $\infty$ ]
[ 450, 575 ]	2 – 3j, 0b	[ 200, 300, 400, 500, $\infty$ ]
	2 – 3j, 1b	[ 200, 300, 400, 500, $\infty$ ]
	2 – 3j, 2b	[ 200, 300, 400, 500, $\infty$ ]
	4 – 6j, 0b	[ 200, 300, 400, 500, $\infty$ ]
	4 – 6j, 1b	[ 200, 300, 400, 500, $\infty$ ]
	4 – 6j, 2b	[ 200, 300, 400, 500, $\infty$ ]
	$\geq 7j$ , 0b	[ 200, 300, 400, $\infty$ ]
	$\geq 7j$ , 1b	[ 200, 300, 400, $\infty$ ]
	$\geq 7j$ , 2b	[ 200, 300, 400, $\infty$ ]
	2 – 6j, $\geq 3b$	[ 200, 300, 400, 500, $\infty$ ]
[ 575, 1000 ]	$\geq 7j, \geq 3b$	[ 200, 300, 400, $\infty$ ]
	2 – 3j, 0b	[ 200, 300, 400, 600, 800, $\infty$ ]
	2 – 3j, 1b	[ 200, 300, 400, 600, 800, $\infty$ ]
	2 – 3j, 2b	[ 200, 300, 400, 600, 800, $\infty$ ]
	4 – 6j, 0b	[ 200, 300, 400, 600, 800, $\infty$ ]
	4 – 6j, 1b	[ 200, 300, 400, 600, 800, $\infty$ ]
	4 – 6j, 2b	[ 200, 300, 400, 600, 800, $\infty$ ]
	$\geq 7j$ , 0b	[ 200, 300, 400, 600, 800, $\infty$ ]
	$\geq 7j$ , 1b	[ 200, 300, 400, 600, $\infty$ ]
	$\geq 7j$ , 2b	[ 200, 300, 400, 600, $\infty$ ]
	2 – 6j, $\geq 3b$	[ 200, 300, 400, 600, $\infty$ ]
	$\geq 7j, \geq 3b$	[ 200, 300, 400, 600, $\infty$ ]

**Table 4.3:**  $M_{T2}$  binning in the High and Extreme  $H_T$  topological regions.

$H_T$ Range [GeV]	Jet Multiplicities	Binning [GeV]
[ 1000, 1500 ]	2 – 3j, 0b	[ 200, 400, 600, 800, 1000, 1200, $\infty$ ]
	2 – 3j, 1b	[ 200, 400, 600, 800, 1000, 1200, $\infty$ ]
	2 – 3j, 2b	[ 200, 400, 600, 800, 1000, $\infty$ ]
	4 – 6j, 0b	[ 200, 400, 600, 800, 1000, 1200, $\infty$ ]
	4 – 6j, 1b	[ 200, 400, 600, 800, 1000, 1200, $\infty$ ]
	4 – 6j, 2b	[ 200, 400, 600, 800, 1000, $\infty$ ]
	$\geq 7j$ , 0b	[ 200, 400, 600, 800, 1000, $\infty$ ]
	$\geq 7j$ , 1b	[ 200, 400, 600, 800, $\infty$ ]
	$\geq 7j$ , 2b	[ 200, 400, 600, 800, $\infty$ ]
	2 – 6j, $\geq 3b$	[ 200, 400, 600, $\infty$ ]
	$\geq 7j$ , $\geq 3b$	[ 200, 400, 600, $\infty$ ]
[ 1500, $\infty$ ]	2 – 3j, 0b	[ 400, 600, 800, 1000, 1400, $\infty$ ]
	2 – 3j, 1b	[ 400, 600, 800, 1000, $\infty$ ]
	2 – 3j, 2b	[ 400, $\infty$ ]
	4 – 6j, 0b	[ 400, 600, 800, 1000, 1400, $\infty$ ]
	4 – 6j, 1b	[ 400, 600, 800, 1000, 1400, $\infty$ ]
	4 – 6j, 2b	[ 400, 600, 800, $\infty$ ]
	$\geq 7j$ , 0b	[ 400, 600, 800, 1000, $\infty$ ]
	$\geq 7j$ , 1b	[ 400, 600, 800, $\infty$ ]
	$\geq 7j$ , 2b	[ 400, 600, 800, $\infty$ ]
	2 – 6j, $\geq 3b$	[ 400, 600, $\infty$ ]
	$\geq 7j$ , $\geq 3b$	[ 400, $\infty$ ]

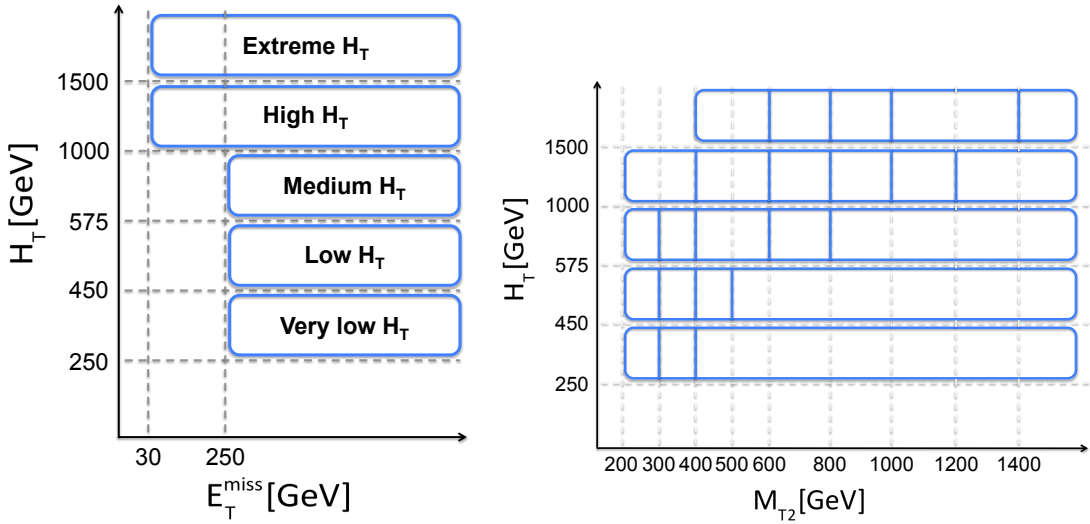


**Figure 4.2:** Signal region bins in  $H_T$  and  $E_T^{\text{miss}}$  (left) and  $M_{T2}$  binning within each  $H_T$  region (right). If simulation predicts less than one background event in the greatest  $M_{T2}$  bin within a region, it is merged with the previous bin.

signal regions so that phenomenologists may easily reinterpret results in the context of different signal models. Results obtained using the SSRs are not as sensitive as the nominal binning — finely binned regions have a higher signal-to-background ratio and the global background fit reduces the background uncertainties – but are much easier to use for reinterpretation than the many correlated bins of the nominal analysis.

## 4.5 Control Regions

In order to anchor the data-driven background estimates used in this analysis, *control regions* (CR) orthogonal to the signal region selection are defined for various processes. In particular, there are control regions corresponding to enriched samples of  $\gamma + \text{jet}$  events,

**Table 4.4:** Definition of "super signal regions" used in reinterpretations of the analysis.

Region	$N_{\text{jets}}$	$N_{\text{b-jets}}$	$H_T$ [GeV]	$M_{T2}$ [GeV]
2j loose	$\geq 2$	-	$> 1000$	$> 1200$
2j tight	$\geq 2$	-	$> 1500$	$> 1400$
4j loose	$\geq 4$	-	$> 1000$	$> 1000$
4j tight	$\geq 4$	-	$> 1500$	$> 1400$
7j loose	$\geq 7$	-	$> 1000$	$> 600$
7j tight	$\geq 7$	-	$> 1500$	$> 800$
2b loose	$\geq 2$	$\geq 2$	$> 1000$	$> 600$
2b tight	$\geq 2$	$\geq 2$	$> 1500$	$> 600$
3b loose	$\geq 2$	$\geq 3$	$> 1000$	$> 400$
3b tight	$\geq 2$	$\geq 3$	$> 1500$	$> 400$
7j3b loose	$\geq 7$	$\geq 3$	$> 1000$	$> 400$
7j3b tight	$\geq 7$	$\geq 3$	$> 1500$	$> 400$

single lepton events,  $Z \rightarrow l^+l^-$  events, and QCD multijet events.

#### 4.5.1 Single Lepton Control Region

The single lepton CR is constructed to select a sample enriched with single lepton events, the most dominant contributions being from  $t\bar{t}$  and  $W + \text{jets}$  production. The same baseline selections described in section 4.3 are applied with the exception of the following:

- In lieu of the lepton veto, exactly one lepton candidate passing the reco or PF lepton selections is required. In order to avoid double counting (for leptons which are reconstructed both as a reco lepton and PF candidate), PF leptons within  $\Delta R < 0.1$  of a reco lepton are not considered.
- The transverse mass  $M_{T2}$  between the lepton and  $E_T^{\text{miss}}$  must be less than 100 GeV to reduce possible signal contamination.

Since non-isolated leptons in the fiducial region of the detector are usually successfully reconstructed, the closest jet within  $\Delta R < 0.4$  of the lepton is removed and the lepton instead counted as a visible object for the purposes of computing  $H_T$ ,  $H_T^{\text{miss}}$ ,  $\Delta\phi(j_{1234}, E_T^{\text{miss}})$ ,  $|\vec{H}_T^{\text{miss}} - \vec{E}_T^{\text{miss}}|/E_T^{\text{miss}}$ , and  $M_{T2}$  (as well as the hemispheres used to calculate  $M_{T2}$ ). Events are further subdivided into the topological regions described in section 4.4 using the modified  $H_T$  and  $N_{\text{jets}}$  and  $N_{\text{b-jets}}$ , but not in  $M_{T2}$  to increase the statistical power of the CR. The signal regions with  $\geq 7j, \geq 1b$  are all predicted using CRs with identical  $H_T$  bins but  $\geq 7j, 1\text{-}2b$  to increase the statistical power of those CRs (and to avoid signal contamination in regions with  $\geq 7j, \geq 3b$ ). In addition, for regions with  $H_T > 1500$  GeV, the minimum

$M_{\text{T2}}$  threshold is set to 200 GeV to increase available statistics. The monojet CR is binned identically to the signal region.

#### 4.5.2 Dilepton Control Region

Control regions corresponding to opposite-sign same-flavor leptons (OSSF) from  $Z \rightarrow l^+l^-$  events are used to estimate the  $Z \rightarrow \nu\bar{\nu}$  background, with corresponding sets of control regions requiring an opposite-sign opposite-flavor (OSOF) pair to estimate the flavor-symmetric background component in the former dilepton CR. The same baseline selections as described in section 4.3 are applied with the exception of the follow:

- In lieu of the lepton veto, exactly 2 leptons ( $ee$ ,  $e\mu$ , or  $\mu\mu$ ) passing loose lepton selections are required.
- There is no requirement on  $E_{\text{T}}^{\text{miss}}$ . Instead, the dilepton system must have a transverse momentum  $p_{\text{T}}(\ell\ell) > 200 \text{ GeV}$  to mimic the kinematics of the  $Z \rightarrow \nu\bar{\nu}$  background and suppress the  $t\bar{t}$  contribution.
- Without a missing energy requirement, events are selected in data using leptonic trigger paths. Dimuon events are selected using a combination of dimuon and high- $p_{\text{T}}$  single muon triggers, dielectron events using a combination of dielectron and high- $p_{\text{T}}$  single photon paths (which do not require isolation and recover efficiency for high- $p_{\text{T}}$  electrons or those highly co-linear high- $p_{\text{T}}$  Z bosons), and opposite-flavor events are selected using a combination of  $e\mu$  triggers and higher threshold single-lepton paths (to again recover efficiency for some events).

- To improve trigger efficiency for these regions, the leading lepton is required to have a minimum momentum  $p_T > 100 \text{ GeV}$  and the sub-leading lepton  $p_T > 30 \text{ GeV}$ .
- When selecting  $Z$  boson candidates for the  $Z \rightarrow \nu\bar{\nu}$  estimate, the leptons are also required to be OSSF with an invariant mass  $|m_{\ell\ell} - m_Z| < 20 \text{ GeV}$ , where  $m_Z$  is the nominal  $Z$  boson mass.

Similar to the single lepton control region, the closest jet within  $\Delta R < 0.4$  of each lepton is removed and the leptons added to the  $E_T^{\text{miss}}$  vector for the purposes of computing  $N_{\text{jets}}$ ,  $N_{\text{b-jets}}$ ,  $H_T$ ,  $H_T^{\text{miss}}$ ,  $\Delta\phi(j_{1234}, E_T^{\text{miss}})$ ,  $|\vec{H}_T^{\text{miss}} - \vec{E}_T^{\text{miss}}|/E_T^{\text{miss}}$ , and  $M_{\text{T2}}$  (as well as the hemispheres used to calculate  $M_{\text{T2}}$ ). Additional information on the  $M_{\text{T2}}$  binning for these regions is detailed in section 5.4.

### 4.5.3 Multijet Control Region

The multijet control region is designed to select a sample enriched in QCD events to estimate the multijet background. The same baseline selections described in section 4.3 are applied with the exception of the  $\Delta\phi(j_{1234}, E_T^{\text{miss}})$  requirement, which is inverted to select a sample dominated by QCD events with large fake  $E_T^{\text{miss}}$  due to jet energy mismeasurements.

The transfer factor which is used to extrapolate the control region yield to the signal region is measured in a separate QCD-dominated region with  $M_{\text{T2}} < 200 \text{ GeV}$ , described in detail in section 5.2. Because of the lower  $E_T^{\text{miss}}$  requirement, different trigger paths must be used. for regions with  $H_T > 1000 \text{ GeV}$  trigger paths seeded by a single high- $p_T$

jet are used. For other  $H_T$  regions, similar trigger paths with lower jet  $p_T$  thresholds are used, but due to the rate of QCD events creating low- $p_T$  jets these paths are prescaled to suppress the data acquisition rate.

This work would not have been possible without all the members of the CMS collaboration, whose support made it possible to produce the figures and tables in this chapter.

# Chapter 5

## Background Estimates

### 5.1 Types of Backgrounds

The  $M_{T2}$  all-hadronic search is primarily a search for missing energy, and the backgrounds present in the signal region can be roughly categorized into two groups: events with “fake” missing energy due to mismeasurement of energies or other experimental effects, and those with “real” missing energy due to the underlying physics process which escapes the detector. In this analysis, the primary backgrounds from SM processes with  $E_T^{\text{miss}}$  and hadronic activity in the final state can be divided into three categories:

- *Multijet events*, with no true missing energy generating fake  $E_T^{\text{miss}}$ . Such all-hadronic events usually enter analysis signal regions due to mismeasurement of jet energy or sporadic noise.

- *Lost lepton events*, with a lepton in the final state that is either not identified, reconstructed, in the fiducial region of the detector, or sufficiently isolated to pass the lepton selections. The bulk of these events are due to leptonic W boson or top quark decays (which may also produce significant real  $E_T^{\text{miss}}$  with an associated neutrino) recoiling against jets.
- *Invisible Z events*, where a Z boson produced in association with jets decays into neutrinos. The neutrinos are extremely weakly interacting particles which escape the detector without leaving any signature, and so this background is fundamentally very similar to many of the BSM signals which may appear in each search region. It is a dominant background in many signal regions, though the relative fraction decreases in regions with more b-tagged jets ( $N_{\text{b-jets}}$ ).

In order to provide a robust prediction of each background that is not heavily dependent on simulation alone, each background is estimated using data-driven techniques as described in the following sections. The control regions for each background can be found in chapter 4.

## 5.2 Multijet Estimate

The estimate of the SM multijet background utilizes two different techniques depending on the number of jets in a given signal region. For regions with two or more jets, the background is estimated by extrapolating to regions with high  $\Delta\phi_{\min}$  after inverting the  $\Delta\phi_{\min}$  requirement. In the monojet signal regions, a sample enriched in unbalanced

dijet events is used to extrapolate to regions with low sub-leading jet momentum.

### 5.2.1 Multijet Signal Region Prediction

As outlined in section 4.5.3, the multijet background in control regions with two or more jets is estimated using a QCD-enriched sample where  $H_T$  triggers are used to select events with an inverted  $\Delta\phi_{\min}$  cut. The ratio of events with high to low  $\Delta\phi_{\min}$  ( $r_\phi$ ) is modeled as a power law function in  $M_{T2}$ , as shown in equation 5.1.

$$r_\phi(M_{T2}) = \frac{N(\Delta\phi_{\min} > 0.3)}{N(\Delta\phi_{\min} < 0.3)} = a \cdot M_{T2}^b \quad (5.1)$$

The power-law dependence of  $r_\phi$  on  $M_{T2}$  is verified in simulation for events with  $M_{T2} > 60 \text{ GeV}$ , as illustrated in figure 5.1. Because the dominant source of  $E_T^{\text{miss}}$  in low  $M_{T2}$  events is not necessarily due to jet mismeasurement, the fit is performed in the window  $60 < M_{T2} < 100 \text{ GeV}$  except in extreme  $H_T$  regions where a lower bound of  $70 \text{ GeV}$  is used (as a conservative measure since these regions have high statistics). The upper bound of  $100 \text{ GeV}$  is chosen such that the contamination of electroweak and top-quark events is small compared to the QCD multijet yield. A systematic uncertainty in the  $r_\phi$  value is assigned based on variations of the fit window, by shifting the lower boundary of the window in either direction while preserving the fit statistics by shifting the upper boundary of the window. The systematic uncertainty is then taken as the maximal deviation of all such variation with respect to the nominal window.

Due to the total integrated luminosity available and the deliberate suppression rate with which some  $H_T$  triggers save events (known as the trigger *prescale*), the statistics

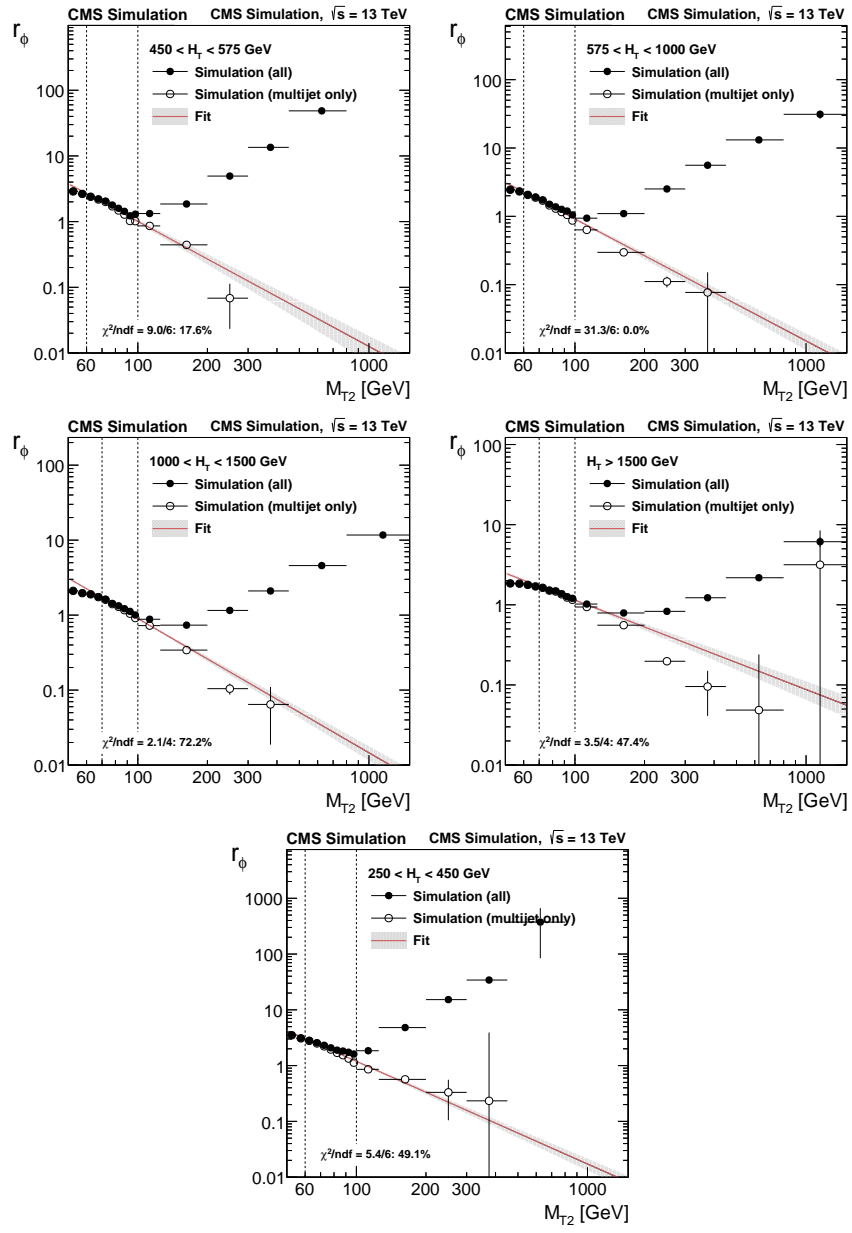


**Figure 5.1:** Simulated distribution of the  $r_\phi$  ratio as a function of  $M_{T2}$  for the low (top left), medium (top right), high (medium left), extreme (medium right), and very low (bottom)  $H_T$  regions. Solid points represent the total simulated background, and hollow points show the QCD multijet contribution only. The red line and grey error band illustrates the best fit to a power law function performed in the dashed line fit window

**Table 5.1:** Relative uncertainty of  $f_j$  and  $r_b$  associated with the assumed invariance with respect to  $M_{T2}$  and  $\Delta\phi$  (and  $H_T$  for  $r_b$  ).

Observable	$f_{23}$	$f_{46}$	$f_{7+}$	$r_0$	$r_1$	$r_2$	$r_{3+}$
Syst. Error	25%	7%	20%	8%	20%	35%	70%

are sufficient to perform fits in  $H_T$  regions inclusive in  $N_{\text{jets}}$  and  $N_{\text{jets}}$ . The inclusive multijet background estimate can be determined using  $r_\phi$  as a function of  $M_{T2}$   $N_{\text{inc}}^{SR} = r_\phi(M_{T2}) \cdot N_{\text{inc}}^{CR}(M_{T2})$ . The final estimate in a given  $N_{\text{jets}}\text{-}N_{\text{b-jets}}$  bin can be determined as in equation 5.2, where  $f_j$  is the fraction of multijet events in bin  $N_{\text{jets}}$  in a given  $H_T$  bin, and  $r_b$  is the ratio of events with  $N_{\text{b-jets}}$  b-tags in a given  $N_{\text{jets}}$  bin.

$$N_{j,b}^{SR}(M_{T2}) = r_\phi(M_{T2}) \cdot N_{\text{inc}}^{CR}(M_{T2}) \cdot f_j(H_T) \cdot r_b(N_{\text{jets}}) \quad (5.2)$$

The values of  $f_j$  and  $r_b$  are measured in data using QCD-enriched regions with an inverted  $\Delta\phi$  requirement and  $100 < M_{T2} < 200$ . Based on simulation,  $f_j$  and  $r_b$  do not significantly depend on  $M_{T2}$ , and  $r_b$  is independent of  $H_T$ . Since  $f_j$  is dependent on  $H_T$  and  $r_b$  on  $N_{\text{jets}}$ , different values of  $f_j$  are measured in each inclusive  $H_T$  region, and different values of  $r_b$  are measured in inclusive  $N_{\text{jets}}$  regions. Figures 5.2 and 5.3 illustrates the data-driven values of  $f_j$  and  $r_b$  respectively, along with a comparison to simulation. The robustness of invariance with respect to  $M_{T2}$  and  $\Delta\phi$  (and  $H_T$  for  $r_b$  ) is calculated by making several variations of the aforementioned variables and measuring consequent variations in  $f_j$  and  $r_b$ , and is summarized in table 5.1.

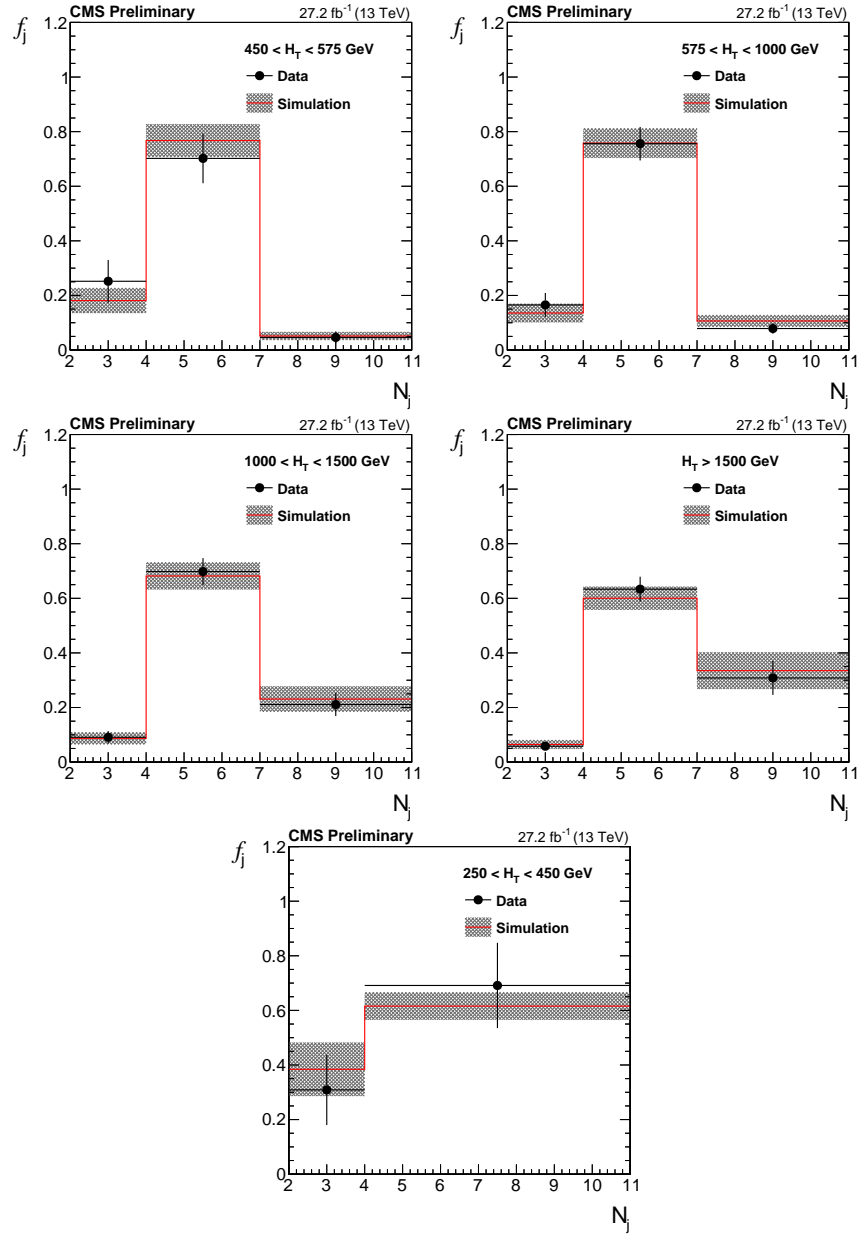


**Figure 5.2:** The values of  $f_j$  as measured in data in different  $H_T$  regions, compared to simulation. The uncertainties include both the statistical error and the systematic sources as listed in table 5.1

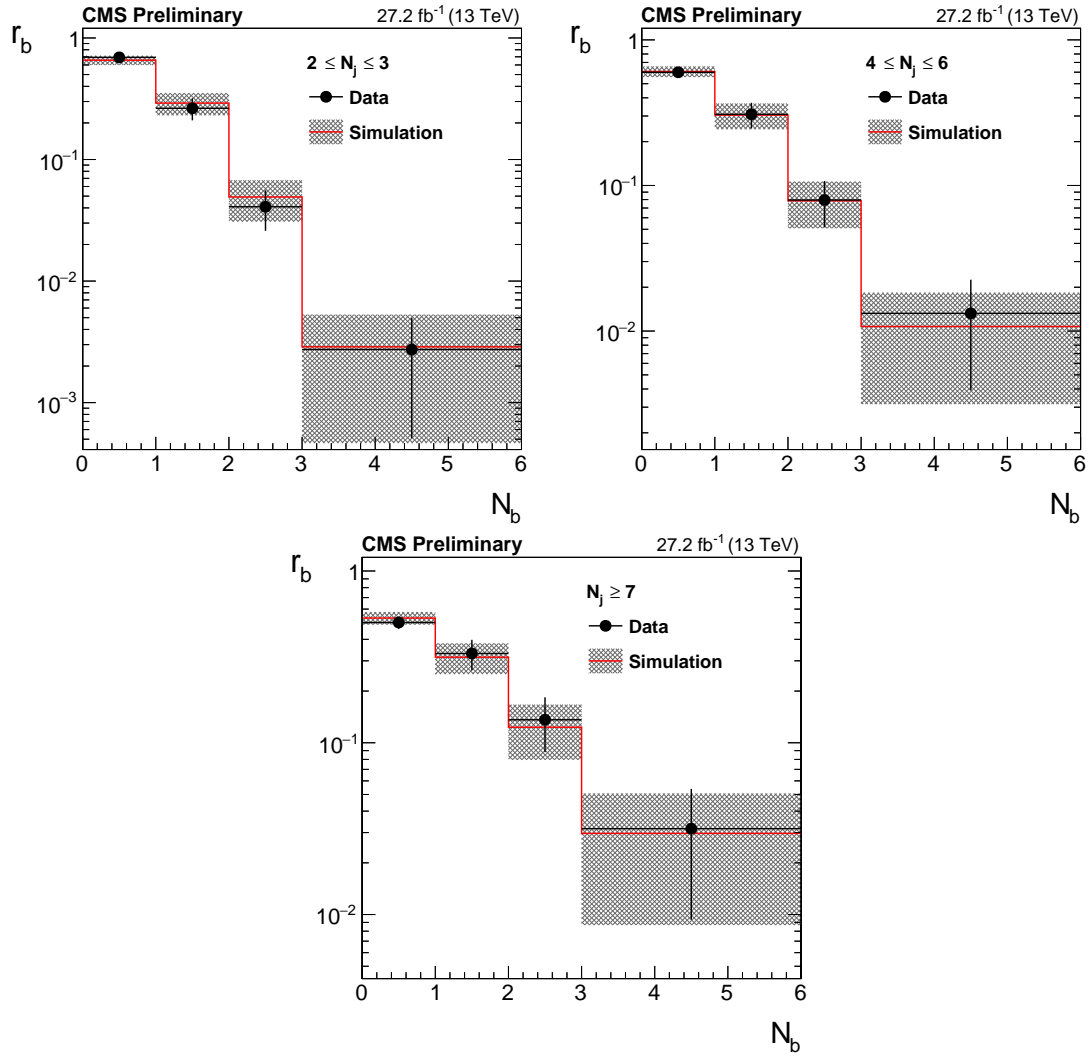


**Figure 5.3:** The values of  $r_b$  as measured in data in different  $N_{\text{jets}}$  regions, compared to simulation. The uncertainties include both the statistical error and the systematic sources as listed in table 5.1

### 5.2.2 Monojet Signal Region Prediction

The multijet background in control regions with a single jet cannot be estimated using the  $\Delta\phi$  technique since  $E_T^{\text{miss}}$  is usually very similar to the  $H_T$  in these events and typically anti-aligned with the jet. As outlined in section 4.5.3, a separate control region is devised which instead selects dijet events that are orthogonal to the multijet signal regions because of an inverted  $\Delta\phi(j_{1234}, E_T^{\text{miss}})$  cut (and orthogonal to the the monojet SR with the presence of multiple jets).

The sub-leading jet momentum for in this CR can be seen in figure 5.4. Because jets with  $p_T$  below 30 GeV are not considered, monojet events can be classified as those with  $p_T^{\text{jet}2} < 30 \text{ GeV}$ , and the CR is used to extrapolate into the regime where  $p_T^{\text{jet}2}$  is small. With decreasing  $p_T^{\text{jet}2}$ , events appear more imbalanced and approximate the topology of a true monojet event, as depicted in figure 5.5.

The predicted yield of multijet background in a monojet  $p_T^{\text{jet}1}$  bin is determined according to equation 5.3, where  $f_{\text{QCD}}$  is the fraction of QCD events as measured in the region with  $30 < p_T^{\text{jet}2} < 60 \text{ GeV}$  and  $N_{\text{data}}$  is the yield in data of dijet events with  $30 < p_T^{\text{jet}2} < 60 \text{ GeV}$ . Assuming  $N_{\text{data}}(0 - 30) < N_{\text{data}}(30 - 60)$ , this estimate provides an upper bound on the total multijet background contribution in each monojet CR. A systematic uncertainty of 50% on the QCD fraction  $f_{\text{QCD}}$  is assigned as a conservative estimate.

$$N_{\text{QCD}}(p_T^{\text{jet}1}) = N_{\text{data}}(30 - 60, p_T^{\text{jet}1}) \cdot f_{\text{QCD}}(30 - 60, p_T^{\text{jet}1}) \quad (5.3)$$

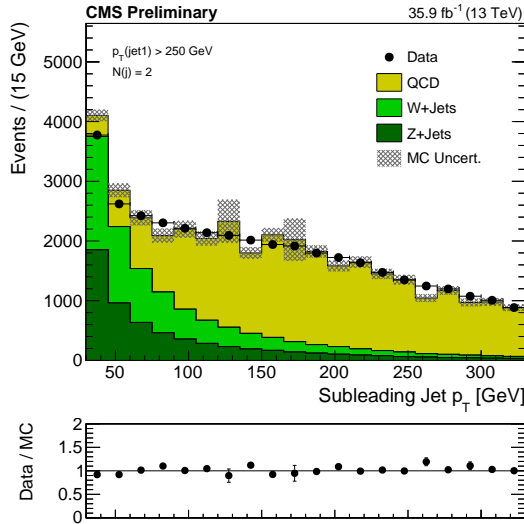


**Figure 5.4:** The transverse momentum of the sub-leading jet for dijet events in the monojet QCD background control region. The total yield of the simulation is normalized to the overall yield in data.

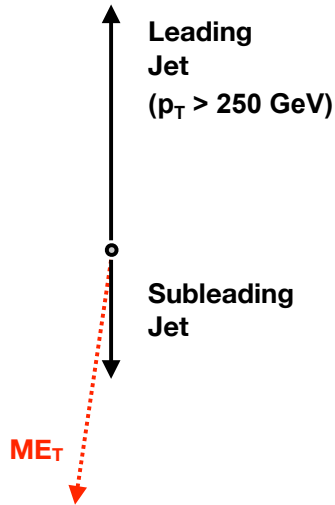


**Figure 5.5:** An illustration of “unbalanced” dijet events. As the momentum of the sub-leading jet decreases,  $E_T^{\text{miss}}$  is more anti-aligned with the primary jet and approaches the topology of a monojet event.

## 5.3 Lost Lepton Estimate

The lost lepton background is predicted by taking the yield of single lepton events in similar kinematic regions, measuring the ratio of events where the lepton is lost to those where it is found, and extrapolating into the lost lepton regime. The control region for the lost lepton estimate is described in detail in section 4.5.1, and is comprised of events in data with the same signal triggers and preselection, with the exception of an inverted lepton veto and an additional requirement on lepton  $M_T$  (to reduce signal contamination).

### 5.3.1 Background Prediction

The estimate in a given signal region is obtained from a control region using transfer factors as described in equation 5.4, where  $N_{1L}^{CR}$  is the number of events in the corresponding CR,  $R_{MC}^{0l/1l}$  is the ratio of zero-lepton to one-lepton events derived from simulation, and  $k(M_{T2})$  is the transfer factor into bins of  $M_{T2}$  in a given topological region. The ratio  $R_{MC}^{0l/1l}$  is measured in Monte Carlo after normalizing the yield to data in each CR and correcting for differences in lepton efficiency between data and simulation, and also factors in lepton acceptance, efficiency of reconstruction and identification, as well as contributions from  $W$  bosons decaying through  $\tau$  leptons to a hadronic final state. The  $M_{T2}$  transfer factor  $k(M_{T2})$  is taken from data where statistics permit, and uses information from simulation to project events into bins of  $M_{T2}$  in the low-statistics regime.

$$N_{LL}^{SR}(H_T, N_j, N_b, M_{T2}) = N_{1L}^{CR}(H_T, N_j, N_b, M_{T2}) \cdot R_{MC}^{0l/1l}(H_T, N_j, N_b, M_{T2}) \cdot k(M_{T2}) \quad (5.4)$$

To reduce the dependence of the estimate on the  $M_{T2}$  shape modeling in simulation,

the transfer factor  $k(M_{T2})$  uses a combination of data and simulation information. In each topological region, the greatest  $M_{T2}$  bin is iteratively combined with the next-greatest bin until the total expected SM background yield in simulation is at least 50 events. These combined bins together form the CR for a range of  $M_{T2}$  values, where the fraction of events falling in a particular  $M_{T2}$  bin,  $k(M_{T2})$ , is determined from simulation. In all the other  $M_{T2}$  bins in the topological region, statistics are sufficient for a direct measurement in data and  $k(M_{T2}) = 1$ . The extrapolation point for each topological region can be found in table 5.2. The shape modeling in simulation is verified in data by selecting an inclusive sample enriched in either W boson or  $t\bar{t}$  production (using the number of b-tags in the event), and predicting the  $M_{T2}$  distribution using simulation after normalizing simulation yield to data and summing all the control regions together, as seen in figure 5.6.

### 5.3.2 Systematic Uncertainties

Several sources of uncertainty are assessed for the lost lepton estimate, including those associated with the topological transfer factor and the  $M_{T2}$  shape modeling in simulation. The full list of systematic uncertainties is as follows:

- *Control region statistical error:* the Poisson error on the number of observed events in data is taken as a correlated uncertainty in each signal region using the same control region. The error is uncorrelated amongst  $M_{T2}$  bins, except in regions sharing merged  $M_{T2}$  bins for the estimate.

**Table 5.2:** The last  $M_{T2}$  bin and the  $M_{T2}$  extrapolation point for each topological region, beyond which shape data from simulation is used to extrapolate the lost lepton estimate into  $M_{T2}$  bins.

Control Region $H_T$ [GeV]	$N_j$	$N_b$	Extrapolation Point $M_{T2}$ [GeV]	Last $M_{T2}$ bin $M_{T2}$ [GeV]
[250, 450]	2-3	0	> 300	> 400
[250, 450]	2-3	1	> 300	> 400
[250, 450]	2-3	2	> 300	> 400
[250, 450]	4+	0	> 300	> 400
[250, 450]	4+	1	> 300	> 400
[250, 450]	4+	2	> 200	> 400
[250, 450]	2-3	3+	> 200	> 400
[450, 575]	2-3	0	> 400	> 500
[450, 575]	2-3	1	> 300	> 500
[450, 575]	2-3	2	> 200	> 500
[450, 575]	4-6	0	> 400	> 500
[450, 575]	4-6	1	> 300	> 500
[450, 575]	4-6	2	> 300	> 500
[450, 575]	7+	0	> 200	> 400
[450, 575]	7+	1-2	> 200	> 400
[450, 575]	2-6	3+	> 200	> 500
[575, 1000]	2-3	0	> 600	> 800
[575, 1000]	2-3	1	> 400	> 800
[575, 1000]	2-3	2	> 200	> 800
[575, 1000]	4-6	0	> 400	> 800
[575, 1000]	4-6	1	> 400	> 800
[575, 1000]	4-6	2	> 400	> 800
[575, 1000]	7+	0	> 300	> 800
[575, 1000]	7+	1-2	> 300	> 600
[575, 1000]	2-6	3+	> 200	> 600
[1000, 1500]	2-3	0	> 400	> 1200
[1000, 1500]	2-3	1	> 200	> 1200
[1000, 1500]	2-3	2	> 200	> 1000
[1000, 1500]	4-6	0	> 400	> 1200
[1000, 1500]	4-6	1	> 400	> 1200
[1000, 1500]	4-6	2	> 200	> 1000
[1000, 1500]	7+	0	> 200	> 1000
[1000, 1500]	7+	1-2	> 200	> 800
[1000, 1500]	2-6	3+	> 200	> 600
[1500, $\infty$ ]	2-3	0	> 200	> 1400
[1500, $\infty$ ]	2-3	1	> 200	> 1000
[1500, $\infty$ ]	2-3	2	> 200	> 400
[1500, $\infty$ ]	4-6	0	> 400	> 1400
[1500, $\infty$ ]	4-6	1	> 200	> 1400
[1500, $\infty$ ]	4-6	2	> 200	> 800
[1500, $\infty$ ]	7+	0	> 200	> 1000
[1500, $\infty$ ]	7+	1-2	> 200	> 800
[1500, $\infty$ ]	2-6	3+	> 200	> 600

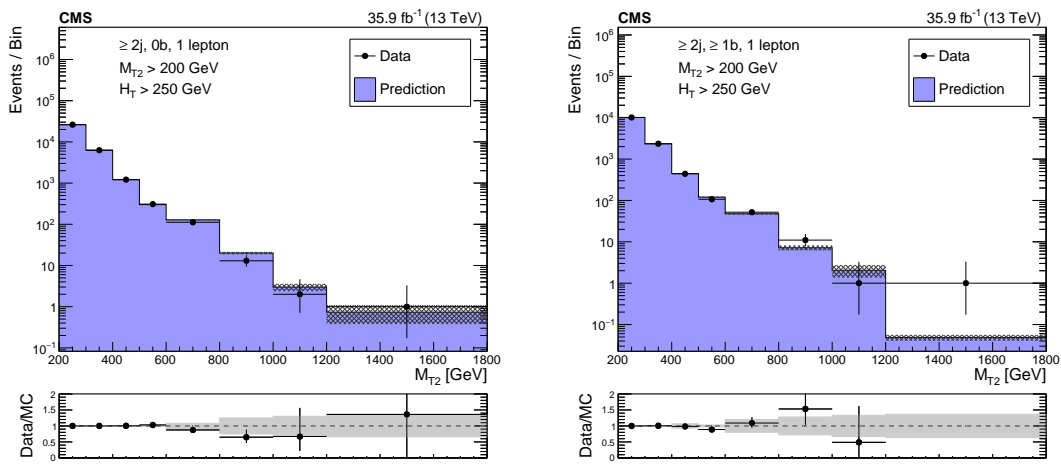


**Figure 5.6:** The  $M_{T2}$  shape in data and simulation using the single lepton CR selection, for events with zero b-tagged jets (left) or at least one b-tagged jet (right). The simulation is normalized to data in each topological region before summing to create the inclusive region. The hatched bands in each upper plot show the MC statistical uncertainty, while the shaded bands in each lower plot represent the systematic shape uncertainty.

- *Monte Carlo statistical error*: where the simulation is used to compute the transfer factor (and in some cases, the  $M_{T2}$  shape), the MC statistical uncertainty ranges from 1-50%, taken as uncorrelated amongst all bins.
- *Electron and muon selection efficiency*: the reconstruction and identification efficiency of electrons and muons is computed using a procedure known as *tag and probe*, where leptons from  $Z \rightarrow \ell\ell$  decays are used to evaluate the lepton id efficiencies as a function of lepton  $p_T$  and  $\eta$  and lepton isolation efficiencies as a function of  $p_T$  and nearby activity. The scale factors applied to simulation to compensate for such effects approach unity with uncertainties on the order of a few percent, and are correlated across all bins. The maximum effect of this uncertainty is up to 7% in some signal regions.
- *Tau selection efficiency*: the efficiency for hadronically decaying taus is classified according to the number of charged particles in the  $\tau$  decay, whether a *1-prong* tau leaving a single charged track, or a *3-prong* tau leaving three charged tracks in the final state. This efficiency is measured in simulation by measuring the isolation efficiency as a function of candidate  $p_T$  for electrons, muons, and taus in various decay modes. Based on half the difference in efficiency between 1-prong taus and muons, an uncertainty of 10% is taken for 1-prong taus which also covers and differences in veto efficiency as a function of the primary kinematic variables. For 3-prong taus, the PF hadron veto is very inefficient since most fail the isolation requirement (the typical selection efficiency is 8%), and a 100% relative uncertainty is taken to cover any

differences as a function of kinematics. These uncertainties are correlated amongst all bins.

- *$M_T$  cut efficiency:* the use of simulation to compute the CR-to-SR transfer factor also relies on the satisfactory modeling of the  $M_T$  cut in Monte Carlo. A sample of  $Z \rightarrow \ell\ell$  events is selected in data with one of the leptons “deleted” from the event to mimic a leptonic W boson decay, and compared with simulation. Based on data-MC agreement, a correlated error of 3% is taken across all bins.
- *b-tagging efficiency:* the effect of varying the b-tag scale factor efficiency is calculated in each bin, and taken as a correlated error amongst all bins. The maximum effect of this variation is about 4% in some bins.
- *Jet energy corrections:* by varying the jet energy scales across all bins, a maximum deviation of about 5% is observed in regions with sufficient statistics, and a correlated error of 5% is taken across all bins.
- *MC renormalization and factorization scales:* the overall effect of varying the simulation renormalization and factorization scales of the underlying physics processes (and subsequent effect on event kinematics) is computed separately in each bin. Taken as correlated across all bins, it is typically on the order of a few percent, but ranges up to 10% in some regions.
- *$M_{T2}$  shape uncertainty:* in regions where the simulation is used to model the  $M_{T2}$  distribution, additional variations of the renormalization and factorization scales,

parton distribution functions, b-tagging scale factor uncertainties, and jet energy scale uncertainties are performed to measure their effect on the  $M_{\text{T2}}$  shape modeling. The most significant impact is seen in the highest  $M_{\text{T2}}$  bins from theoretical uncertainties ( $\sim 15\%$ ), and up to 40% in low statistics bins due to jet energy scale variations. With this in mind, the shape uncertainty (in regions where MC  $M_{\text{T2}}$  shape modeling is used) is assigned as a linear morphing of the  $M_{\text{T2}}$  shape starting in the first bin from which MC extrapolation is used, growing to 40% in the final bin. The shape morphing in every distinct topological region is taken as an uncorrelated error.

### 5.3.3 Signal Contamination

Nearly every control region in this analysis (including those for multijet and invisible Z backgrounds) is not only orthogonal to the signal region selection, but also crafted such that any potential BSM signal contribution to any CR is negligible and will not bias the background estimate. However, certain SUSY simplified models yield final states with prompt lepton decays — in some cases kinematically similar to SM  $t\bar{t}$  decays — which may be non-negligible in the lost lepton CR. To account for this effect when calculating limits on such models (described in detail in section refsec:interpretations), the amount by which the lost lepton background is overestimated is modeled as a loss in signal efficiency. The modified signal yield  $N_{\text{sig}}^{SR'}$  is defined in equation 5.5, where  $N_{\text{sig}}^{SR}$  and  $N_{\text{sig}}^{CR}$  represent the simulated signal yield in the signal and control regions respectively, and  $TF$  the total

transfer factor used in the lost lepton estimate for a given signal region.

$$N_{\text{sig}}^{SR'} = N_{\text{sig}}^{SR} - TF \cdot N_{\text{sig}}^{CR} \quad (5.5)$$

The correction is most significant for simplified models with stop decays, where the stop-neutralino mass splitting is close to the SM top quark mass. In such cases, the signal contamination is maximally 5% of the expected background yields in each CR for mass points near the expected exclusion limits at high mass.

## 5.4 Invisible Z Estimate

The invisible Z background is the dominant SM contribution in many signal regions due to the “irreducible” nature of the underlying physics. Because the primary interaction produces a massive particle decaying to an invisible final state ( $Z \rightarrow \nu\bar{\nu}$ ) recoiling against hadronic activity, the signature is fundamentally similar to that of the BSM physics the search is designed to target and difficult to reduce by conventional cuts removing SM background contributions. A robust method leveraging the well-understood Drell-Yan process ( $Z \rightarrow l^+l^-$ ) — kinematically similar to the invisible Z background — is used to predict the expected SM contribution based on data while minimizing the reliance on Monte Carlo modeling of the kinematics.

### 5.4.1 Background Prediction

The invisible Z background is estimated using dilepton events selected in data. The control region consists of events selected with dilepton triggers, with addition requirements

that the leptons are of the same flavor and opposite sign. The momentum of the leading and trailing lepton must also be at least 100 GeV and 30 GeV, respectively, and the invariant mass of the lepton system  $m_{\ell\ell}$  must be within 20 GeV of the Z boson mass. The individual CRs are then constructed by removing the dilepton system from the event and applying the baseline preselection requirements as for the signal regions. A detailed description of the CR can be found in section 4.5.2.

The invisible Z prediction is computed as described by equation 5.6, where  $N_{\ell\ell}^{\text{CR(SF)}}$  is the number of events in the dilepton same-flavor (SF) region,  $N_{\ell\ell}^{\text{CR(OF)}}$  the number of events in the dilepton opposite-flavor (OF) region,  $R^{\text{SF/OF}}$  the SF-OF transfer factor,  $R_{\text{MC}}^{Z \rightarrow \nu\bar{\nu}/Z \rightarrow l^+l^-}$  the transfer factor from  $Z \rightarrow l^+l^-$  to  $Z \rightarrow \nu\bar{\nu}$  events, and  $k(M_{\text{T2}})$  the transfer factor into bins of  $M_{\text{T2}}$ . Each factor is explained in detail below.

$$N_{Z \rightarrow \nu\bar{\nu}}^{\text{SR}}(H_{\text{T}}, N_{\text{j}}, N_{\text{b}}, M_{\text{T2}}) = \left[ N_{\ell\ell}^{\text{CR(SF)}}(H_{\text{T}}, N_{\text{j}}, N_{\text{b}}) - N_{\ell\ell}^{\text{CR(OF)}}(H_{\text{T}}, N_{\text{j}}, N_{\text{b}}) \cdot R^{\text{SF/OF}} \right] \\ \times R_{\text{MC}}^{Z \rightarrow \nu\bar{\nu}/Z \rightarrow l^+l^-}(H_{\text{T}}, N_{\text{j}}, N_{\text{b}}) \cdot k(M_{\text{T2}}) \quad (5.6)$$

The second term in equation 5.6,  $N_{\ell\ell}^{\text{CR(OF)}} \cdot R^{\text{SF/OF}}$ , is a correction factor applied to the control region yield to correct for the contribution from processes producing SF and OF event, or *flavor-symmetric processes* (such as  $t\bar{t}$ ). To compensate for this contribution, a separate control region enriched in  $t\bar{t}$  events is selected from data by using the same selections as the invisible Z CR, except for an inverted selection on the dilepton  $p_{\text{T}}$  and  $m_{\ell\ell}$  requirements. The ratio of  $t\bar{t}$  events is then measured directly from data by counting the yield of SF ( $ee$  or  $\mu\mu$ ) and OF ( $e\mu$  or  $\mu e$ ) events in this CR. The ratio  $R^{\text{SF/OF}}$  is expected to be close to unity based on the underlying physics process, but due to varying acceptance

and efficiency effects for different flavor leptons is measured as  $R^{\text{SF}/\text{OF}} = 1.13 \pm 0.15$ , and is stable with respect to event kinematics as shown in figure 5.7. The Drell-Yan yield in each control region, as well as the SF yield, OF yield, and transfer factors can be found in tables 5.3 and 5.4.

The ratio of invisible Z events to Drell-Yan events,  $R_{\text{MC}}^{Z \rightarrow \nu\bar{\nu}/Z \rightarrow l^+l^-}$ , is measured in simulation for each CR. The ratio accounts for the branching fraction differences between  $Z \rightarrow l^+l^-$  and  $Z \rightarrow \nu\bar{\nu}$  decays, as well as differences in lepton acceptance and efficiency for dilepton pairs in the CR (including corrections for differences in lepton efficiency between data and simulation).

The transfer factor  $k(M_{\text{T2}})$  uses a combination of data and simulation information to reduce the dependence of the prediction on the  $M_{\text{T2}}$  shape modeling in simulation. Based on simulation, the  $M_{\text{T2}}$  shape in ever  $H_{\text{T}}$  region is independent of  $N_{\text{b-jets}}$ . In addition, in the extreme  $H_{\text{T}}$  region  $H_{\text{T}} > 1500 \text{ GeV}$ , the shape is also independent of  $N_{\text{jets}}$ . Based on these findings,  $M_{\text{T2}}$  shape templates are constructed for each  $H_{\text{T}}$  and  $N_{\text{jets}}$  region (inclusive in  $N_{\text{b-jets}}$ <sup>1</sup>), with one single template for the extreme  $H_{\text{T}}$  region (which is also inclusive in  $N_{\text{jets}}$ ).

The  $M_{\text{T2}}$  distribution,  $k(M_{\text{T2}})$ , for each topological region is constructed from dilepton events in data where statistics allows, and  $Z \rightarrow \nu\bar{\nu}$  simulation where statistics are sparse. In each template region, the greatest  $M_{\text{T2}}$  bin is iteratively combined with the next-greatest bin until the total expected SM background yield in simulation is at least 50

---

<sup>1</sup>The only exception is for regions with more than 2 b-tags (2j3b and 2-6j3b), where at least 3 jets are required so as to avoid biasing the  $N_{\text{jets}}$  distribution when requiring more b-tags than jets.

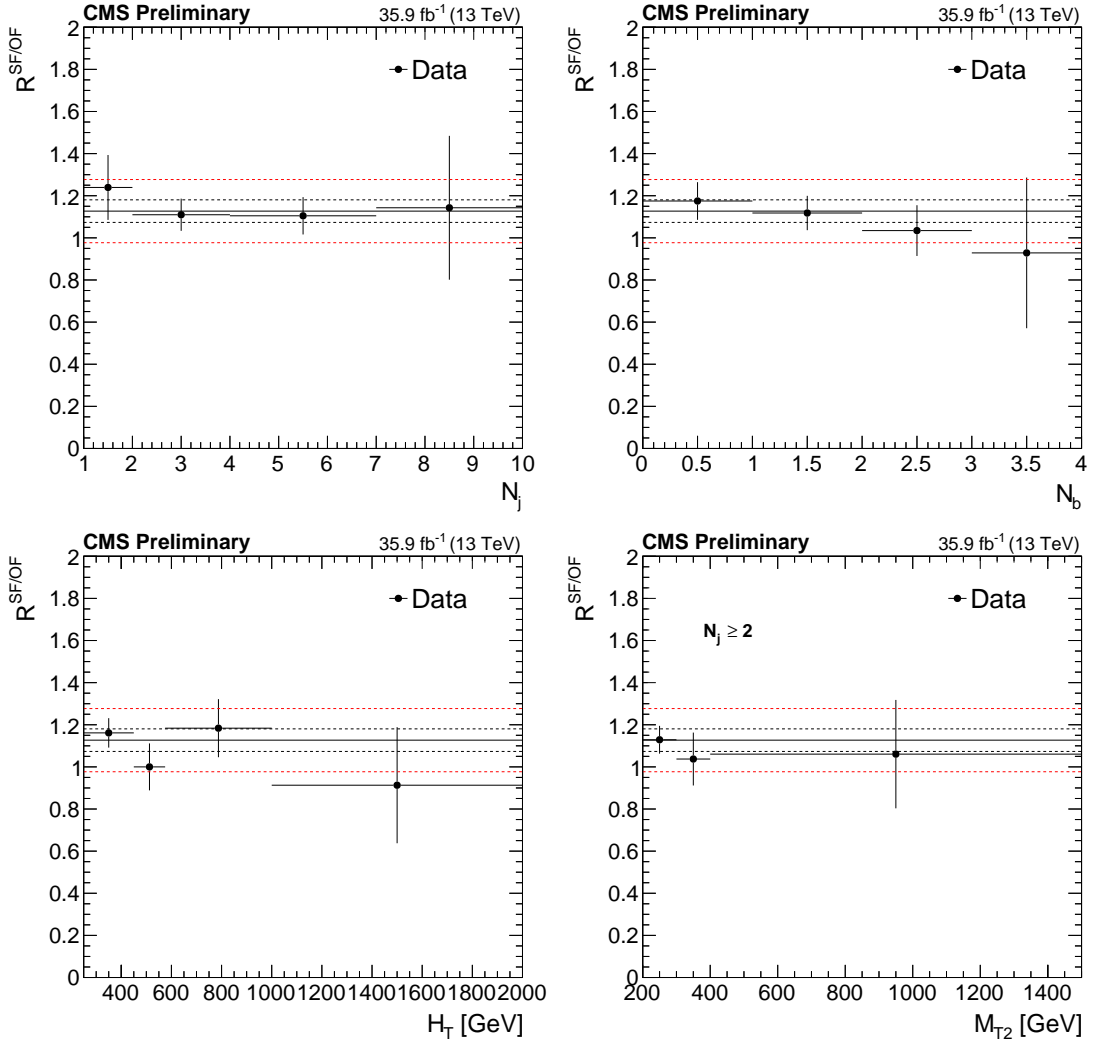


**Figure 5.7:** The ratio of same-flavor to opposite-flavor events in a  $t\bar{t}$  enriched control region, as a function of  $N_{\text{jets}}$  (top left),  $N_{\text{b-jets}}$  (top right),  $H_T$  (bottom left), and  $M_{T2}$  (bottom right). The solid black line corresponds to a constant value of  $1.13 \pm 0.15$ , while the dashed black lines correspond to the statistical uncertainty and the dashed red lines the total systematic uncertainty.

**Table 5.3:** The control region predicted Drell-Yan (DY) yield, SF yield, OF yield, purity (the rfraction of  $Z \rightarrow l^+l^-$  events), and ratio  $R_{\text{MC}}^{Z \rightarrow \nu\bar{\nu}/Z \rightarrow l^+l^-}$  for the very low, low, and medium  $H_T$  topological regions. Note that the 7+ jet regions with b-tags (marked with an asterisk) share the same CR, and the fraction of events with different numbers of b-tags is folded into the ratio.

Invisible Z							
Region			DY Yield	SF Yield	OF Yield	Purity	Ratio
$H_T$ [GeV]	$N_j$	$N_b$					
[250, 450]	2-3	0	8707.6	8749	37	$0.995 \pm 0.001$	5.61
[250, 450]	2-3	1	986.0	1005	17	$0.981 \pm 0.004$	5.47
[250, 450]	2-3	2	122.8	125	2	$0.982 \pm 0.012$	5.31
[250, 450]	4+	0	1124.5	1129	4	$0.996 \pm 0.002$	5.88
[250, 450]	4+	1	215.2	223	7	$0.965 \pm 0.012$	5.70
[250, 450]	4+	2	35.9	37	1	$0.970 \pm 0.028$	5.52
[250, 450]	2-3	3+	7.0	7	0	$1.000 \pm 0.000$	6.29
[450, 575]	2-3	0	1862.7	1875	11	$0.993 \pm 0.002$	5.08
[450, 575]	2-3	1	273.2	281	7	$0.972 \pm 0.010$	4.89
[450, 575]	2-3	2	19.8	22	2	$0.898 \pm 0.064$	4.75
[450, 575]	4-6	0	650.9	661	9	$0.985 \pm 0.005$	5.49
[450, 575]	4-6	1	143.4	149	5	$0.962 \pm 0.016$	5.58
[450, 575]	4-6	2	27.6	31	3	$0.892 \pm 0.056$	5.21
[450, 575]	7+	0	7.0	7	0	$1.000 \pm 0.000$	5.56
[450, 575]	7+	1	4.0	4	0	$1.000 \pm 0.000$	5.18 <sup>(*)</sup>
[450, 575]	7+	2	4.0	4	0	$1.000 \pm 0.000$	1.87 <sup>(*)</sup>
[450, 575]	2-6	3+	7.0	7	0	$1.000 \pm 0.000$	5.78
[450, 575]	7+	3+	4.0	4	0	$1.000 \pm 0.000$	0.48 <sup>(*)</sup>
[575, 1000]	2-3	0	1347.0	1356	8	$0.993 \pm 0.002$	4.76
[575, 1000]	2-3	1	157.3	164	6	$0.959 \pm 0.015$	4.55
[575, 1000]	2-3	2	25.8	28	2	$0.920 \pm 0.051$	4.68
[575, 1000]	4-6	0	812.4	818	5	$0.993 \pm 0.003$	5.16
[575, 1000]	4-6	1	180.0	189	8	$0.953 \pm 0.015$	5.09
[575, 1000]	4-6	2	26.3	33	6	$0.796 \pm 0.070$	5.29
[575, 1000]	7+	0	32.9	34	1	$0.967 \pm 0.031$	5.84
[575, 1000]	7+	1	15.6	19	3	$0.823 \pm 0.088$	4.41 <sup>(*)</sup>
[575, 1000]	7+	2	15.6	19	3	$0.823 \pm 0.088$	1.10 <sup>(*)</sup>
[575, 1000]	2-6	3+	5.8	8	2	$0.720 \pm 0.159$	5.82
[575, 1000]	7+	3+	15.6	19	3	$0.823 \pm 0.088$	0.22 <sup>(*)</sup>

**Table 5.4:** The control region predicted Drell-Yan (DY) yield, SF yield, OF yield, purity (the rfraction of  $Z \rightarrow l^+l^-$  events), and ratio  $R_{\text{MC}}^{Z \rightarrow \nu\bar{\nu}/Z \rightarrow l^+l^-}$  for the high and extreme  $H_T$  topological regions. Note that the 7+ jet regions with b-tags (marked with an asterisk) share the same CR, and the fraction of events with different numbers of b-tags is folded into the ratio.

Invisible Z								
Region	$H_T$ [GeV]	$N_j$	$N_b$	DY Yield	SF Yield	OF Yield	Purity	Ratio
[1000, 1500]	2-3	0	129.0	129	0	1.000±0.000	4.76	
[1000, 1500]	2-3	1	25.9	27	1	0.959±0.038	4.63	
[1000, 1500]	2-3	2	1.9	3	1	0.627±0.279	4.73	
[1000, 1500]	4-6	0	154.0	154	0	1.000±0.000	5.10	
[1000, 1500]	4-6	1	42.0	42	0	1.000±0.000	4.97	
[1000, 1500]	4-6	2	11.0	11	0	1.000±0.000	5.07	
[1000, 1500]	7+	0	19.0	19	0	1.000±0.000	5.63	
[1000, 1500]	7+	1	10.0	10	0	1.000±0.000	4.63 <sup>(*)</sup>	
[1000, 1500]	7+	2	10.0	10	0	1.000±0.000	1.22 <sup>(*)</sup>	
[1000, 1500]	2-6	3+	1.0	1	1	1.000±1.000	4.25	
[1000, 1500]	7+	3+	10.0	10	0	1.000±0.000	0.20 <sup>(*)</sup>	
[1500, ∞]	2-3	0	29.0	29	0	1.000±0.000	5.00	
[1500, ∞]	2-3	1	8.0	8	0	1.000±0.000	4.66	
[1500, ∞]	4-6	0	28.9	30	1	0.963±0.035	5.09	
[1500, ∞]	4-6	1	14.0	14	0	1.000±0.000	5.25	
[1500, ∞]	4-6	2	2.9	4	1	0.720±0.224	4.80	
[1500, ∞]	7+	0	5.0	5	0	1.000±0.000	5.16	
[1500, ∞]	7+	1	1.9	3	1	0.627±0.279	3.97 <sup>(*)</sup>	
[1500, ∞]	7+	2	1.9	3	1	0.627±0.279	1.18 <sup>(*)</sup>	
[1500, ∞]	2-6	3+	1.0	1	0	1.000±0.000	6.27	
[1500, ∞]	7+	3+	1.9	3	1	0.627±0.279	0.18 <sup>(*)</sup>	

events. For uncombined bins (where statistics in data is sufficient), the  $M_{\mathrm{T}2}$  shape is taken directly from dilepton data, corrected for the ratio  $R_{\mathrm{MC}}^{Z \rightarrow \nu\bar{\nu}/Z \rightarrow l^+l^-}$ . In the low-statistics combined regime, the  $M_{\mathrm{T}2}$  shape in  $Z \rightarrow \nu\bar{\nu}$  simulation is used to determine the fraction of events in each  $M_{\mathrm{T}2}$  bin after normalizing the simulation yield to data in the combined bins. The extrapolation point after which the  $M_{\mathrm{T}2}$  shape is based on simulation in each signal region can be found in tables 5.5 and 5.6.

The accuracy of the  $M_{\mathrm{T}2}$  shape modeling in simulation is verified using other control samples enriched in  $\gamma$ ,  $W \rightarrow \ell\nu$ , and  $Z \rightarrow l^+l^-$  events in each  $H_{\mathrm{T}}$  bin, as shown in figure 5.8. The  $\gamma$ -enriched sample is selected using photon triggers and requiring  $p_{\mathrm{T}}^{\gamma} > 180 \text{ GeV}$ , with corrections applied for multijet background contributions and the ratio of  $M_{\mathrm{T}2}$  distributions for photon to Z boson events,  $R_{\mathrm{MC}}^{Z/\gamma}$ . The W and Z boson samples are selected in data using leptonic triggers, corrected to compensate for the contribution from top quark production, as well as the ratio of  $M_{\mathrm{T}2}$  distributions,  $R_{\mathrm{MC}}^{Z/W}$  and  $R_{\mathrm{MC}}^{Z \rightarrow \nu\bar{\nu}/Z \rightarrow l^+l^-}$  respectively.

### 5.4.2 Systematic Uncertainties

Several sources of uncertainty are assessed for the invisible Z estimate, including those associated with the various transfer factors and the  $M_{\mathrm{T}2}$  shape modeling in simulation. The dominant uncertainty in regions using an  $M_{\mathrm{T}2}$  template constructed from data is the statistics of the template. The full list of systematic uncertainties is as follows:

**Table 5.5:** The  $M_{T2}$  extrapolation point for the very low, low, and medium  $H_T$  topological regions, beyond which shape data from simulation is used to extrapolate the invisible Z estimate into  $M_{T2}$  bins. “NA” indicates regions where the simulation shape is not used at all since dilepton statistics in data are sufficiently large to perform the estimate bin-by-bin.

$H_T$ [GeV]	Template Region		Invisible Z
	$N_j$	$N_b$	Extrapolation Point $M_{T2}$ [GeV]
[250, 450]	2-3	0	NA
[250, 450]	2-3	1	NA
[250, 450]	2-3	2	NA
[250, 450]	4+	0	300
[250, 450]	4+	1	300
[250, 450]	4+	2	300
[250, 450]	2+	3+	NA
[450, 575]	2-3	0	400
[450, 575]	2-3	1	400
[450, 575]	2-3	2	400
[450, 575]	4-6	0	400
[450, 575]	4-6	1	400
[450, 575]	4-6	2	400
[450, 575]	7+	0	200
[450, 575]	7+	1	200
[450, 575]	7+	2	200
[450, 575]	2-6	3+	NA
[450, 575]	7+	3+	200
[575, 1000]	2-3	0	600
[575, 1000]	2-3	1	600
[575, 1000]	2-3	2	600
[575, 1000]	4-6	0	600
[575, 1000]	4-6	1	600
[575, 1000]	4-6	2	600
[575, 1000]	7+	0	200
[575, 1000]	7+	1	200
[575, 1000]	7+	2	200
[575, 1000]	2-6	3+	NA
[575, 1000]	7+	3+	200

**Table 5.6:** The  $M_{T2}$  extrapolation point for the high and extreme  $H_T$  topological regions, beyond which shape data from simulation is used to extrapolate the invisible Z estimate into  $M_{T2}$  bins. “NA” indicates regions where the simulation shape is not used at all since dilepton statistics in data are sufficiently large to perform the estimate bin-by-bin.

Invisible Z			
Template Region		Extrapolation Point	
$H_T$ [GeV]	$N_j$	$N_b$	$M_{T2}$ [GeV]
[1000, 1500]	2-3	0	400
[1000, 1500]	2-3	1	400
[1000, 1500]	2-3	2	400
[1000, 1500]	4-6	0	400
[1000, 1500]	4-6	1	400
[1000, 1500]	4-6	2	400
[1000, 1500]	7+	0	200
[1000, 1500]	7+	1	200
[1000, 1500]	7+	2	200
[1000, 1500]	2-6	3+	NA
[1000, 1500]	7+	3+	200
[1500, $\infty$ ]	2-3	0	400
[1500, $\infty$ ]	2-3	1	400
[1500, $\infty$ ]	4-6	0	400
[1500, $\infty$ ]	4-6	1	400
[1500, $\infty$ ]	4-6	2	400
[1500, $\infty$ ]	7+	0	400
[1500, $\infty$ ]	7+	1	400
[1500, $\infty$ ]	7+	2	400
[1500, $\infty$ ]	2-6	3+	400
[1500, $\infty$ ]	7+	3+	400

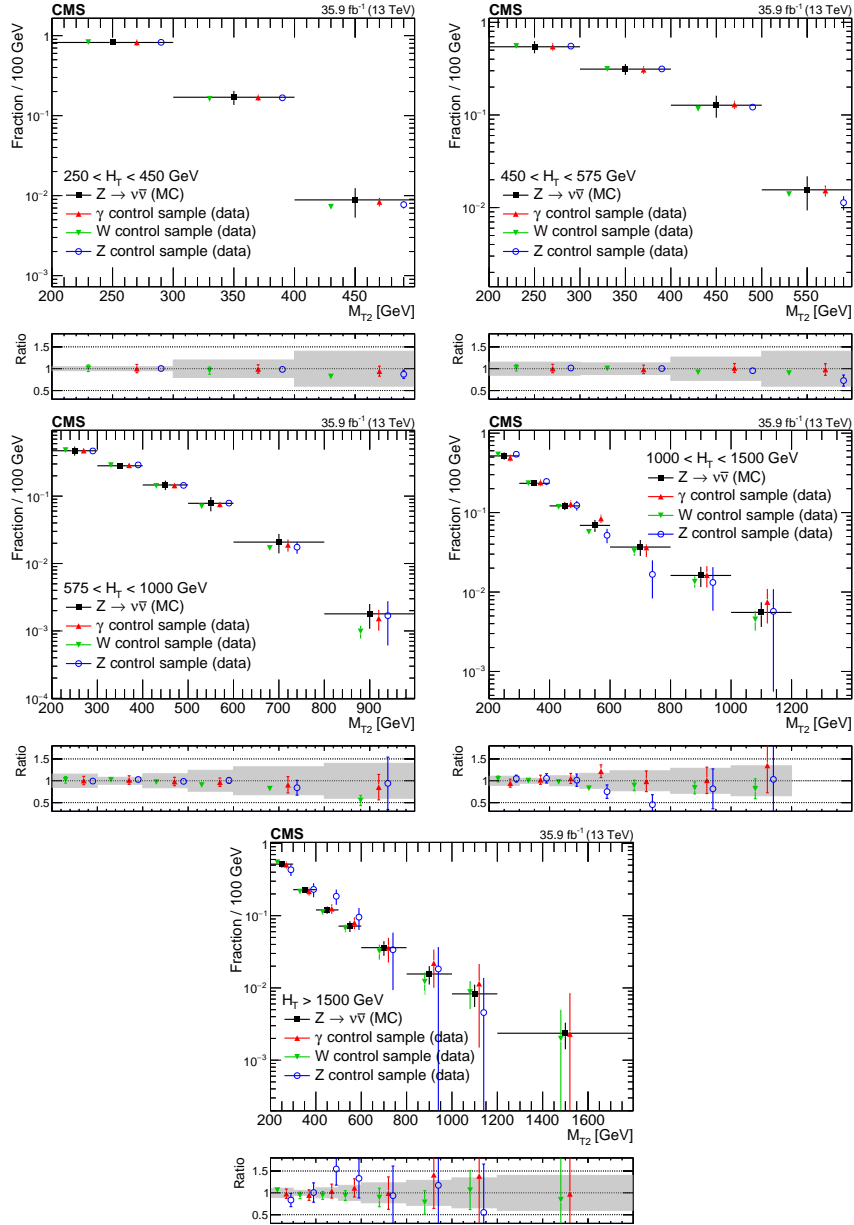


**Figure 5.8:** The  $M_{T2}$  shape distribution in  $Z \rightarrow \nu\bar{\nu}$  simulation compared to  $\gamma$ ,  $W \rightarrow \ell\nu$ , and  $Z \rightarrow l^+l^-$  enriched samples in data, for each  $H_T$  region. The solid grey band indicates the systematic uncertainty associated with the  $M_{T2}$  shape modeling.

- *Control region statistical error*: the Poisson error on the number of observed events in  $Z \rightarrow l^+l^-$  data is taken as an uncorrelated uncertainty across all signal regions.
- $R_{\text{MC}}^{Z \rightarrow \nu\bar{\nu}/Z \rightarrow l^+l^-}$  *statistical error*: the statistical error associated with the number of MC events generated factors into the transfer factor.
- $R_{\text{MC}}^{Z \rightarrow \nu\bar{\nu}/Z \rightarrow l^+l^-}$  *systematic error*: a 5.5% uncertainty based on variations of lepton efficiency uncertainties as well as other modeling parameters (jet energy scales, factorization and renormalization scales, etc.) is applied as a correlated error in each topological region.
- *Flavor-symmetric subtraction statistical error*: a Poisson error based on the number of observed opposite-flavor events.
- *Flavor-symmetric subtraction systematic error*: a 15% uncertainty on the  $t\bar{t}$  contamination based on the  $R^{\text{SF/OF}}$  uncertainty.
- *$M_{\text{T2}}$  shape uncertainty*: in regions where the simulation is used to model the  $M_{\text{T2}}$  distribution, additional variations of the renormalization and factorization scales, parton distribution functions, b-tagging scale factor uncertainties, and jet energy scale uncertainties are performed to measure their effect on the  $M_{\text{T2}}$  shape modeling. The most significant impact is seen in the highest  $M_{\text{T2}}$  bins of up to 20%. In order to cover the uncertainty from additional electro-weak corrections not present in simulation (and possibly not covered by the above variations), a conservative upper threshold of 40% is used, and the shape uncertainty (in regions where MC

$M_{T2}$  shape modeling is used) is assigned as a linear morphing of the  $M_{T2}$  shape starting in the first bin from which MC extrapolation is used, growing to 40% in the final bin. The shape morphing in every distinct topological region is taken as an uncorrelated error.

This work would not have been possible without all the members of the CMS collaboration, whose support made it possible to produce the figures and tables in this chapter.

# Chapter 6

## Results

The techniques described in this analysis are applied to  $35.9\text{fb}^{-1}$  of proton-proton collision data gathered at the LHC and recorded by the CMS detector. Observed yields in each signal region are further interpreted in the context of simplified SUSY models to establish new limits on the masses of hypothesized BSM particles.

### 6.1 Yields and Background Fits

The observed yield in the search regions is statistically compatible with the predicted background from SM processes. A summary of the total yield in each signal region and predicted background contribution relying only on the techniques described in chapter 5, referred to as *pre-fit* results, is illustrated for each topological region in figure 6.1, and the individual yield in each  $M_{\text{T2}}$  bin can be found in figures 6.2, 6.3, and 6.4.

The background estimate is further refined by performing a maximum-likelihood fit

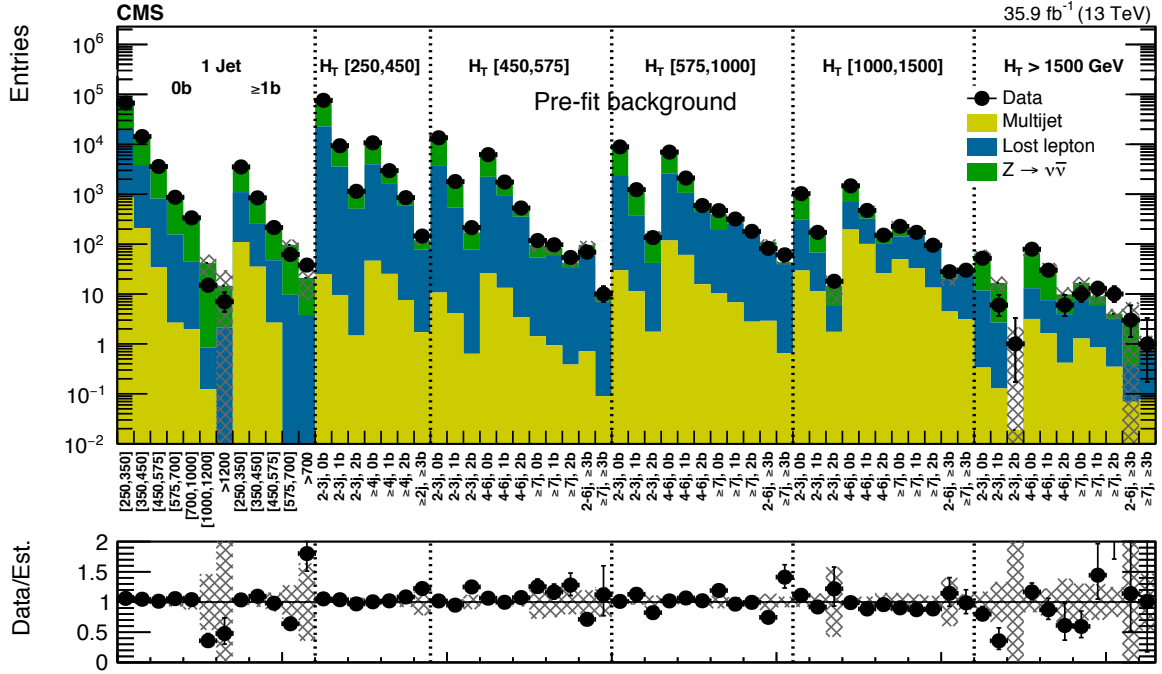


**Figure 6.1:** The data yield in each topological region compared to the pre-fit background prediction. The hatched bands illustrate the total uncertainty in the background estimate. Results in the monojet regions are binned in jet  $p_T$ , while those in the multijet regions are labeled according to  $N_{\text{jets}}$  and  $N_{\text{b-jets}}$ .

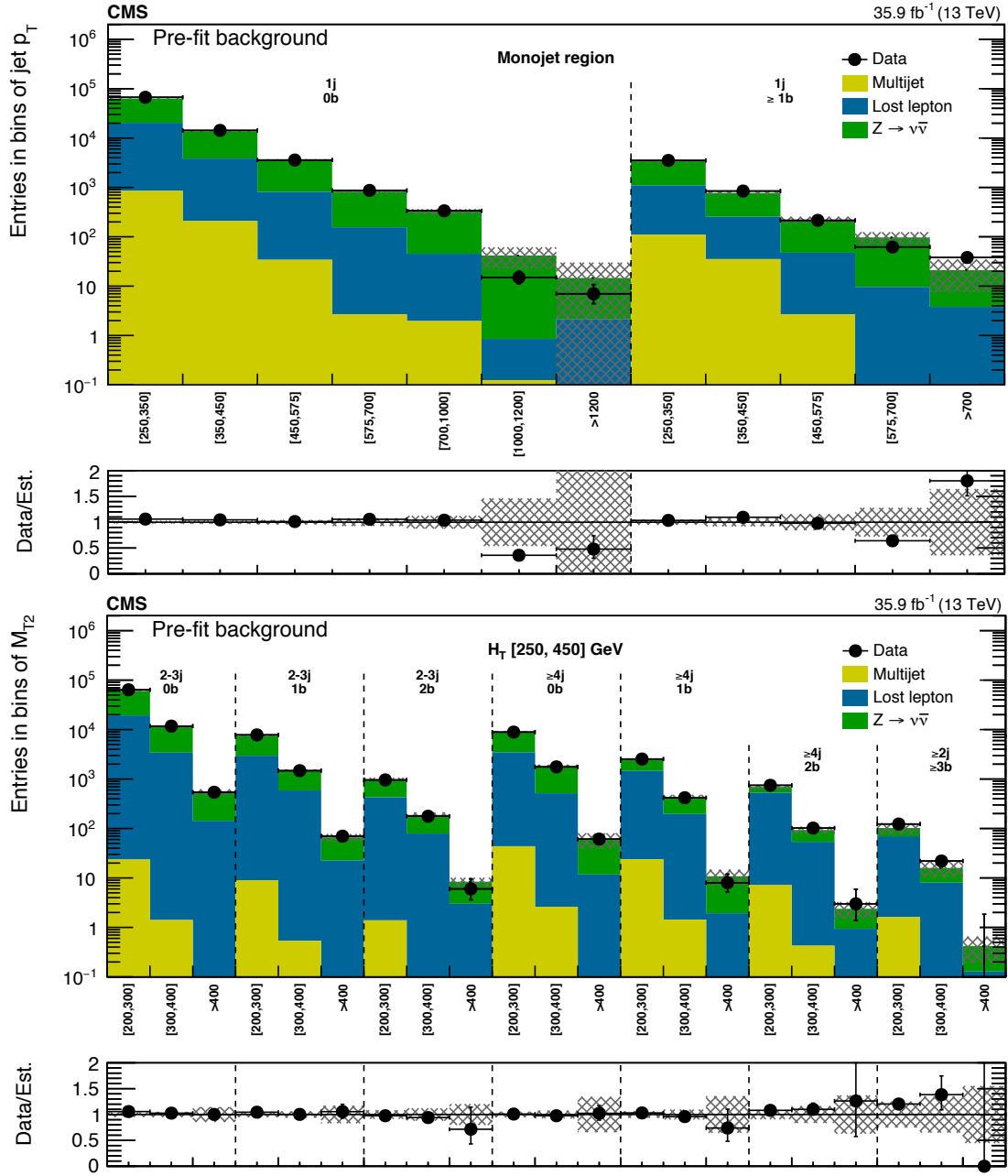


**Figure 6.2:** The data yield in the monojet and very-low  $H_T$  regions compared to the pre-fit background prediction. The hatched bands illustrate the total uncertainty in the background estimate. Results in the monojet regions are binned in jet  $p_T$  in units of GeV, while those in the multijet regions are labeled according to  $M_{T2}$  bin in units of GeV.

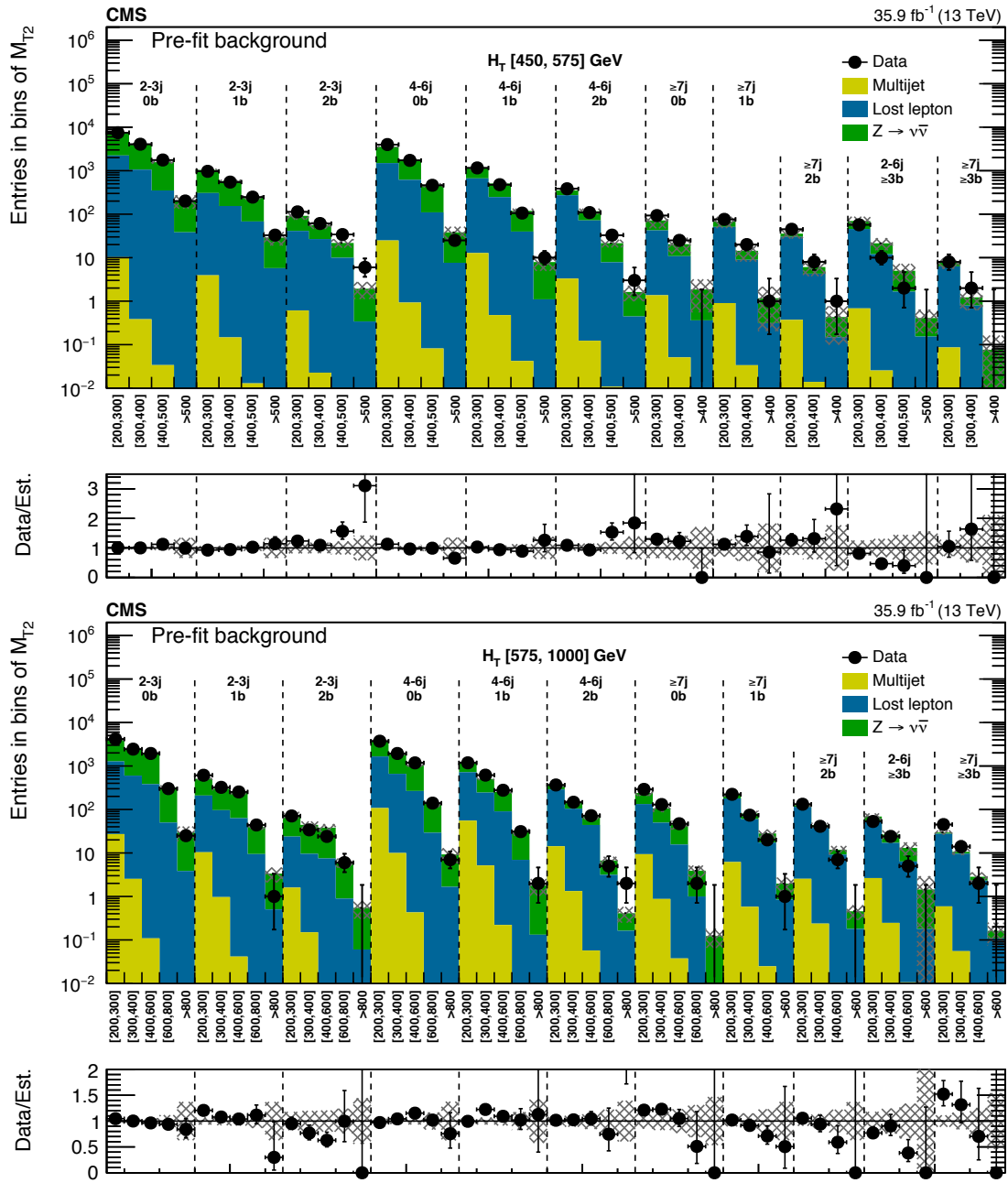


**Figure 6.3:** The data yield in the low  $H_T$  and medium  $H_T$  regions compared to the pre-fit background prediction. The hatched bands illustrate the total uncertainty in the background estimate. Results are labeled according to  $M_{T2}$  bin in units of GeV.

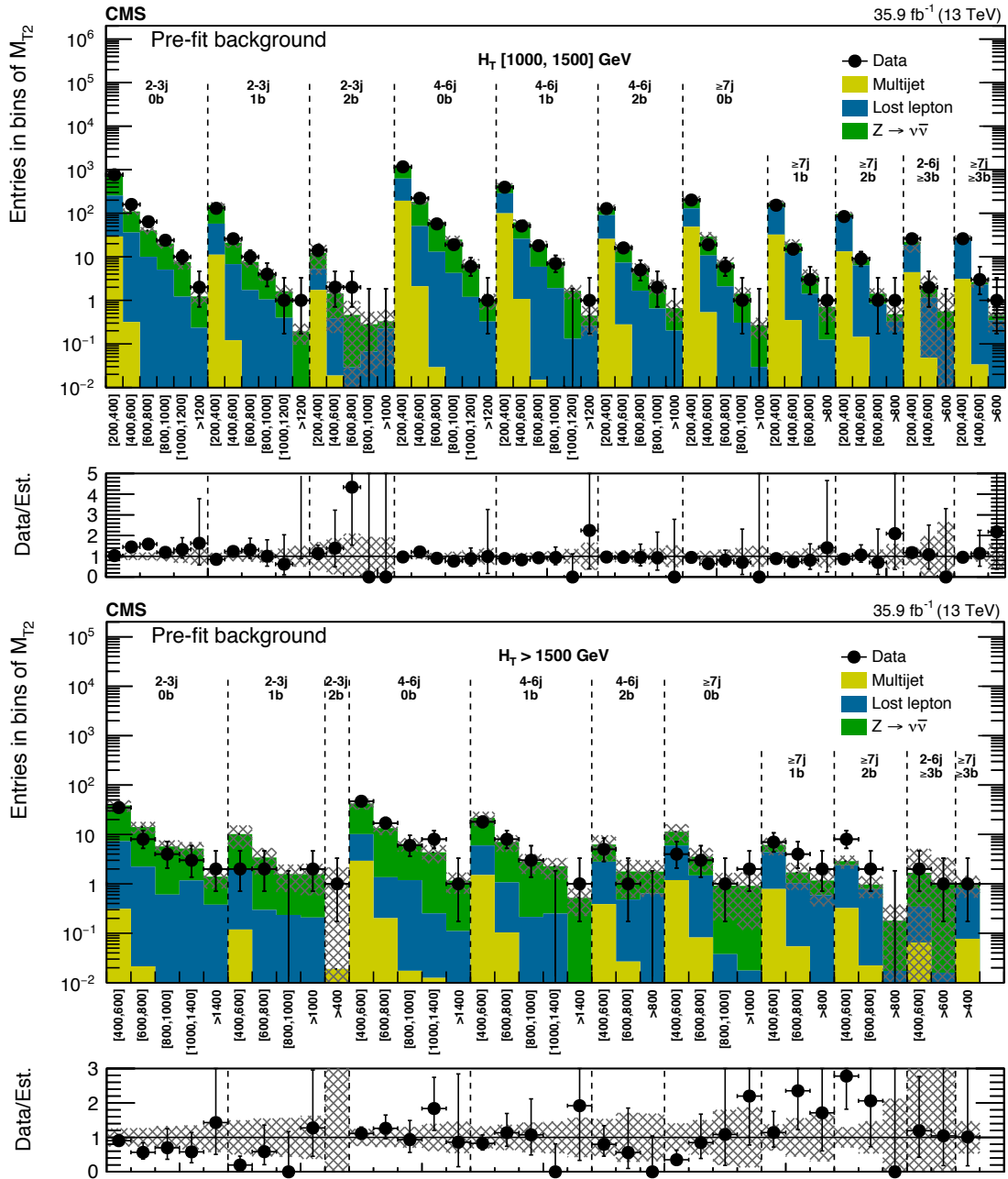


**Figure 6.4:** The data yield in the high  $H_T$  and extreme  $H_T$  regions compared to the pre-fit background prediction. The hatched bands illustrate the total uncertainty in the background estimate. Results are labeled according to  $M_{T2}$  bin in units of GeV.

to data in each signal region, referred to as *post-fit* results. The fit is performed using both background-only or background-plus-signal hypotheses to set limits on simplified physics models described in section 6.2. The estimates and uncertainties on each background as described in chapter 5 are used as inputs to the fitting procedure, where the likelihood is constructed as a product of Poisson probability density functions for each signal region with constraints set according to the background uncertainties and signal uncertainties (described in section 6.2.1). The post-fit yield for each topological region is illustrated in figure 6.5, and the individual yield in each  $M_{T2}$  bin can be found in figures 6.6, 6.7, and 6.8. The post-fit procedure has the effect of constraining background and its associated uncertainties when the fitting procedure is applied to data consistent with predictions modeling uncertainties appropriately.

## 6.2 Signal Interpretations

The results of the search can be interpreted as a constraint on the mass of hypothesized particles of various BSM models. Based on the simulated production processes of simplified SUSY models, this section describes some of the uncertainties associated with the signal yield, as well as the limits associated with various simplified models of interest.

### 6.2.1 Signal Yield Systematic Uncertainties

The uncertainties associated with the signal yield are summarized in table 6.1. The various sources of uncertainty are described in detail below:

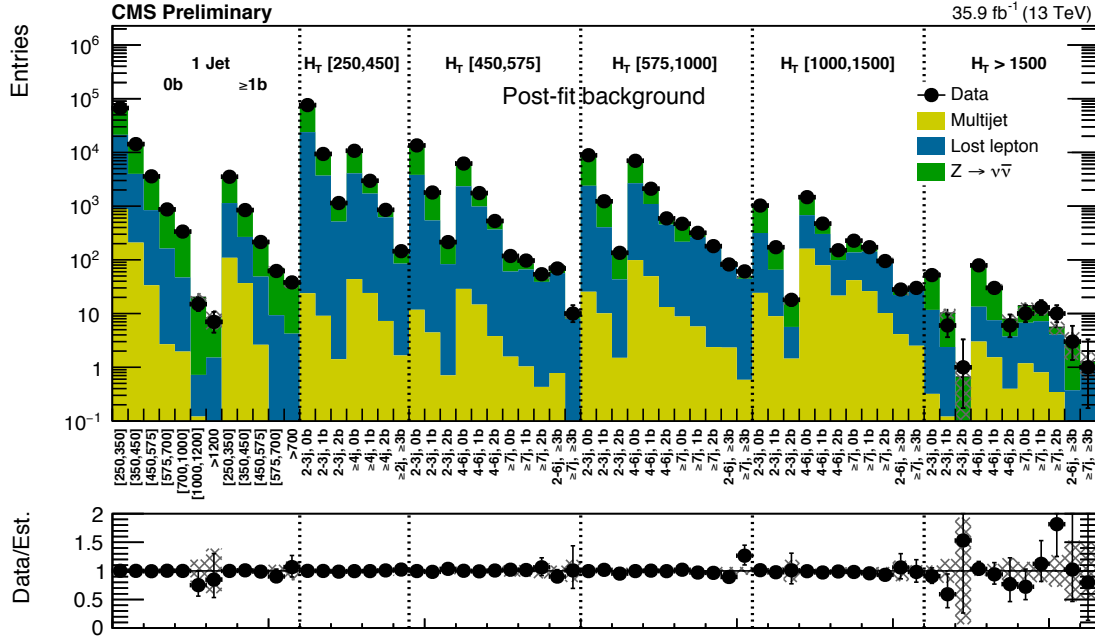


**Figure 6.5:** The data yield in each topological region compared to the post-fit background prediction. The hatched bands illustrate the total uncertainty in the background estimate. Results in the monojet regions are binned in jet  $p_T$ , while those in the multijet regions are labeled according to  $N_{\text{jets}}$  and  $N_{\text{b-jets}}$ .

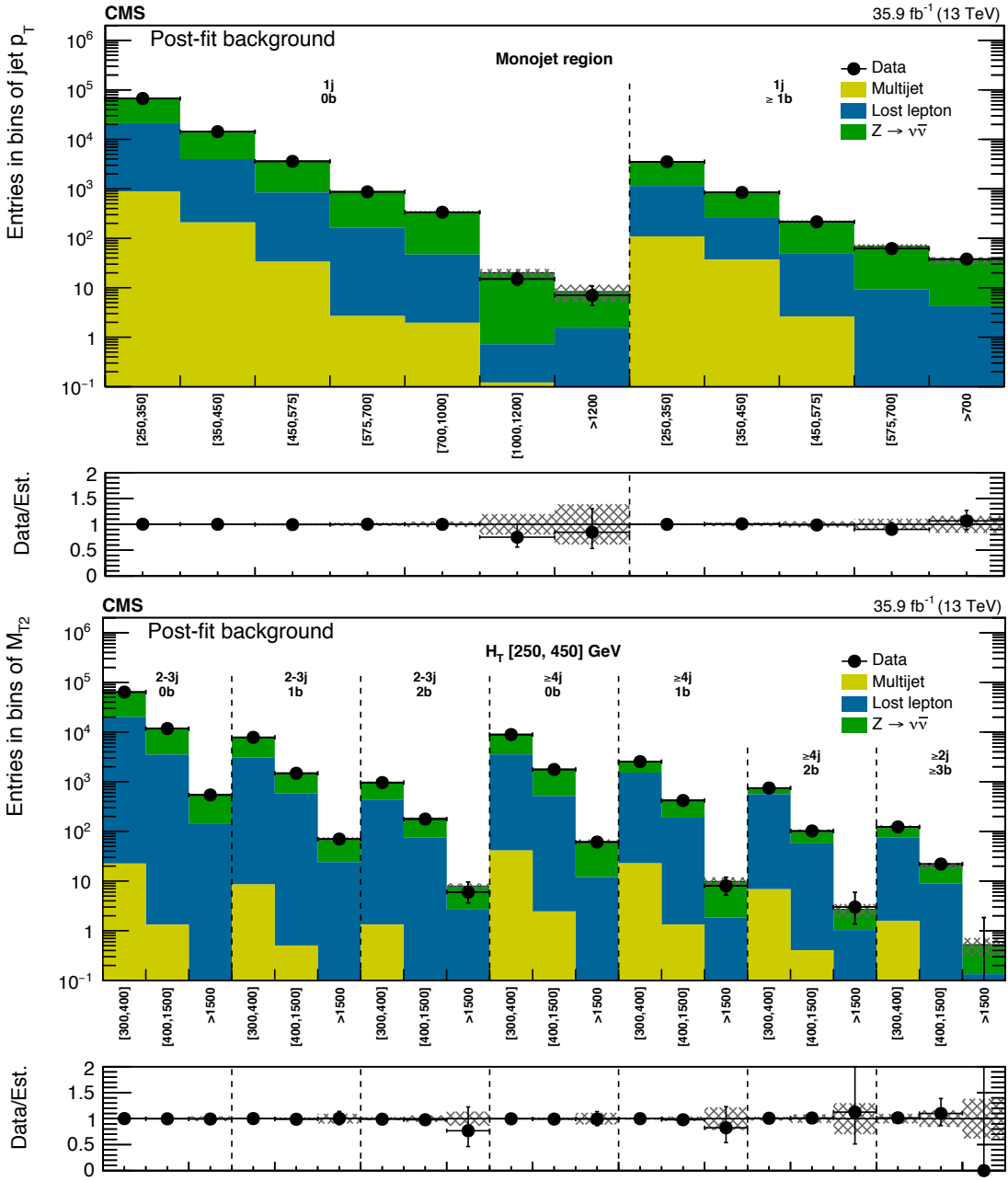


**Figure 6.6:** The data yield in the monojet and very-low  $H_T$  regions compared to the post-fit background prediction. The hatched bands illustrate the total uncertainty in the background estimate. Results in the monojet regions are binned in jet  $p_T$  in units of GeV, while those in the multijet regions are labeled according to  $M_{T2}$  bin in units of GeV.

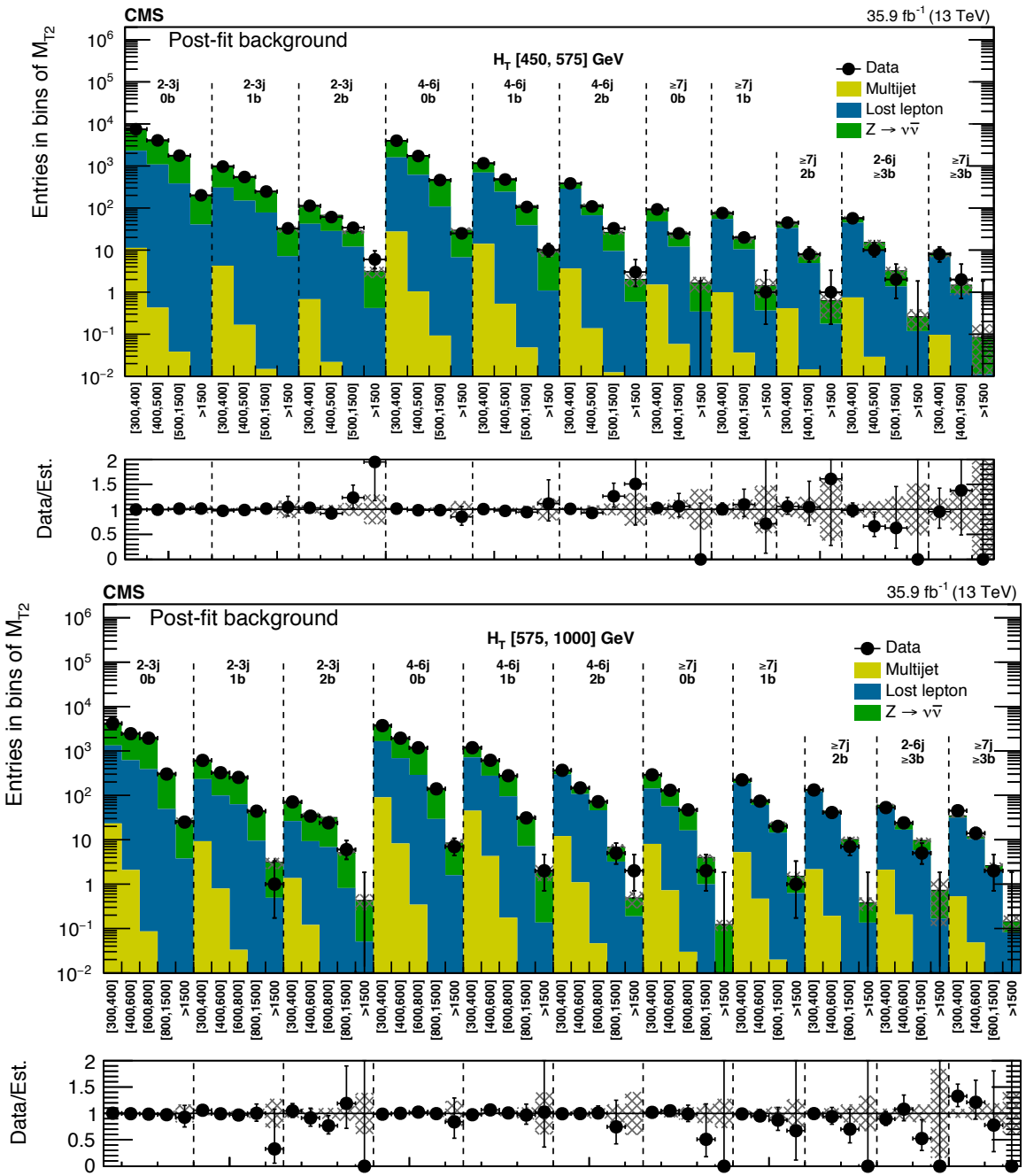


**Figure 6.7:** The data yield in the low  $H_T$  and medium  $H_T$  regions compared to the post-fit background prediction. The hatched bands illustrate the total uncertainty in the background estimate. Results are labeled according to  $M_{T2}$  bin in units of GeV.

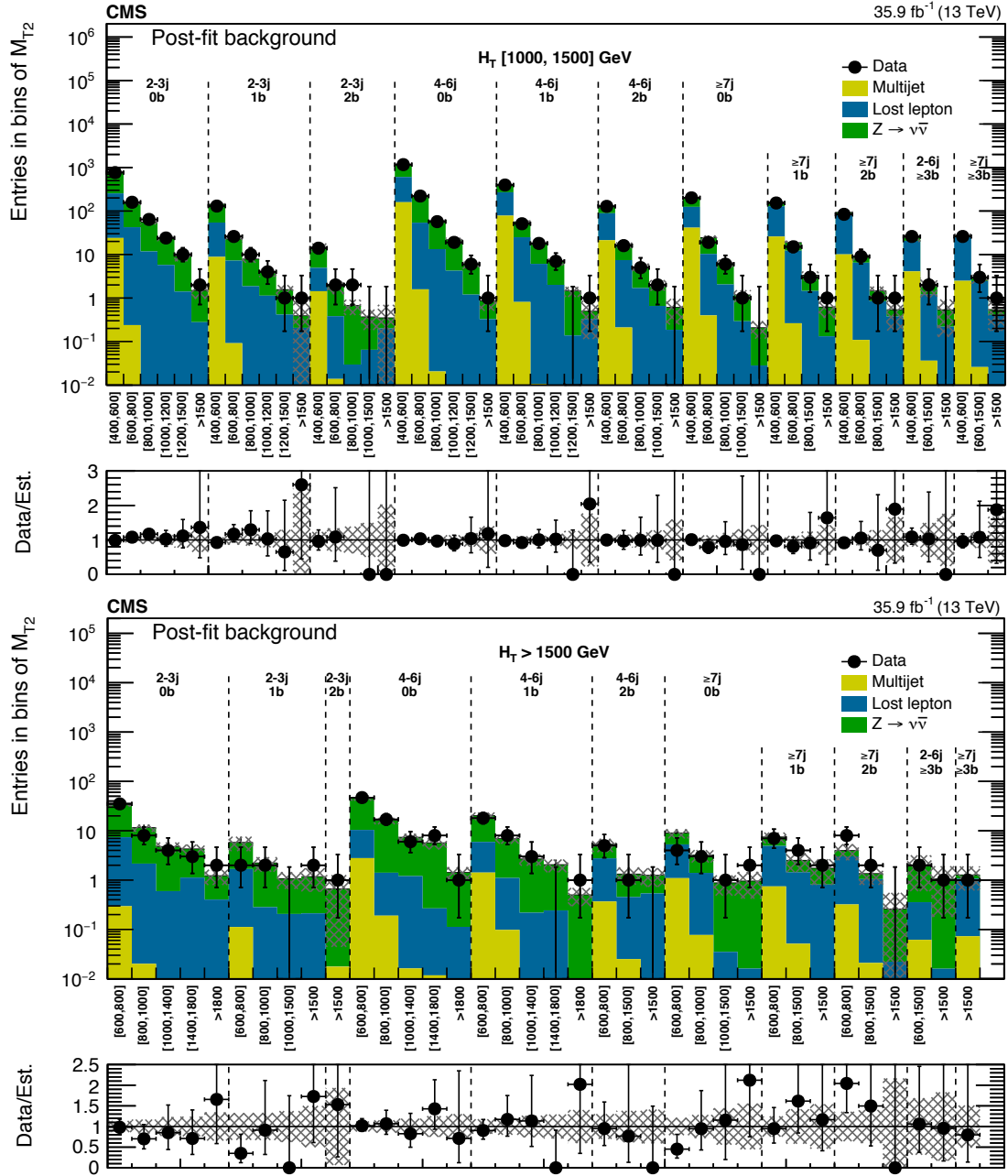


**Figure 6.8:** The data yield in the high  $H_T$  and extreme  $H_T$  regions compared to the post-fit background prediction. The hatched bands illustrate the total uncertainty in the background estimate. Results are labeled according to  $M_{T2}$  bin in units of GeV.

- *Luminosity*: the uncertainty of the total integrated luminosity delivered by the LHC is evaluated in *Van Der Meer scans*, where the rate of interactions is measured while scanning the colliding proton beams across each other. The uncertainty in the luminosity based on these studies is 2.5%.
- *Simulation statistics*: the limited size of the Monte Carlo samples for each sample effect the statistics in each signal region bin. After applying the signal selection, the statistical uncertainty can range from 1-100% in different bins, though bins with large uncertainty typically correspond to those with low signal acceptance, and thus do not drive the sensitivity of the analysis to that simplified model mass point.
- *Renormalization and factorization scales*: the overall effect of varying the simulation renormalization and factorization scales of the underlying physics processes (and subsequent effect on event kinematics) is computed separately in each bin. The result of this variation is relatively flat and minor across the signal bins, and is conservatively estimated at 5% for all regions.
- *Initial-state radiation (ISR) recoil*: variations of the boost due to initial-state radiation are performed to test the modeling of ISR effects in simulation. The effect of these variations ranges from 0-30% across signal regions.
- *b-tagging efficiency*: the effect of varying the b-tag scale factor efficiency is calculated in each bin, and taken as a correlated error amongst all bins. The effect of this variation for heavy (light) flavor jets is 0-40% (0-20%) across signal regions.

- *Lepton efficiency*: the effect of varying the electron and muon scale factors applied to simulation is calculated in each bin, and taken as a correlated error amongst all bins. The effect of this variation is 0-20% across signal regions.
- *Jet energy scale*: the effect of varying the jet energy scales is calculated in each bin, and the results are compatible with statistical uncertainty for low-statistics bins. Based on findings in the high-statistics bins, the uncertainty is estimated at 5% for all regions.
- *Fast simulation modeling*: The signal Monte Carlo samples are generated using the FastSim package, which may result in modeling differences compared to Fullsim MC. Studies of the Fastsim kinematics with respect to  $E_T^{\text{miss}}$  and pile-up modeling indicate differences of up to 5% in some signal regions.

### 6.2.2 Exclusion Limits

The final results are interpreted in the context of various simplified SUSY models: gluino-mediated squark pair production, direct production of squarks, and alternative models of top squark production with different decay modes. Each of these models is illustrated in figure 6.9. For each pair producing gluino (squark) scenario, the models assume all SUSY particles other than the gluino (squark) and lightest neutralino are too massive to be produced directly and the gluino (squark) decays promptly. In addition, each model assumes that the gluino (squark) decays with a 100% branching fraction into the decay products depicted in figure 6.9, except for models where the decays of the two squarks

**Table 6.1:** Typical values of the systematic uncertainties associated with the simplified SUSY model signal yield for each interpretation in this search. Some systematics are taken as correlated amongst all signal regions; the rest are uncorrelated everywhere. Note that the large range of statistical uncertainty is driven by a small number of signal regions with low acceptance (which are not typically sensitive to those model points).

Source	Typical Values	Correlated?
Luminosity	2.6%	✓
Limited size of MC samples	1–100%	-
Renormalization and factorization scales	5%	-
“ISR” recoil	0–30%	✓
B-tagging efficiency, heavy flavor	0–40%	✓
B-tagging efficiency, light flavor	0–20%	✓
Lepton efficiency	0–20%	✓
Jet energy scale	5%	-
Fast simulation $E_T^{\text{miss}}$ modeling	0–5%	✓
Fast simulation pileup modeling	4.6%	✓

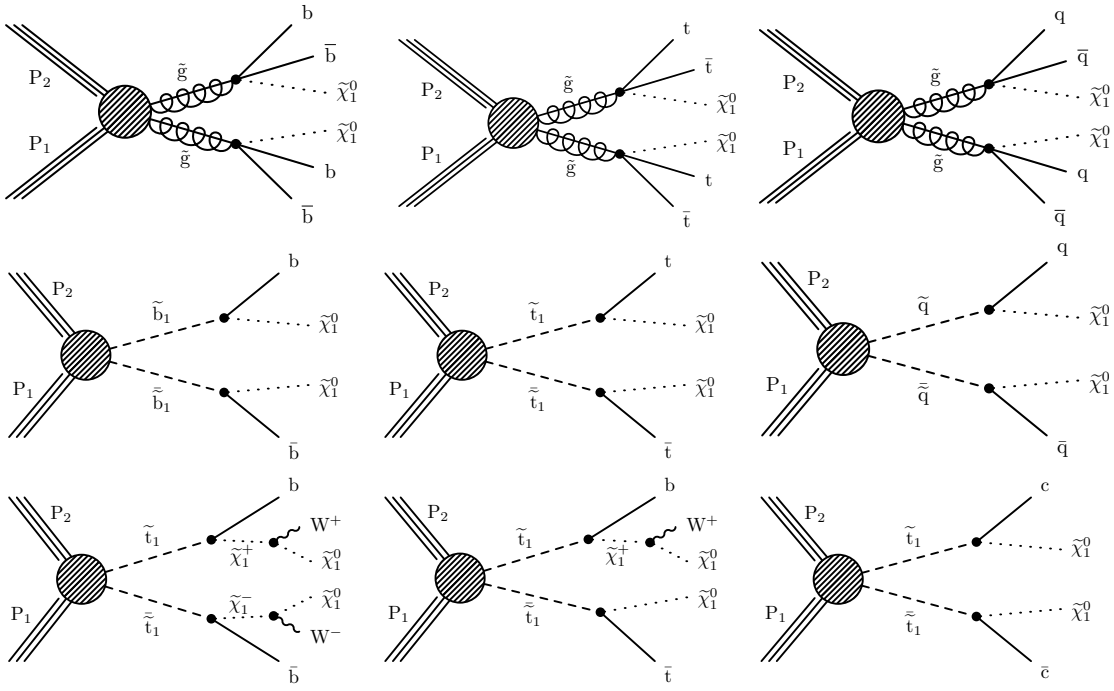


**Figure 6.9:** Feynman diagrams depicting the different simplified SUSY models considered in this analysis. Results are interpreted in the context of gluino-mediated bottom, top, and light-flavor squark production (top), direct production of bottom, top, and light-flavor squarks (middle), and alternate decay modes of direct top squark production (bottom).

differ where a 50% branching fraction for each decay mode is assumed. When considering top squark pair production, the polarization of the top quark is model dependent (and a function of the top-squark and neutralino mixing matrices), so events are generated without polarization to remain model-independent.

The cross-section exclusion limits are calculated at 95% confidence level (CL) for each simplified model [44, 30, 23]. The limits are obtained using the background-fitting procedure described in section 6.1 obtained with the higgsCombine tool. The 95% CL exclusion limits for gluino-mediated models is shown in figure 6.10, for direct squark pro-

duction in figure 6.11, and for alternate top squark decay modes in figure 6.12. The constraints on the masses of SUSY particles excluded by this search is summarized in table 6.2.

This work would not have been possible without all the members of the CMS collaboration, whose support made it possible to produce the figures and tables in this chapter.

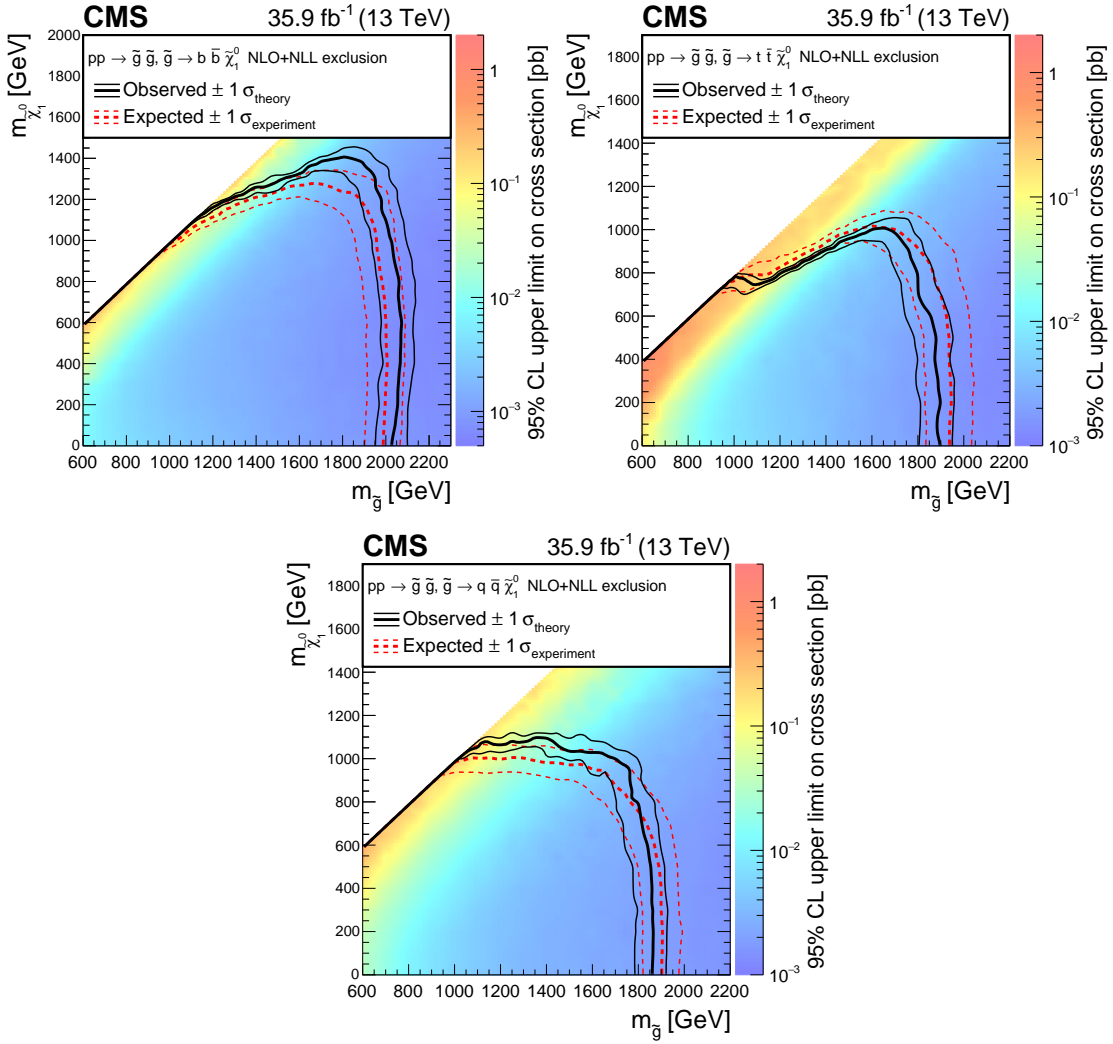


**Figure 6.10:** 95% confidence level exclusion limits for gluino-mediated squark production of bottom (top left), top (top right), and light-flavor (bottom) squarks. Dashed red lines indicate the expected sensitivity and associated uncertainty, while black lines indicate the observed exclusion limit and its associated theoretical uncertainty based on the signal cross-section.

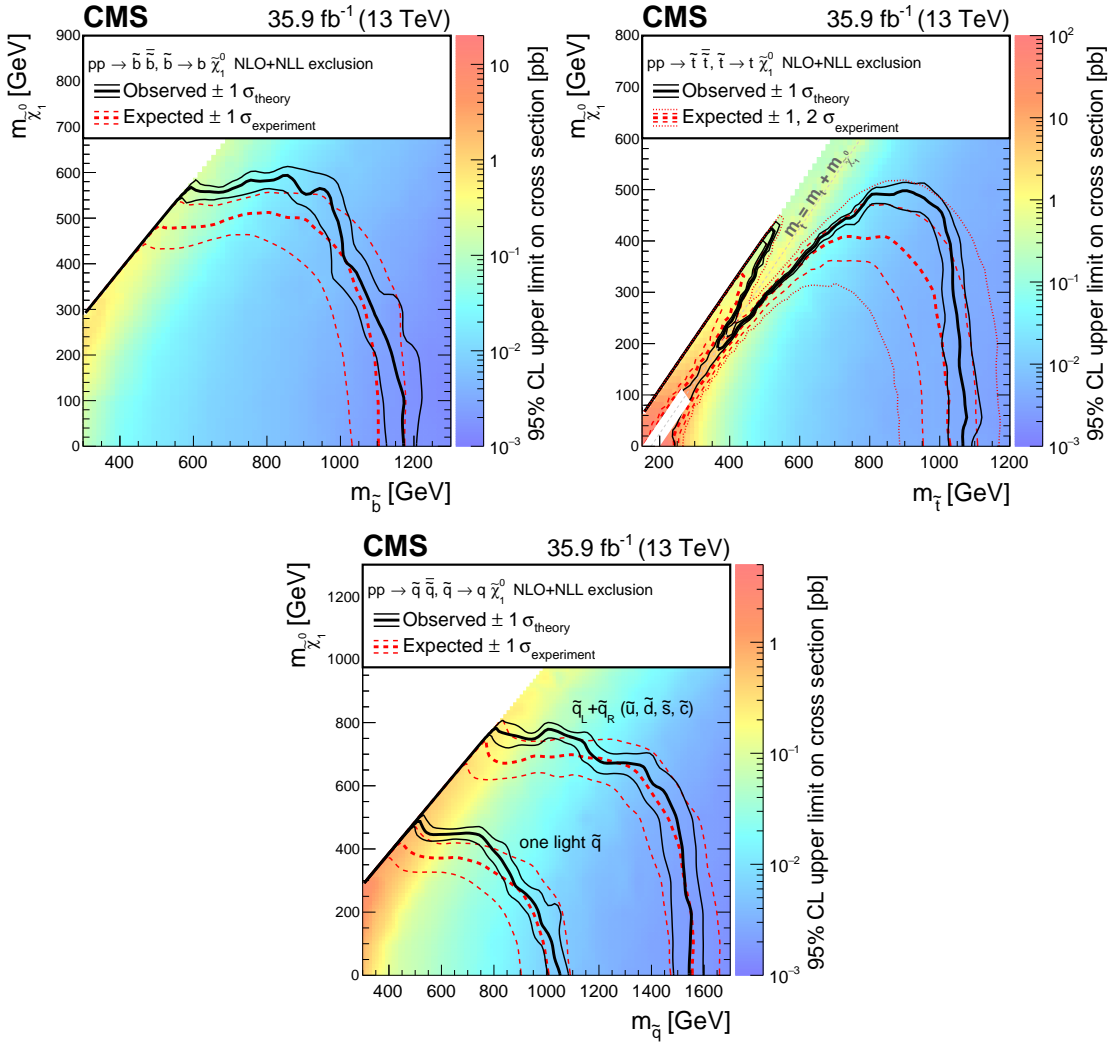


**Figure 6.11:** 95% confidence level exclusion limits for direct squark production of bottom (top left), top (top right), and light-flavor (bottom) squarks. Dashed red lines indicate the expected sensitivity and associated uncertainty, while black lines indicate the observed exclusion limit and its associated theoretical uncertainty based on the signal cross-section.

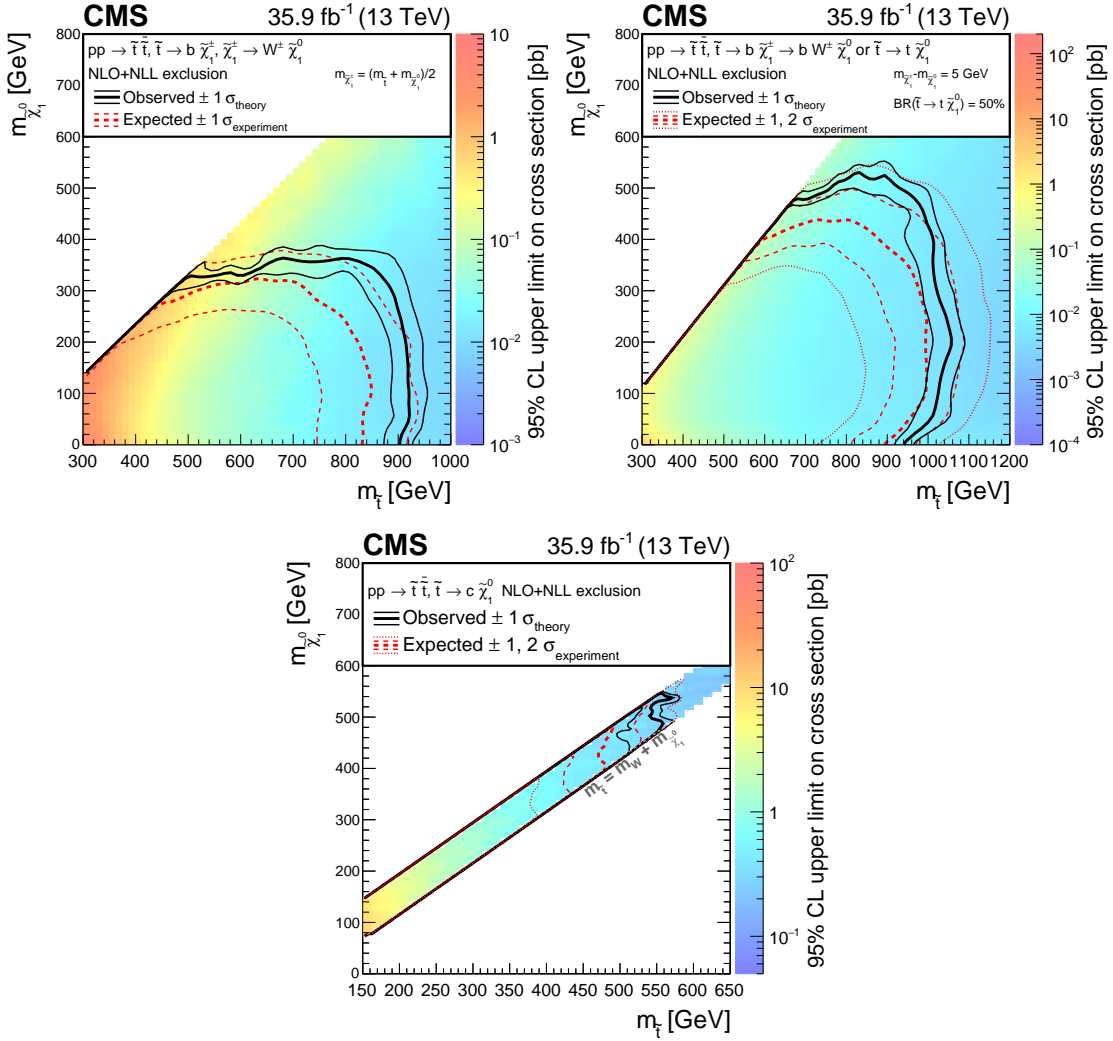


**Figure 6.12:** 95% confidence level exclusion limits for top squark production, decaying either via charginos (top left), where the chargino mass is taken as halfway-between the top squark and neutralino; a mixed mode with charginos and neutralinos (top right), where the  $\tilde{\chi}^{\pm}$  mass is 5 GeV above the  $\tilde{\chi}_1^0$  mass; or a compressed scenario, where the top squark is kinematically constrained to decay to charm quarks (bottom). Dashed red lines indicate the expected sensitivity and associated uncertainty, while black lines indicate the observed exclusion limit and its associated theoretical uncertainty based on the signal cross-section.

**Table 6.2:** Summary of 95% CL exclusion limits on the masses of SUSY particles (sparticles) produced by various simplified models. The limit on the produced sparticle is listed for a massless  $\tilde{\chi}_1^0$ , along with the greatest excluded mass of  $\tilde{\chi}_1^0$  for any mass of produced sparticle.

Simplified model	Limit on produced sparticle mass [GeV] for $m_{\tilde{\chi}_1^0} = 0 \text{ GeV}$	Highest limit on the $\tilde{\chi}_1^0$ mass [GeV]
Direct squark production:		
Bottom squark	1175	590
Top squark	1070	550
Single light squark	1050	475
Eight degenerate light squarks	1550	775
Gluino-mediated production:		
$\tilde{g} \rightarrow b\bar{b}\tilde{\chi}_1^0$	2025	1400
$\tilde{g} \rightarrow t\bar{t}\tilde{\chi}_1^0$	1900	1010
$\tilde{g} \rightarrow q\bar{q}\tilde{\chi}_1^0$	1860	1100

# Chapter 7

## Extending the All-Hadronic Search

The results presented in this analysis thus far exclude significant amounts of SUSY parameter phase space compared to previous searches for similar signatures. However, the spectrum of SUSY models that might be realized in nature is wide and varied. As the LHC continues to deliver an increasing amount of collision data, the ability to probe increasing rare and more subtle signatures increases.

In this final section we discuss extensions to the  $M_{T2}$  analysis that modify the search to target additional SUSY models, in particular those which may produce very low- $p_T$  leptons in the final state, otherwise known as *soft leptons*. By requiring a lepton in the final state, the previously irreducible invisible Z background of the all-hadronic analysis is greatly suppressed, and in principle one might hope to probe additional phase space for new physics.

## 7.1 Natural Supersymmetry and EWKinos

There are a multitude of supersymmetric models which solve some of the theoretical issues of the SM, namely the hierarchy problem discussed in section 2.2. However, given the vast parameter of SUSY phase space which might satisfy physical constraints, it is sometimes considered theoretically unfavorable for a particular model to accomodate physical phenomena at the expense of a theoretical explanation, instead relying on the “fine-tuning” of physical parameters to remain consistent with observations in nature. The property of a theoretical model that consistently explain observed phenomena with minimal tuning is often referred to as its *naturalness*, and can be quantified as a the likelihood for measured observables to be contained in some subset of the total parameter space such that the model satisfies experimental constraints.

A SUSY model that solves some of the fine-tuning problems present in the SM without introducing additional fine-tuning problems of its own is an example of *natural supersymmetry*, and is theoretically appealing as an elegant solution to the would-be fine-tuning issues in the SM [15]. Such natural models often share similar characteristics, including a relative mixing of the supersymmetric partners of the Higgs and electroweak gauge bosons (EWKinos) into mass eigenstates with a highly-degenerate spectrum. Charged EWKinos ( $\tilde{\chi}^\pm$ ) can decay into neutral EWKinos or the lightest supersymmetric particle ( $\tilde{\chi}^0$ ) in cascades with leptons in the final state. In compressed mass spectra where the mass difference between the charged and neutral EWKinos is small, the outgoing leptons will be soft, and searches targeting soft leptons in the final state can be a useful tool in searches for natural

SUSY.

## 7.2 The Soft Lepton Search

A preliminary search extending the all-hadronic analysis was conducted on  $2.3\text{ fb}^{-1}$  of data collected by the CMS detector through 2015 [21]. The results of this preliminary analysis are presented here and interpreted in the context of two simplified SUSY models with compressed spectra.

### 7.2.1 Event Selection

The soft lepton search defines a baseline selection similar to that used in the  $M_{\text{T2}}$  analysis, with the notable exception of requiring a soft electron (muon) with  $5 < p_{\text{T}} < 20\text{ GeV}$  in the barrel region,  $|\eta| < 1.4442$  (1.479). Similar  $E_{\text{T}}^{\text{miss}}$  triggers are used, with a minimum  $E_{\text{T}}^{\text{miss}}$  requirement of  $200\text{ GeV}$  to saturate the trigger efficiency. Identical  $\Delta\phi(j_{1234}, E_{\text{T}}^{\text{miss}})$  and  $|\vec{H}_{\text{T}}^{\text{miss}} - \vec{E}_{\text{T}}^{\text{miss}}|/E_{\text{T}}^{\text{miss}}$  requirements are used to protect against  $E_{\text{T}}^{\text{miss}}$  mismeasurements, and to reject dilepton events the same lepton vetoes are applied to additional leptons in the event. There is an additional requirement on transverse mass of the soft leptons such that  $m_T > 20\text{ GeV}$ , in order to reduce the background contribution from  $Z \rightarrow \tau\tau$  events. Events must contain at least 1 jet and a minimum of  $H_{\text{T}} > 200\text{ GeV}$  of hadronic activity.

Following the baseline selection above, events are further categorized into topological regions using the  $H_{\text{T}}$ ,  $E_{\text{T}}^{\text{miss}}$ , and  $N_{\text{jets}}$  content, as well as the number of b-tags  $N_{\text{b-jets}}^{\text{soft}}$

and  $N_{\text{b-jets}}^{\text{hard}}$ , where a b-jet is considered soft if  $20 < p_T < 50 \text{ GeV}$ , and hard if  $p_T > 50 \text{ GeV}$ .

There are three “tail” regions corresponding to different kinematic variables:

- $N_{\text{b-jets}}$  (soft or hard)  $\geq 3$
- $E_T^{\text{miss}} > 500 \text{ GeV}$  and  $N_{\text{b-jets}} \leq 3$
- $H_T > 1000 \text{ GeV}$ ,  $N_{\text{b-jets}} \leq 3$ , and  $E_T^{\text{miss}} < 500 \text{ GeV}$

The remaining phase space is divided into topological regions as follows:

- $E_T^{\text{miss}}$ :  $[200,300]$ ,  $[300,500]$  GeV. These are merged in the monojet regions with b-tags.
- $N_{\text{b-jets}}$ : There are four  $N_{\text{b-jets}}$  regions,  $N_{\text{b-jets}} = 0$ ,  $N_{\text{b-jets}}^{\text{soft}} = [1,2]$  (with  $N_{\text{b-jets}}^{\text{hard}} = 0$ ), and  $N_{\text{b-jets}}^{\text{hard}} = [1,2]$ , respectively referred to as the 0b, soft b, and hard b regions.
- $N_{\text{jets}}$ : In regions with no b-tags, events are binned in regions with 1, 2-3, 4-5, or  $\geq 6$  jets. In regions with one or more b-tags, events are binned in regions with 1, 2-3, or  $\geq 4$  jets.

Finally, each topological region is subdivided into three bins of  $m_T$ :  $[20,90]$ ,  $[90,120]$ , and  $\geq 120 \text{ GeV}$ . In total, there are 21 topological regions each subdivided into 3  $m_T$  bins.

### 7.2.2 Backgrounds

The background for the soft lepton analysis can be categorized into three separate sources:

- *Single Lepton*: real SM processes can generate events with a single lepton in the final state. Typically such events contain a single leptonically decaying W boson (from either W production, top quark production, or other rare processes), and also generate significant missing energy due to the neutrino associated with the W decay.
- *Dilepton*: SM events with two (or more) leptons in the final state can be misclassified when other leptons are misidentified or not reconstructed. Typically such events are due to two leptonically decaying W bosons (from either  $t\bar{t}$  or diboson production), where one of the W-associated leptons is not found. Because there are usually two neutrinos contributing to the  $E_T^{\text{miss}}$  vector,  $m_T$  is less effective in discriminating against this background.
- *Fake Lepton*: events without any lepton in the final state (such as QCD multijet production of  $Z \rightarrow \nu\bar{\nu}$ ) can enter the signal region if a jet is misidentified as a lepton or a non-prompt lepton passes the lepton selection. This background is highly suppressed and typically negligible in all but some high- $m_T$  regions.

### 7.2.3 Single Lepton Estimate

The single lepton background is primarily due to highly-asymmetric W decays where the neutrino carries a large fraction of the W momentum, resulting in a large  $E_T^{\text{miss}}$  and a soft lepton. These events are greatly suppressed by sampling the  $m_T$  distribution as values greater than the W mass, and is estimated in all signal regions using a control region with an inverted asymmetry. A single high- $p_T$  control region is created by selecting events

with a single lepton above the corresponding  $E_T^{\text{miss}}$  threshold in a given signal region ( $p_T \geq 200, 300, \text{ or } 500 \text{ GeV}$ ), with a maximum threshold on the missing energy  $E_T^{\text{miss}} < 60 \text{ GeV}$  so that the W momentum distribution is kinematically similar to that in the signal regions. The number of control region events in a given topological region ( $N^{\text{CR1L}}$ ) is multiplied by the ratio of SR-to-CR events as calculated in simulation ( $R_{\text{MC}}^{\text{SR/CR1L}}$ ) for the region, and extrapolated into bins of  $m_T$  based on simulation ( $k_{\text{MC}}(m_T)$ ) as described in equation 7.1. The extrapolation in bins of  $m_T$  is necessary not only to preserve statistics but because the shape of the  $m_T$  distribution in each control region is very different from the signal region distribution, due to the low- $E_T^{\text{miss}}$  requirement in the control region where resolution effects cause a significant smearing in the  $m_T$  shape.

$$N_{1l}^{\text{SR}} = N^{\text{CR1L}} \cdot R_{\text{MC}}^{\text{SR/CR1L}} \cdot k_{\text{MC}}(m_T) \quad (7.1)$$

The uncertainties associated with the single lepton estimate account for statistical fluctuations in data and simulation, as well as possible sources of systematic error in simulation propagated to the quantities measured in MC. The polarization modeling is studied in an inclusive W sample and found to be well modeled by simulation, and additional studies reweighting simulation based on W polarization result in an uncertainty of 10-20% on the transfer factor  $R_{\text{MC}}^{\text{SR/CR1L}}$ . Additional uncertainties due to the relative fraction of top and W events, renormalization and factorization scales, lepton efficiency, b-tagging efficiency, jet energy corrections, and uncertainty on top momentum are propagated through simulation, with varying effects between 1-10%. In addition, multiple uncertainties associated with  $m_T$  modeling in simulation are studied, with effects due to W-top fraction and

$E_T^{\text{miss}}$  resolution yielding uncertainties ranging between 5-30% in  $m_T$  shape, depending on the relative fraction of top events in a given bin.

#### 7.2.4 Dilepton Estimate

Backgrounds due to dilepton events where one lepton is not found are estimated using a control region instead requiring two leptons, replacing the second-lepton veto with a tight requirement for a second, high- $p_T$  lepton. To suppress the contribution from events with fake leptons, the second lepton is required to have a minimum  $p_T$  of at least 25 GeV, and the expected statistics, kinematics, and composition of the control region is similar to that of the signal region. Because of the low rate of this background in the signal region (and corresponding low statistics in each control region), the estimate is performed in a similar manner to the single lepton estimate, but with an additional extrapolation in the  $E_T^{\text{miss}}$  dimension based on simulation. The number of control region events in a given region of  $H_T$ ,  $N_{\text{jets}}$ , and  $N_{\text{b-jets}}$  ( $N^{\text{CR2L}}$ ) is multiplied by the ratio of SR-to-CR events as calculated in simulation ( $R_{\text{MC}}^{\text{SR/CR2L}}$ ) for that region, and extrapolated into bins of  $E_T^{\text{miss}}$  and  $m_T$  based on simulation ( $k_{\text{MC}}(E_T^{\text{miss}}, m_T)$ ) as described in equation 7.2.

$$N_{2l}^{\text{SR}} = N^{\text{CR2L}} \cdot R_{\text{MC}}^{\text{SR/CR1L}} \cdot k_{\text{MC}}(E_T^{\text{miss}}, m_T) \quad (7.2)$$

In addition to statistical fluctuations, the uncertainties associated with the dilepton estimate account for several effects, including lepton acceptance in simulation. Varying the renormalization and factorization scales, lepton efficiency, and jet energy corrections in simulation is propagated to the ratio  $R_{\text{MC}}^{\text{SR/CR1L}}$ , yielding uncertainties of 1-10%, 5%,

and 5-20% respectively (the b-tagging uncertainty is found to be negligible). Because the  $Z \rightarrow l^+l^-$  yield in the control region is slightly different than that in the corresponding signal regions, an additional uncertainty of 5-10% is assigned to each region based on the relative fraction of  $Z \rightarrow l^+l^-$  events. Possible systematic effects of the  $E_T^{\text{miss}}$  and  $m_T$  modeling in simulation are also studied in dilepton  $t\bar{t}$  control regions, yielding uncertainties of 10% (35%) in the 300-500 GeV ( $\geq 500$  GeV)  $E_T^{\text{miss}}$  regions and 30% (50%) in the medium (high)  $m_T$  bins.

### 7.2.5 Fake Lepton Estimate

The fake lepton background has multiple contributions from different SM processes. Missing energy mismeasurement may yield a contribution from QCD multijet events, but this background is strongly suppressed due to sufficiently large  $E_T^{\text{miss}}$  requirements in every signal region. Additional contributions from electroweak SM processes with zero or one lepton in the final state but significant  $E_T^{\text{miss}}$  can also contribute, when a fake lepton is found in a zero lepton event (such as  $Z \rightarrow \nu\bar{\nu}$ ) or a real lepton lost and a fake lepton found in a one lepton event (such as W production). In most regions, the fake lepton background is negligible (with respect to uncertainties on the other backgrounds), and so the prediction is taken directly from simulation in the low and medium  $m_T$  regions with a 100% uncertainty on the yield. However, because the fake lepton background is not constrained by  $m_T < m_W$  and falls more slowly than other background distributions in  $m_T$ , in the high- $m_T$  regions it is more significant and estimated from data. To calculate the predicted yield, a loose-not-tight (L!T) control region is constructed with identical

kinematic requirements to the signal region, except the soft lepton is required to pass the loose lepton identification requirements but fail the tight requirements ( $N_{\text{data}}^{\text{L!T}}$ ). Once the contribution from prompt leptons passing the L!T selection ( $N_{\text{prompt}}^{\text{L!T}}$ ), the yield is weighted by the probability that a fake lepton passing the loose selection also passes the tight selection ( $\epsilon_{\text{TL}}$ ). The probability is measured as a function of lepton  $p_{\text{T}}$  in a sample of QCD multijet data enriched in fake leptons, selected using a high-statistics sample of QCD events recorded with pure  $H_{\text{T}}$  triggers. The fake lepton estimate in each high- $m_T$  signal region is described by equation 7.3.

$$N_{\text{SR}}^{\text{fakes}} = \sum_{p_{\text{T}}} \left( N_{\text{data}}^{\text{L!T}}(p_{\text{T}}) - N_{\text{prompt}}^{\text{L!T}}(p_{\text{T}}) \right) \times \frac{\epsilon_{\text{TL}}(p_{\text{T}})}{1 - \epsilon_{\text{TL}}(p_{\text{T}})} \quad (7.3)$$

Based on studies in simulation, the fake-enriched QCD multijet sample has negligible prompt lepton contamination when requiring  $E_{\text{T}}^{\text{miss}} < 50 \text{ GeV}$  and  $m_T < 40 \text{ GeV}$ . The tight-to-loose ratio is  $\mathcal{O}(10\%)$ , and the expected fake yield in the high- $m_T$  bin is  $\mathcal{O}(1)$  events. Thus the estimate is dominated by statistics in the L!T region, ranging between 50-100%.

### 7.2.6 Results and Interpretations

The predicted background yields are compared with  $2.3 \text{ fb}^{-1}$  of data collected by the CMS detector through 2015. No significant deviations from the expected SM background are observed. As with the all-hadronic analysis, the backgrounds are also estimated using a maximum likelihood fitting procedure with a background-only hypothesis as described in section 6.1. Both the pre-fit and post-fit background predictions compared to data are

**Table 7.1:** Typical values of the systematic uncertainties associated with the simplified SUSY model signal yield for each interpretation in this search.

Source	Typical values [%]
Integrated luminosity	2.7
Lepton efficiency	10
Jet energy scale	5
b tagging efficiency	0–20
ISR	15–30
Renormalization and factorization scales	5
Limited size of MC samples	1–70

illustrated in figure 7.1.

Additional fits using a background+signal hypothesis are used to set upper limits on the production cross sections of some simplified SUSY models producing soft leptons. A summary of the uncertainties on the simulated signal yield can be found in table 7.1. The post-fit background yield based on these inputs is used to set 95% confidence level exclusion limits as shown in figure 7.2.

### 7.3 Future Extensions for an All-Hadronic Search

The extension of the all-hadronic analysis presented in this section illustrates one possible way to broaden the scope of an all-hadronic search to target additional sectors

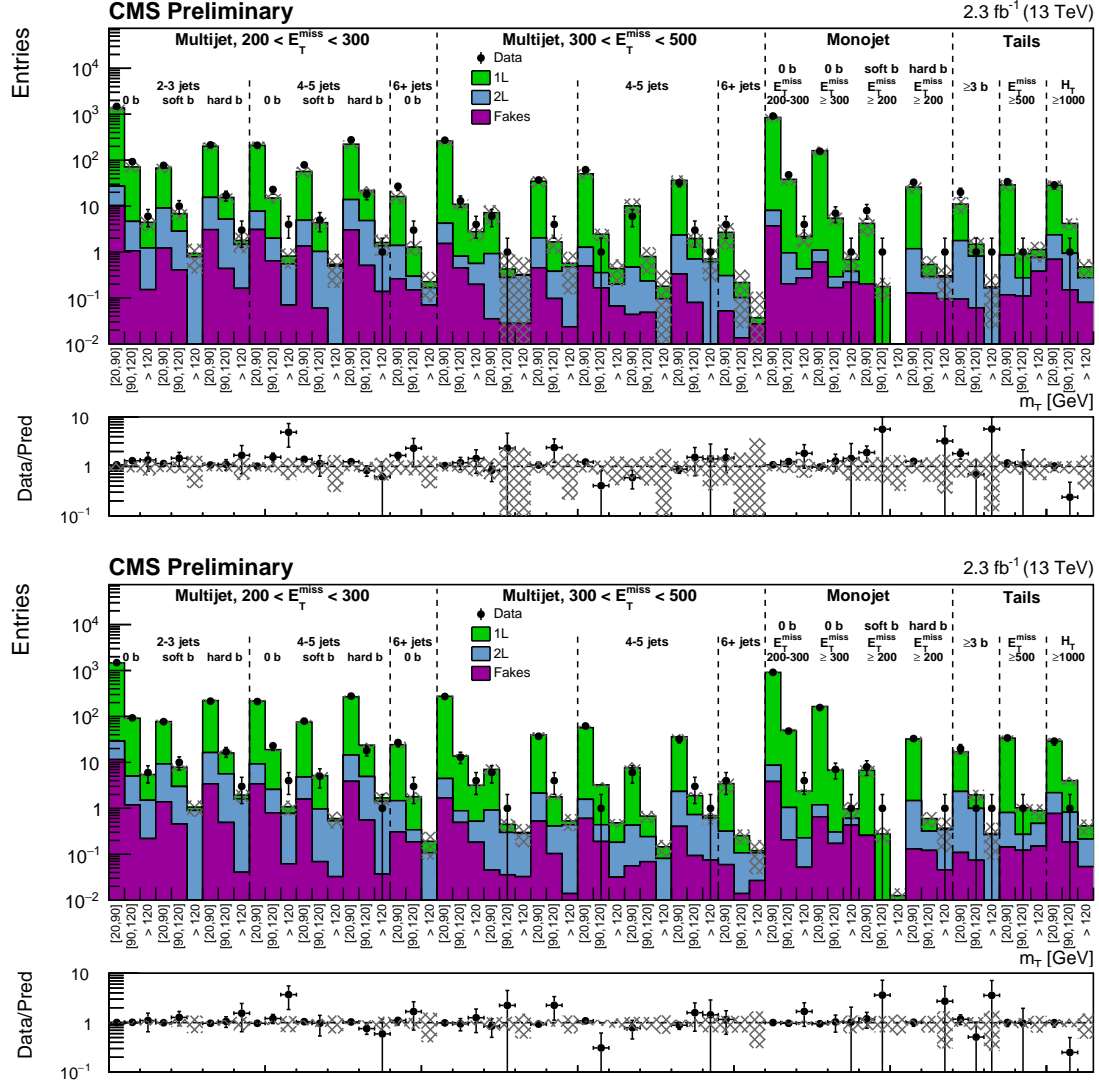


**Figure 7.1:** The predicted background yields compared to the observed number of events in data for pre-fit (top) and post-fit (bottom) background estimates. The  $m_T$  bins are shown on the  $x$ -axis, and the grey hatched band represents the total uncertainty on the background yields for the pre-fit background estimates and the fit uncertainty for the post-fit estimates.

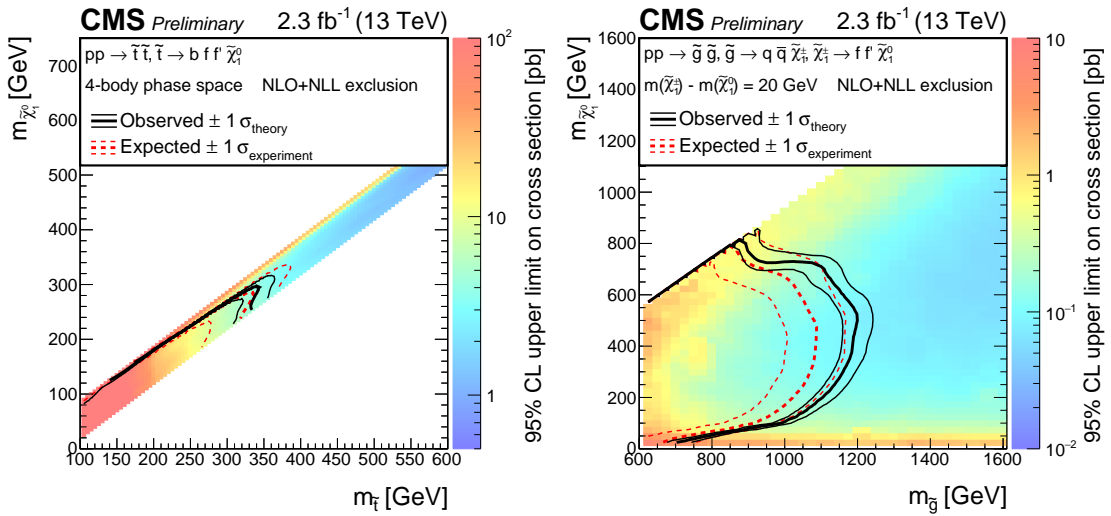


**Figure 7.2:** 95% confidence level exclusion limits for top squark (left) and gluino (right) production. Dashed red lines indicate the expected sensitivity and associated uncertainty, while black lines indicate the observed exclusion limit and its associated theoretical uncertainty based on the signal cross-section.

where new physics might reveal itself. However, there are similar analyses which may supersede the results of a naive single soft lepton search, and an additional question remains – how much does the extension requiring a soft lepton outperform a traditional all-hadronic analysis? An all-hadronic search should have some discriminating power even against models which always generate soft leptons in the final state (since these leptons will occasionally be lost or mis-identified), and ironically may even have greatly discriminatory power than a soft lepton search when the leptons generated are ultra-soft ( $p_T << 5 \text{ GeV}$ ) and not reconstructed at all.

To benchmark the possible performance of an improved soft lepton analysis against an all-hadronic search, the performance of the  $M_{T2}$  analysis on a squark production model generating soft leptons (T5qqWW) is compared to a soft lepton extension. With additional optimization of signal region binning – in particular a finer binning in the low- $E_T^{\text{miss}}$  regime to target compressed spectra – and assuming a typical background estimate uncertainty commensurate with previous analyses, it is possible for a soft lepton analysis to outperform an all-hadronic search as illustrated in figure 7.3.

Near the mass-diagonal where the parent particle mass (in this case, the squark) is very close to the LSP mass, the soft-lepton search can significantly outperform an all-hadronic equivalent, at the cost of performance in the light-LSP regime. The evidence suggests that a soft-lepton search could be used in conjunction with typical all-hadronic analyses to increase the total excluded phase space when targeting compressed models with nearly-degenerate mass splittings.

This work would not have been possible without all the members of the CMS

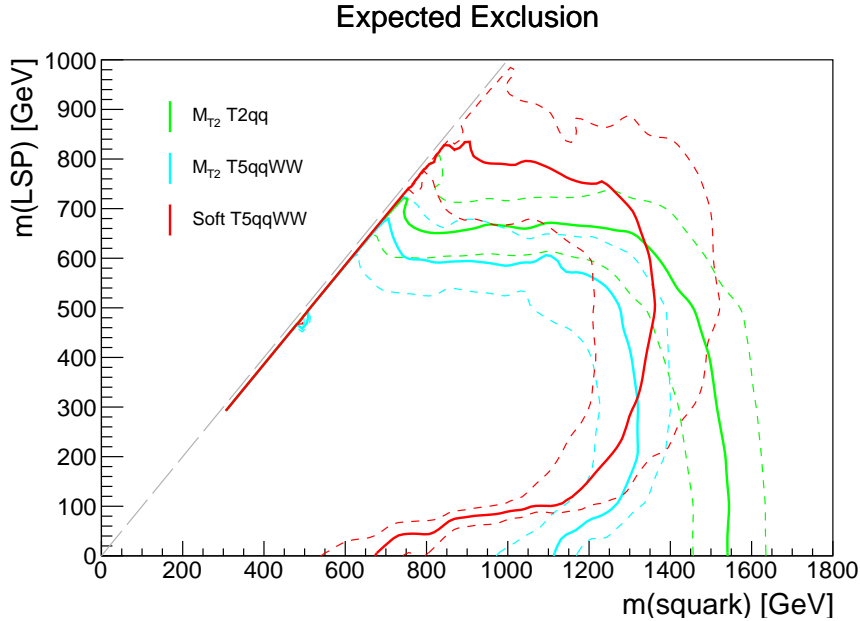


**Figure 7.3:** The expected limits of the all-hadronic  $M_{T2}$  analysis compared with a hypothetical soft lepton extension. The “T2qq” model is a typical squark production model as previously shown in figure 6.11, whereas the “T5qqWW” model is a similar squark production model where the squarks decay in a cascade including charginos, which radiate W bosons that may decay to soft leptons. While the performance of the  $M_{T2}$  analysis in the hadronic model (green) is similar to the soft lepton model (blue), a soft lepton search can out-perform the all-hadronic equivalent near the diagonal where the mass splitting between the squarks and lightest supersymmetric particle is very small.

collaboration, whose support made it possible to produce the figures and tables in this chapter.

# Bibliography

- [1] Morad Aaboud et al. Search for bottom squark pair production in proton-proton collisions at  $\sqrt{s} = 13\text{TeV}$  with the ATLAS detector. *Eur. Phys. J.*, C76(10):547, 2016.
- [2] Morad Aaboud et al. Search for new phenomena in final states with an energetic jet and large missing transverse momentum in  $pp$  collisions at  $\sqrt{s} = 13\text{TeV}$  using the ATLAS detector. *Phys. Rev.*, D94(3):032005, 2016.
- [3] Morad Aaboud et al. Search for squarks and gluinos in final states with jets and missing transverse momentum at  $\sqrt{s} = 13\text{TeV}$  with the ATLAS detector. *Eur. Phys. J.*, C76(7):392, 2016.
- [4] Georges Aad et al. Observation of a new particle in the search for the Standard Model Higgs boson with the ATLAS detector at the LHC. *Phys. Lett.*, B716:1–29, 2012.
- [5] Georges Aad et al. Search for new phenomena in final states with large jet multiplicities and missing transverse momentum with ATLAS using  $\sqrt{s} = 13\text{TeV}$  proton-proton collisions. *Phys. Lett.*, B757:334–355, 2016.
- [6] Georges Aad et al. Search for pair production of gluinos decaying via stop and sbottom in events with  $b$ -jets and large missing transverse momentum in  $pp$  collisions at  $\sqrt{s} = 13\text{TeV}$  with the ATLAS detector. *Phys. Rev.*, D94(3):032003, 2016.
- [7] S Abdullin, P Azzi, F Beaudette, P Janot, A Perrotta, and the CMS Collaboration. The fast simulation of the CMS detector at LHC. *Journal of Physics: Conference Series*, 331(3):032049, 2011.
- [8] S. Agostinelli et al. GEANT4: A Simulation toolkit. *Nucl. Instrum. Meth.*, A506:250–303, 2003.
- [9] W. M. Alberico and S. M. Bilenky. Neutrino oscillations, masses and mixing. *Phys. Part. Nucl.*, 35:297–323, 2004. [Fiz. Elem. Chast. Atom. Yadra35,545(2004)].
- [10] Johan Alwall, Michel Herquet, Fabio Maltoni, Olivier Mattelaer, and Tim Stelzer. MadGraph 5 : Going Beyond. *JHEP*, 06:128, 2011.

- [11] S. Baffioni, C. Charlot, F. Ferri, D. Futyan, P. Meridiani, I. Puljak, C. Rovelli, R. Salerno, and Y. Sirois. Electron reconstruction in CMS. *Eur. Phys. J.*, C49:1099–1116, 2007.
- [12] G. L. Bayatian et al. CMS Physics. 2006.
- [13] Matteo Cacciari and Gavin P. Salam. Pileup subtraction using jet areas. *Phys. Lett.*, B659:119–126, 2008.
- [14] Matteo Cacciari, Gavin P. Salam, and Gregory Soyez. The Anti-k(t) jet clustering algorithm. *JHEP*, 04:063, 2008.
- [15] J. Alberto Casas, Jesús M. Moreno, Sandra Robles, Krzysztof Rolbiecki, and Bryan Zaldívar. What is a Natural SUSY scenario? *JHEP*, 06:070, 2015.
- [16] S. Chatrchyan et al. The CMS Experiment at the CERN LHC. *JINST*, 3:S08004, 2008.
- [17] S Chatrchyan et al. Performance of CMS Muon Reconstruction in Cosmic-Ray Events. *JINST*, 5:T03022, 2010.
- [18] Serguei Chatrchyan et al. Missing transverse energy performance of the CMS detector. *JINST*, 6:P09001, 2011.
- [19] Serguei Chatrchyan et al. Observation of a new boson at a mass of 125 GeV with the CMS experiment at the LHC. *Phys. Lett.*, B716:30–61, 2012.
- [20] The CMS Collaboration. Jet energy scale and resolution performances with 13 TeV data. Jun 2016.
- [21] The CMS Collaboration. Search for new physics in the one soft lepton final state using 2015 data at  $\sqrt{s} = 13$  TeV. Technical Report CMS-PAS-SUS-16-011, CERN, Geneva, 2016.
- [22] Edvige Corbelli and Paolo Salucci. The Extended Rotation Curve and the Dark Matter Halo of M33. *Mon. Not. Roy. Astron. Soc.*, 311:441–447, 2000.
- [23] Glen Cowan, Kyle Cranmer, Eilam Gross, and Ofer Vitells. Asymptotic formulae for likelihood-based tests of new physics. *Eur. Phys. J.*, C71:1554, 2011. [Erratum: Eur. Phys. J.C73,2501(2013)].
- [24] Creative commons attribution 3.0 unported.
- [25] Lyndon Evans and Philip Bryant. LHC Machine. *JINST*, 3:S08001, 2008.
- [26] Pierre Fayet. Supergauge invariant extension of the higgs mechanism and a model for the electron and its neutrino. *Nuclear Physics B*, 90:104 – 124, 1975.

- [27] S. L. Glashow. Partial Symmetries of Weak Interactions. *Nucl. Phys.*, 22:579–588, 1961.
- [28] Yu. A. Golfand and E. P. Likhtman. Extension of the Algebra of Poincare Group Generators and Violation of p Invariance. *JETP Lett.*, 13:323–326, 1971. [Pisma Zh. Eksp. Teor. Fiz. 13, 452 (1971)].
- [29] Rudolf Haag, Jan T. Lopuszanski, and Martin Sohnius. All Possible Generators of Supersymmetries of the s Matrix. *Nucl. Phys.*, B88:257, 1975. [, 257(1974)].
- [30] Thomas Junk. Confidence level computation for combining searches with small statistics. *Nucl. Instrum. Meth.*, A434:435–443, 1999.
- [31] Vardan Khachatryan et al. Performance of Photon Reconstruction and Identification with the CMS Detector in Proton-Proton Collisions at  $\sqrt{s} = 8\text{TeV}$ . *JINST*, 10(08):P08010, 2015.
- [32] Vardan Khachatryan et al. Search for new physics with the  $M_{T2}$  variable in all-jets final states produced in pp collisions at  $\sqrt{s} = 13\text{TeV}$ . *JHEP*, 10:006, 2016.
- [33] Vardan Khachatryan et al. Search for new physics with the  $M_{T2}$  variable in all-jets final states produced in pp collisions at  $\sqrt{s} = 13\text{TeV}$ . *JHEP*, 10:006, 2016.
- [34] Vardan Khachatryan et al. Search for supersymmetry in the multijet and missing transverse momentum final state in pp collisions at  $13\text{TeV}$ . *Phys. Lett.*, B758:152–180, 2016.
- [35] Vardan Khachatryan et al. A search for new phenomena in pp collisions at  $\sqrt{s} = 13\text{TeV}$  in final states with missing transverse momentum and at least one jet using the  $\alpha_T$  variable. *Eur. Phys. J.*, C77(5):294, 2017.
- [36] Vardan Khachatryan et al. Inclusive search for supersymmetry using razor variables in pp collisions at  $\sqrt{s} = 13\text{TeV}$ . *Phys. Rev.*, D95(1):012003, 2017.
- [37] Vardan Khachatryan et al. Jet energy scale and resolution in the CMS experiment in pp collisions at  $8\text{TeV}$ . *JINST*, 12(02):P02014, 2017.
- [38] C. G. Lester and D. J. Summers. Measuring masses of semiinvisibly decaying particles pair produced at hadron colliders. *Phys. Lett.*, B463:99–103, 1999.
- [39] Stephen P. Martin. A Supersymmetry primer. pages 1–98, 1997. Adv. Ser. Direct. High Energy Phys. 18, 1 (1998).
- [40] A. Neveu and J.H. Schwarz. Factorizable dual model of pions. *Nuclear Physics B*, 31(1):86 – 112, 1971.
- [41] H.P. Nilles. Supersymmetry, supergravity and particle physics. *Physics Reports*, 110(1):1 – 162, 1984.

- [42] Carlo Oleari. The POWHEG-BOX. *Nucl. Phys. Proc. Suppl.*, 205-206:36–41, 2010.
- [43] P. Ramond. Dual theory for free fermions. *Phys. Rev. D*, 3:2415–2418, May 1971.
- [44] A L Read. Presentation of search results: the CL s technique. *Journal of Physics G: Nuclear and Particle Physics*, 28(10):2693, 2002.
- [45] Abdus Salam. Weak and Electromagnetic Interactions. *Conf. Proc.*, C680519:367–377, 1968.
- [46] Matthias Schröder. Performance of jets at CMS. *J. Phys. Conf. Ser.*, 587(1):012004, 2015.
- [47] A. M. Sirunyan et al. Particle-flow reconstruction and global event description with the CMS detector. *JINST*, 12(10):P10003, 2017.
- [48] Albert M Sirunyan et al. Search for new phenomena with the  $M_{T2}$  variable in the all-hadronic final state produced in proton-proton collisions at  $\sqrt{s} = 13$  TeV. *Eur. Phys. J.*, C77(10):710, 2017.
- [49] Torbjorn Sjostrand, Stephen Mrenna, and Peter Z. Skands. A Brief Introduction to PYTHIA 8.1. *Comput. Phys. Commun.*, 178:852–867, 2008.
- [50] D. V. Volkov and V. P. Akulov. Possible universal neutrino interaction. *JETP Lett.*, 16:438–440, 1972. [Pisma Zh. Eksp. Teor. Fiz. 16, 621 (1972)].
- [51] Steven Weinberg. A Model of Leptons. *Phys. Rev. Lett.*, 19:1264–1266, 1967.
- [52] J. Wess and B. Zumino. A lagrangian model invariant under supergauge transformations. *Physics Letters B*, 49(1):52 – 54, 1974.
- [53] J. Wess and B. Zumino. Supergauge transformations in four dimensions. *Nuclear Physics B*, 70(1):39 – 50, 1974.